Master's Thesis in Materials, Energy and Nanotechnology

Thomas Qureishy

Synthesis and structural studies of $Mg_2Si_{1-x}Sn_x$

60 credits

DEPARTMENT OF PHYSICS
Faculty of Mathematics and Natural Sciences
UNIVERSITY OF OSLO

September 15th, 2012

Preface

This Master's thesis is a part of my Master's degree in the program "Materials, Energy and Nanotechnology" at the University of Oslo. The experiments were carried out in the Structure Physics Group at the Centre of Materials Science and Nanotechnology (SMN) from January 2011 to September 2012, in collaboration with the Basic and Applied ThermoElectrics (BATE) group. BATE is a group for people working with thermoelectric materials and devices. Some of the results were presented as a poster presentation, which was held at the Nordic Microscopy Society (SCANDEM) conference in Bergen in June, 2012.

Firstly, I would like to thank my three supervisors, Johan Taftø, Ole Bjørn Karlsen and Anette E. Gunnæs, for giving me the opportunity to work on a very interesting project, for teaching, helping and motivating me, and for many interesting discussions. I could not have completed this project without them. I would also like to take the opportunity to thank Vidar Hansen. Although he wasn't officially a supervisor, the two of us spent a lot of time doing transmission electron microscopy (TEM) together.

Others that I am grateful to are Øystein Prytz for teaching me how to use the JEOL 2000FX TEM, Camilla K. Vigen for teaching me how to use the Quanta 200 FEI scanning electron microscope, Kjetil Valset for teaching me how to make TEM powder specimens and how to use the precision ion polishing system, both Fredrik S. Hage and Kjetil Valset for helping me with TEM related issues, and the rest of my colleagues and friends in the Structure Physics Group for providing me with a friendly environment.

Special thanks to my father, Kim Qureishy, for teaching me mathematics and science for the past 24 years, and for supporting and motivating me with my studies.

Thomas Qureishy

(University of Oslo, September 2012)

Abstract

Samples of $Mg_2Si_{1-x}Sn_x$, a promising thermoelectric material, were synthesized with nominal compositions of x = 0.00, 0.25, 0.50, 0.75 and 1.00, with Mg in excess, and characterized by powder X-ray diffraction (XRD), optical microscopy, scanning electron microscopy (SEM) and transmission electron microscopy (TEM). The synthesis methods include solid state synthesis, solidification of melts and a boron oxide flux method.

The chemistry of the products was characterized by energy dispersive spectroscopy in an SEM and a TEM. The microstructures of the samples that were cooled from a melt were studied with optical microscopy and SEM. Dendritic $Mg_2Si_{1-x}Sn_x$ crystals rich in Si were surrounded by $Mg_2Si_{1-x}Sn_x$ crystals rich in Sn, which were in turn surrounded by eutectic mixtures of Sn and Mg_2Si.

Powder XRD performed on all of the synthesized materials show that the average crystal structure of the material is antifluorite type, as reported in the literature.

The nanostructure of $Mg_2Si_{1-x}Sn_x$ has been investigated with selected area diffraction (SAD) techniques in a TEM. Tilt series of SAD patterns have been carried out on several particles, and some of them had diffraction patterns with extra reflections, due to local ordering phenomena. Three superstructures were proposed, where there is an ordering of the Si – Sn sub-lattice of the same kind as in ordered Cu_3Au and CuAu I-type structures, but the diffraction patterns from the tilt series of $Mg_2Si_{1-x}Sn_x$ were not consistent with the superstructures. The hypothesis was that $Mg_2Si_{1-x}Sn_x$ crystals had Cu_3Au type of ordering of the Si – Sn sub-lattice in $Mg_2Si_{0.25}Sn_{0.75}$ and $Mg_2Si_{0.75}Sn_{0.25}$, and that $Mg_2Si_{0.50}Sn_{0.50}$ crystals had CuAu I-type of ordering of the Si and Sn atoms. The particles showing weak superstructure reflections in the diffraction patterns may consist of crystals with CuAu II-type or related structures.

Some SAD patterns had reflections that were surrounded by satellites. These were caused by double diffraction due to the presence of elemental Sn in addition to $Mg_2Si_{1-x}Sn_x$.

Abbreviations

at. %: atomic per cent

BATE: Basic and Applied ThermoElectrics

bcc: body-centred cubic

BFP: backfocal plane

b.p.: boiling point

BSE: backscattered electron

CBED: convergent beam electron diffraction

EDS: energy dispersive spectroscopy

fcc: face-centred cubic

FEG: field emission gun

FFT: fast Fourier transform

FOLZ: first order Laue zone

hcp: hexagonal closest packing

HOLZ: higher order Laue zone

HRTEM: high resolution transmission electron microscopy

JEOL: Japanese Electron Optics Laboratory

m.p.: melting point

OM: optical microscopy

PIPS: Precision Ion Polishing System

SAD: Selected area diffraction

SAED: Selected area electron diffraction

SE: secondary electron

SOLZ: second order Laue zone

SEM: scanning electron microscope/microscopy

SPS: spark plasma sintering

TEM: transmission electron microscope/microscopy

XRD: X-ray diffraction

wt. %: weight per cent

ZOLZ: zero order Laue zone

Table of Contents

1. Introduction

As the world's population increases and the economy of many countries grows, it becomes more and more difficult to meet the increasing energy demand. Today's society relies heavily on fossil fuels as energy sources, which pollutes the environment and will eventually run out. There is more than enough renewable energy to satisfy the energy demand of the whole world, but the challenges lie in harvesting, storing and distributing the energy. There is a lot of waste heat from energy consumption that dissipates into the atmosphere. With the help from improved thermoelectric materials, a great amount of this heat could be converted into electricity.

This chapter starts with a brief description of thermoelectric effects and a description of thermoelectric materials, followed by the motivation behind and purpose of the experiments in this project. Then there is a section on reported phases and synthesis methods carried out by other research groups, and tables containing information on how well the materials perform as thermoelectric materials. The last sub-chapter is an introduction to the material systems.

1.1 Thermoelectricity

Thermoelectric materials are applied in thermoelectric generators for conversion of heat into electricity, and in heat pumps for conversion of electricity into temperature gradients [1]. The dimension-less figure of merit, *ZT*, of a material is one way of describing its thermoelectric efficiency:

$$ZT = \frac{\alpha^2 \sigma}{\kappa} T \qquad (1.1)$$

where T is the absolute temperature, α is the Seebeck coefficient (in units of volts/Kelvin), σ is the electrical conductivity and κ the thermal conductivity. A good thermoelectric material should have a high Seebeck coefficient and electrical conductivity, but the thermal conductivity should be low. It is difficult to satisfy these criteria, because all of these three parameters are interdependent. The thermal conductivity is a sum of contributions from the lattice and the electrons. By lowering the lattice thermal conductivity in a material, a higher

ZT can be obtained, without drastically altering the other parameters. A good thermoelectric material should not only have a high *ZT*, but also be produced from environmentally friendly, cheap and abundant materials.

Most thermoelectric materials are semiconductors or semimetals. Examples of promising materials include bismuth antimony telluride solid solutions, lead tellurides, Mg_2B^{IV} compounds (B^{IV} = Si, Sn, Ge), silicon-germanium alloys, skutterudites, clathrates, zinc antimonide, transition metal silicides, sodium cobalt oxides and Zintl phase materials [1, 2].

1.2 Purpose of and motivation for the thesis

Both magnesium silicide (Mg_2Si) and magnesium stannide (Mg_2Sn) are promising thermoelectric materials, but suffer from relatively high thermal conductivities. The lattice thermal conductivities are much lower in Mg_2Si – Mg_2Sn solid solutions, because the phonons are scattered by impurities due to the large difference between the mass of Si atoms and Sn atoms. With *x* varying between 0.4 and 0.6, $Mg_2Si_{1-x}Sn_x$ is an excellent thermoelectric material in the temperature range of 600 – 870 K. It has a high *ZT* and is made from eco-friendly, cheap and abundant materials [3].

Although the system $Mg_2Si_{1-x}Sn_x$ has been studied thoroughly, not much is known about the local structure of the material. To our knowledge, only Zhang et al. [4] have carried out structural studies with transmission electron microscopy (TEM). The purpose of this project is to synthesize and characterize $Mg_2Si_{1-x}Sn_x$ samples. They will be synthesized by different methods and characterized with optical microscopy, scanning electron microscopy (SEM), X-ray diffraction (XRD) and TEM.

$Mg_2Si_{1-x}Sn_x$ is reported to have an antifluorite structure. A hypothesis is that there is ordering of the Si-Sn sub-lattice at certain compositions. This hypothesis will be tested by using selected area diffraction techniques with TEM.

1.3 Synthesis and phase separation of $Mg_2Si_{1-x}Sn_x$ reported in the literature

In 1966 Muntyanu et al. constructed a binary phase diagram of the system magnesium silicide – magnesium stannide ($Mg_2Si - Mg_2Sn$) [5]. Samples of $Mg_2Si_{1-x}Sn_x$ were synthesized by mixing magnesium (Mg), silicon (Si) and tin (Sn) (x = 0.0, 0.1, 0.2, ..., 1.0), heating the mixture in an alumina crucible to the melting point of Mg_2Si (1102 °C) and held at that temperature for 3-4 hours, and then cooling the liquid by 10-15 °C/min. The heating was performed in air. During the cooling process, peritectic reactions occurred at 860 °C. Based on studies with XRD, specific gravity and microhardness of the alloys, it was concluded that the system showed solid solubility for $x < 0.08$ and for $x > 0.62$ at room temperature (corresponding to $Mg_2Si_{0.92}Sn_{0.08}$ and $Mg_2Si_{0.38}Sn_{0.62}$, respectively). The solid solubility is temperature dependent. For instance, at 600 °C, the system shows solid solubility at $x < 0.13$ and $x > 0.6$. Hence, there is a temperature-dependent solid miscibility gap located in the system.

Another $Mg_2Si - Mg_2Sn$ phase diagram was constructed by Nikitin et al. in 1968 [6]. Stoichiometric amounts of Mg, Si and Sn were mixed (using the same atomic ratios as in [5]). The mixtures were melted in closed alumina crucibles in an argon (Ar) atmosphere and kept in the molten state for 2 hours. In order to avoid separation of phases due to density differences, the melts were kept in vibration. The samples were cooled by 1.5 °C/min and subsequently annealed at a temperature of 100 °C below the solidus temperature (~760 °C) for 500 h. XRD, differential thermal analyses (DTA), microhardness- and density measurements were performed. A peritectic reaction occurred at 860 °C, as similarly discovered by Muntyanu et al. [5], but the two-phase region of solid solubility was found to be much narrower. According to Nikitin et al. [6], the solid miscibility gap for $Mg_2Si_{1-x}Sn_x$ ranges from x = 0.4 to x = 0.6 at temperatures below 860 °C. They explain that their different results are due to longer annealing times and slower crystallization. The two phase diagrams are presented and compared in Fig. 1.1 [6].

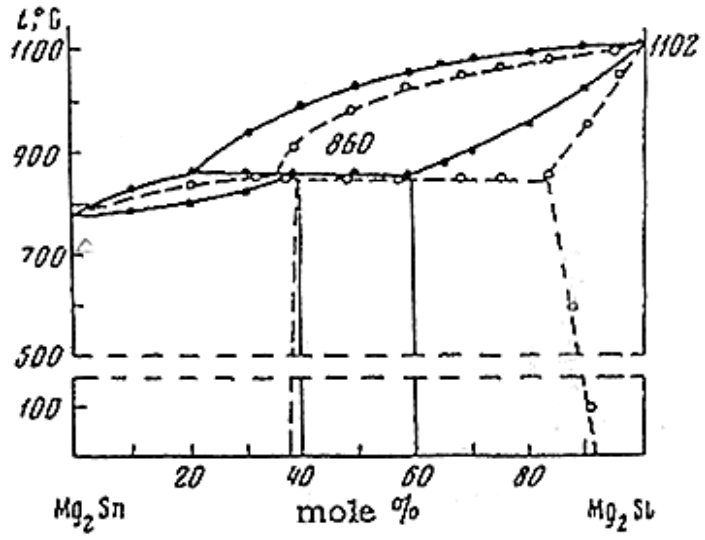

Figure 1.1: A comparison of a binary phase diagram of Mg_2Si – Mg_2Sn by Muntyanu et al. [5] showing a wide immiscibility gap, and that of Nikitin et al. [6] with a narrow gap.

In 2007, Jung et al. used thermodynamic modelling to construct a ternary Mg-Si-Sn phase diagram [7]. Figure 1.2 shows a phase diagram based on their data, as presented in ASM Alloy Phase Diagrams Center [8]. The phase diagram with the larger solid immiscibility range of the two described above was favoured for the calculations. They claim that phase separation is kinetically slow, so it is more probable that the phase diagram with the wider miscibility gap is closer to thermodynamic equilibrium.

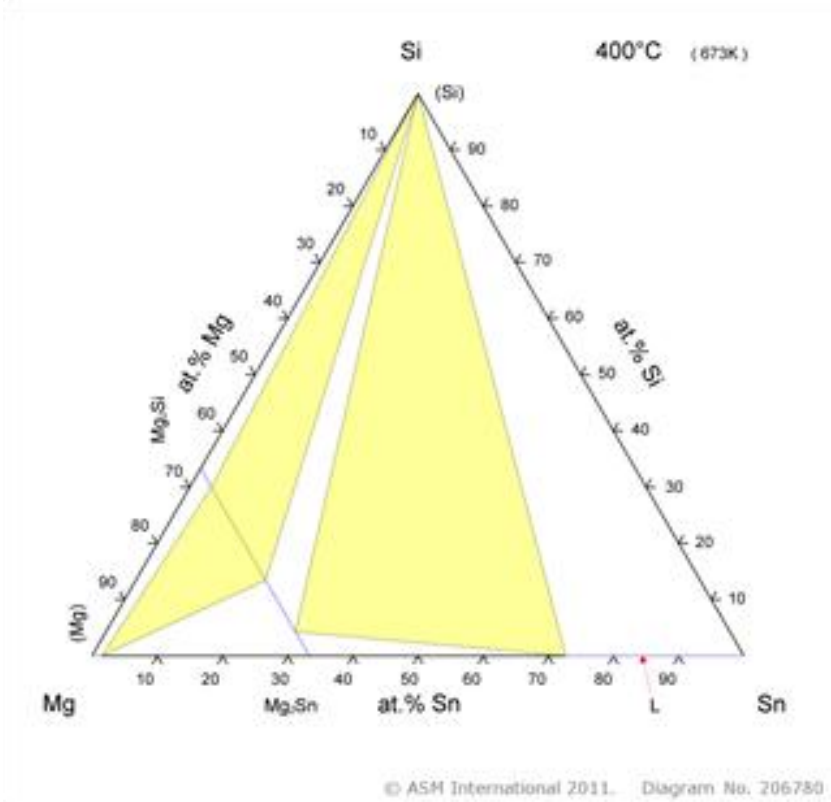

Figure 1.2: A Mg-Si-Sn ternary phase diagram [8].

Zaitsev et al. synthesized and studied Mg_2Si – Mg_2Sn solid solutions in 2006 [3]. $Mg_2Si_{1-x}Sn_x$ was made by melting the components in a boron nitride (BN) crucible by high-frequency (HF) heating, followed by annealing. Solid solubility was observed for $x < 0.4$ and $x > 0.6$. Both $Mg_2Si_{0.4}Sn_{0.6}$ and $Mg_2Si_{0.6}Sn_{0.4}$ had good thermoelectric properties, the former having a higher figure of merit (*ZT*) but the latter being more oxidation resistant and more stable towards vaporization at high temperatures.

In 2007 Zhang et al. [9] synthesized $Mg_2Si_{1-x}Sn_x$ (x = 0.2, 0.4, 0.6 and 0.8) by two different methods. The first technique involves melting and solidification of stoichiometric amounts of the elements by HF heating in an Ar atmosphere. In the other method, they first made Mg_2Si by mixing and melting Mg and Si, and Mg_2Sn by mixing and melting Mg and Sn. Then Mg_2Si and Mg_2Sn were crushed into powders, mixed with each other, and hot pressed at 700 °C under 60 MPa for 2 hours. XRD experiments of the samples produced by both methods showed that those made by the second technique resulted in solids with homogeneous structures.

In 2011 Kozlov et al. [10] synthesized $Mg_2Si_{1-x}Sn_x$ by mixing and pressing stoichiometric amounts of the elements (x = 0.5, 0.58 and 0.75) into pellets and heating them in a tantalum (Ta) tube. The pellets were heated at a rate of 10 °C/min to approximately 1300 °C, then kept at that temperature for 15 minutes, and cooled down at a rate of 10 °C/min. By combining SEM, DTA and differential scanning calorimetry (DSC) experiments with the Calphad method for generating consistent thermodynamic descriptions of binary systems, a phase diagram with a large solid miscibility gap and lower peritectic temperature (781.5 °C) was constructed (see Fig. 1.3). Near the peritectic temperature the two-phase region lies where $0.21 < x < 0.88$. The immiscibility region is very temperature sensitive: it covers the entire composition range below 100 °C. Microstructural studies with SEM showed that Si-rich phases were surrounded by Sn-rich phases in the bulk specimens.

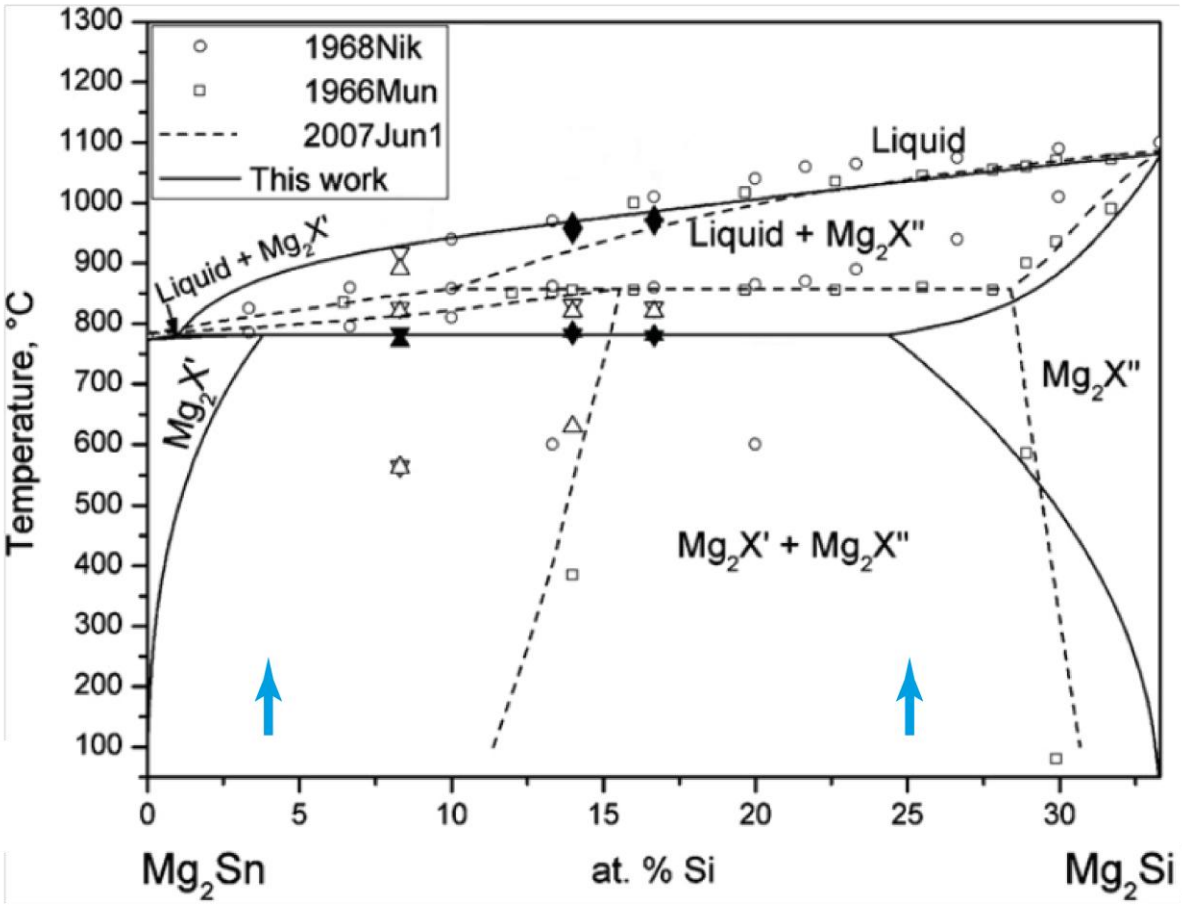

Figure 1.3: A binary Mg_2Si – Mg_2Sn phase diagram constructed by Kozlov et al. (solid lines) [10], also showing data from Muntyanu et al. (circles) [5], Nikitin et al. (triangles) [6] and Jung et al. (dashed lines) [7]. (Adapted from [10].)

Mg-Si-Sn alloys can also be made by microwave irradiation. In 2011 Zhou et al. [11] mixed Mg (200 mesh), Si (300 mesh) and Sn (300 mesh) with an ultrasonic homogenizer in ethanol for 45 minutes, dried the mixtures, pressed them into pellets, and put the pellets in alumina crucibles in a microwave oven with an Ar atmosphere. $Mg_2Si_{1-x}Sn_x$ with x = 0.2, 0.4, 0.6 and 0.8 were heated to 600 – 620 °C and held at those temperatures for 30 – 40 minutes, and then cooled down to room temperature. XRD analyses indicated that the products were homogeneous solid solutions of $Mg_2(Si,Sn)$, giving single peaks in X-ray diffractograms. They claim that oxidation and evaporation of Mg is significantly reduced with this method, compared to that of more conventional techniques, such as melting and solid state reactions.

Riffel and Schilz synthesized $Mg_2Si_{1-x}Sn_x$ solid solutions with x = 0.0, 0.2 and 0.4 by planetary ball milling and hot-pressing in 1996 [12]. The ball milling was performed with 100 steel balls in n-hexane inside a steel vessel under Ar-atmosphere, for 8 – 150 h. The reactants were the pure elements. By using different characterization techniques (SEM, XRD, energy dispersive spectroscopy (EDS) in a TEM, and X-ray fluorescence (XRF)), it was concluded that the system went through a metastable Mg_2Sn phase, which reacted with pure Si and Mg, and the result was a powder with the nominal compositions (with Fe impurities of 3 at.%). The ball milled powders were hot-pressed at 850 °C. XRD measurements showed that a Si-rich peak had split into three peaks after hot-pressing, due to phase separation. The peaks corresponded to phases with the nominal compositions, $Mg_2Si_{0.72}Sn_{0.28}$ and $Mg_2Si_{0.09}Sn_{0.91}$, respectively. This implied a miscibility gap between x = 0.28 and 0.91 at 850 °C.

Bulk mechanical alloying (BMA) was applied by Song et al. in 2007 [13]. BMA consists of cycles of pressing a mixture of powders in a die-punch system in an inert atmosphere [14]. Mg, Si and Sn powders (x = 0, 0.2, 0.4, …, 1.0) were mixed, then solid state synthesis was initiated by BMA in a stainless steel die in an Ar atmosphere, and then the final product was ground and sintered (in order to improve the figure of merit of the material) [13]. The sintering was performed at 500 °C under a pressure of 1 GPa for an hour.

In 2011, Boudemagh et al. [15] studied the structure of $Mg_2Si_{1-x}Sn_x$ at different temperatures. Samples of four different nominal compositions (x = 0.0, 0.4, 0.6 and 1.0) were prepared by heating the elements in a Ta ampoule to 950 – 1150 °C (depending on the composition) [16]

in an HF furnace with an Ar atmosphere, followed by annealing at 800 °C for 20 minutes. They report a phase separation for samples with a nominal composition of $Mg_2Si_{0.6}Sn_{0.4}$. Hence, they concluded that the miscibility gap in the Mg_2Si – Mg_2Sn phase diagram has a boundary at $x < 0.4$. After cooling down their samples, by using XRD from room temperature up to 700 °C and DSC up to 1200 °C, they concluded that there is a phase change from a structure with a cubic lattice to one with a hexagonal closest packing lattice (space group $P6_3/mmc$, number 194) at certain temperatures. This phase transformation temperature varies with the composition of the material, but is reported to be 580, 570 and 590 °C for x = 0.0, 0.4 and 1.0, respectively. Also, the unit cell of the high-temperature hexagonal phase had a very small volume compared to that of the cubic phase.

A single phase of $Mg_2Si_{0.50}Sn_{0.50}$ was synthesized by Isoda et al. in 2004 [17] and later by Isoda et al. in 2006 [18] by a liquid-solid reaction method followed by hot-pressing. This was confirmed by XRD. In 2004, Mg_2Si and Mg_2Sn were made by melting the elements in alumina crucibles. The solid products, namely Mg_2Si and Mg_2Sn, were crushed and mixed, then sintered at 641 – 918 °C under 50 – 70 MPa. A single phase of $Mg_2Si_{0.50}Sn_{0.50}$ was only obtained after sintering for 20 hours. In 2006, the synthesis was carried out in a graphite crucible. The products were then crushed into powders and hot pressed at 800 °C under 80 MPa for 5 hours.

Sb-doped and undoped $Mg_2Si_{0.50}Sn_{0.50}$ samples have been recently made by Gao et al. [19]. This was also confirmed by XRD. The required amounts of elemental Mg, Si and Sn powders (with an excess of 10 mol % Mg) were mixed. The mixtures were put in alumina crucibles, covered by boron oxide (B_2O_3) powder and compacted. The crucibles were placed in a chamber furnace, and the samples heated to 700 °C in air and kept at that temperature for 10 hours. After that, the samples were cooled to room temperature, separated from the B_2O_3 phases, crushed into powders, and sintered at 720 °C under 80 MPa for 2 hours.

Similar experiments were carried out for samples of different compositions by Chen et al. in 2011 [20]. They ground Mg, Si and Sn into powders and mixed them in a glove box. The nominal compositions of the $Mg_2Si_{1-x}Sn_x$ samples were x = 0.1, 0.2, 0.3, 0.4, 0.45, 0.55, 0.6, 0.7 and 0.8. For each sample, 4 g of the Mg-Si-Sn mixture was covered by 3 g of B_2O_3 powder in an alumina crucible, and heated at 700 °C for 10 h in a chamber furnace. Some of

the peaks in the X-ray diffractograms of all the samples, except for those with $x = 0.1$ and 0.8, were relatively broad or had shoulders. There was a phase separation for $0.3 \leq x \leq 0.45$. The porous, bulk products were crushed and ground. After hot-pressing in a graphite die at temperatures varying from 700 °C (for $x = 0.8$) and 840 °C (for $x = 0.1$) for 2 h under 80 MPa, peak splitting occurred for $0.2 \leq x \leq 0.45$. Extra Mg that was in the product before the hot-pressing had turned into MgO. They report that the difference in the miscibility gap in the system $Mg_2Si_{1-x}Sn_x$ among researchers is due to the use of different amounts of excess Mg.

Luo et al. [21] and Zhang et al. [22] have synthesized a single phase of $Mg_2Si_{0.50}Sn_{0.50}$, but their XRD peaks at this composition are a bit broader than those of their other phases. Luo et al. [21] mixed Mg, Si and Sn powders and made pellets, which were heated in a furnace under Ar atmosphere, allowing solid state reactions to occur. The products were densified by spark plasma sintering (SPS) at 650-700 °C at 40 MPa for 10 minutes, also in an Ar atmosphere. Zhang et al. [22] melted molar ratios of the three elements (with 8 wt. % excess Mg), crushed the products into powders and sintered them by SPS in a furnace at 700 – 750 °C under 60 MPa in vacuum. In both experiments, SPS greatly enhanced the mixing, which resulted in homogeneous solids.

Vidar Hansen's group at the Department of Science and Technology at the University of Stavanger, who is collaborating with the University of Oslo through the BATE group, is currently investigating the microstructure of $Mg_2Si_{1-x}Sn_x$ with TEM. The samples had nominal compositions of $x = 0.25$, 0.5 and 0.75, and were synthesized by a casting technique in an aluminium (Al) flux [23]. Chunks of solid Mg were covered in Al foil and heated in an Al melt, along with crushed Si powder and Sn pearls, at 900 °C. The flux was poured into a cast die and cooled in air. The cylinder-shaped casts were cut into square prisms, the edges were grinded and the specimens were analysed in an SEM. The Al matrices of the samples contained both Si-rich and Sn-rich $Mg_2Si_{1-x}Sn_x$ particles. The Sn-rich particles were larger than the Si-rich particles.

Thin films of $Mg_2Si_{1-x}Sn_x$ solid solutions were synthesized by plasma assisted co-sputtering for the first time in 2012, by Le-Quoc et al. [24]. Samples with compositions $x = 0.4$, 0.5 and 0.6 doped with silver (0.2 – 0.4 at. %) were made by depositing the elements from targets

onto SiO_2/Si substrates at room temperature. They studied their products with XRD and field emission SEM. Their products were polycrystalline thin films, with no signs of phase separation.

1.4 Thermoelectric figures of merit for doped and undoped systems

Table 1.1 shows a selection of figure of merits (*ZT*) for $Mg_2Si_{1-x}Sn_x$ obtained by different research groups. (Song et al. [25] and Aizawa et al. [26] prepared their samples by BMA, similarly to Song et al. [13].) The values are given for the compositions and temperatures at which the highest *ZT*s were measured. Table 1.2 represents the highest ZT for doped $Mg_2Si_{1-x}Sn_x$ obtained by certain research groups. Isoda et al. [18], Zhang et al. [4], Gao et al. [27] and Gao et al. [19] doped their samples with antimony (Sb), and Luo et al. [28] doped their samples with bismuth (Bi). Sb and Bi dopants are located on Si sites in $Mg_2Si_{1-x}Sn_x$ lattices.

Table 1.1: The highest ZT reported by different research groups, along with the compositions and temperatures at which they were obtained.

Research group	**Year**	**Compound**	**ZT**	**T (K)**
Riffel & Schilz [12]	1996	$Mg_2Si_{0.6}Sn_{0.4}$	0.03	298
Isoda et al. [17]	2004	$Mg_2Si_{0.5}Sn_{0.5}$	0.018	298
Song et al. [25]	2005	$Mg_2Si_{0.4}Sn_{0.6}$	0.057	653
Aizawa et al. [26]	2006	$Mg_2Si_{0.4}Sn_{0.6}$	0.13	650
Zaitsev et al. [3]	2006	$Mg_2Si_{0.6}Sn_{0.4}$	1.1	870
Song et al. [13]	2007	$Mg_2Si_{0.4}Sn_{0.6}$	0.13	653
Luo et al. [21]	2009	$Mg_2Si_{0.8}Sn_{0.2}$	0.1	490
Zhang et al. [22]	2010	$Mg_2Si_{0.4}Sn_{0.6}$	0.25	673
Chen et al. [20]	2011	$Mg_2Si_{0.55}Sn_{0.45}$	0.3	525

Table 1.2: The highest ZT of $Mg_2Si_{1-x}Sn_x$ reported by different research groups, along with the compositions and temperatures at which they were obtained.

Research group	Year	Compound	ZT	T (K)
Isoda et al. [18]	2006	$Mg_2Si_{0.5}Sn_{0.5}$ with 7500 ppm Sb	1.2	620
Zhang et al. [4]	2008	$Mg_2Si_{0.3925}Sn_{0.6}Sb_{0.0075}$	1.1	773
Luo et al. [28]	2010	$Mg_2Si_{0.8}Sn_{0.2}$ with 3 at. % Bi on Si sites	1.17	850
Gao et al. [27]	2011	$Mg_2Si_{0.6945}Sn_{0.3}Sb_{0.0055}$	0.55	620
Gao et al. [19]	2011	$Mg_2Si_{0.487}Sn_{0.5}Sb_{0.013}$	> 0.9	740

As can be seen in Tables 1.1 and 1.2, measured values of *ZT* vary greatly between the different research groups, more so for undoped systems. The highest values of *ZT* were obtained by research groups who carried out their thermoelectric measurements at a few hundred degrees above room temperature. All of the doped and undoped samples had compositions around $x = 0.4 – 0.6$, except those prepared by Luo et al. [21].

1.5 Structures of material systems

The reactants used in this project are magnesium (Mg), silicon (Si), tin (Sn), magnesium silicide (Mg_2Si) and magnesium stannide (Mg_2Sn). The reported crystal structures are hexagonal closest packing (hcp) for Mg, diamond type for Si, body centred tetragonal for Sn, and antifluorite for both Mg_2Si and Mg_2Sn (see Table 1.3). $Mg_2Si_{1-x}Sn_x$ is also reported to have an antifluorite type structure (see Fig. 1.4).

Table 1.3: The reported crystal structures, crystallographic space groups and lattice parameters of Mg, Si, Sn, Mg_2Si and Mg_2Sn.

Compound	Crystal structure	Space group	Lattice parameters (Å)
Mg	hcp	P63/mmc, no. 194	a = 3.20936, c = 5,2112 [29]
Si	diamond type	Fd-3m, no. 227	a = 5.43088 [30]
Sn	Body-centred tetragonal	I41/amd, no. 141	a = 5.831, c = 3.182 [31]
Mg_2Si	Antifluorite	Fm-3m, no. 225	a = 6.35119 [32]
Mg_2Sn	Antifluorite	Fm-3m, no. 225	a = 6.763 [33]

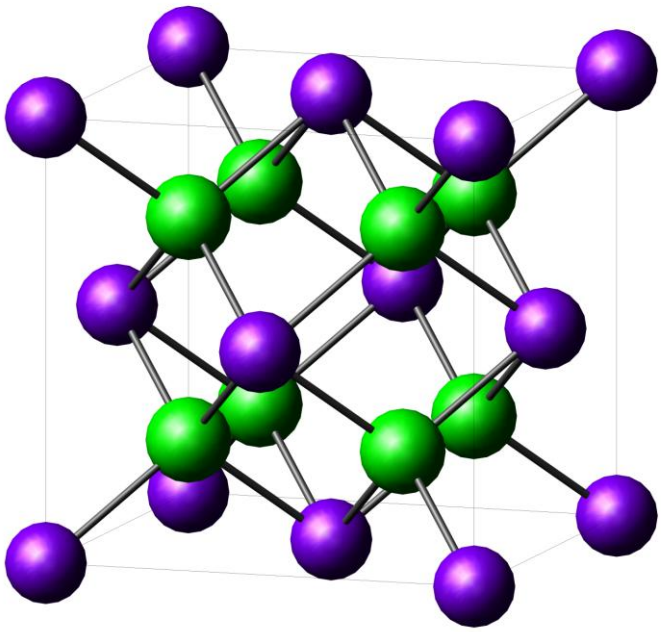

Figure 1.4: An illustration of a unit cell with the antifluorite structure, where Si- and Sn atoms (purple) are randomly distributed on the corners and faces of the cube, and all tetrahedral holes are filled with an Mg atom (green).

The lattice parameter (*a*) varies with composition in $Mg_2Si_{1-x}Sn_x$. It is reported to be 6.35119 Å for Mg_2Si [32] and 6.7630 Å for Mg_2Sn [33]. *a* varies linearly with *x* on the Si-rich side of the immiscibility gap, but there is a slight deviation to Vegard's law on the Sn-rich side [6] (see Fig. 1.7).

One way of describing the crystal structure of $Mg_2Si_{1-x}Sn_x$ is with a face centred cubic (*fcc*) lattice and a basis consisting of a $Si_{1-x}Sn_x$ atom on position 000, a Mg atom on ¼ ¼ ¼ and another Mg atom on -¼ -¼ -¼. The unit cell is a cube with anions (Si or Sn) randomly distributed on the corners and faces, and cations (Mg) in the tetrahedral holes. They are not really anions and cations, but the electron density is shifted away from the Mg atoms [31]. One could argue that the structure is in fact the fluorite structure, because the fluorite and the antifluorite structures have the same geometrical arrangement of the atoms. The only difference is that in the fluorite structure, it is the cations that are on the corners and faces of a cube, and anions in the tetrahedral holes. In order to make it easier to remember that the opposite is the case for $Mg_2Si_{1-x}Sn_x$, this structure will from now on be referred to as antifluorite type.

A Mg – Si phase diagram is presented in Fig. 1.5 [29], and a Mg – Sn phase diagram is presented in Fig. 1.6 [30].

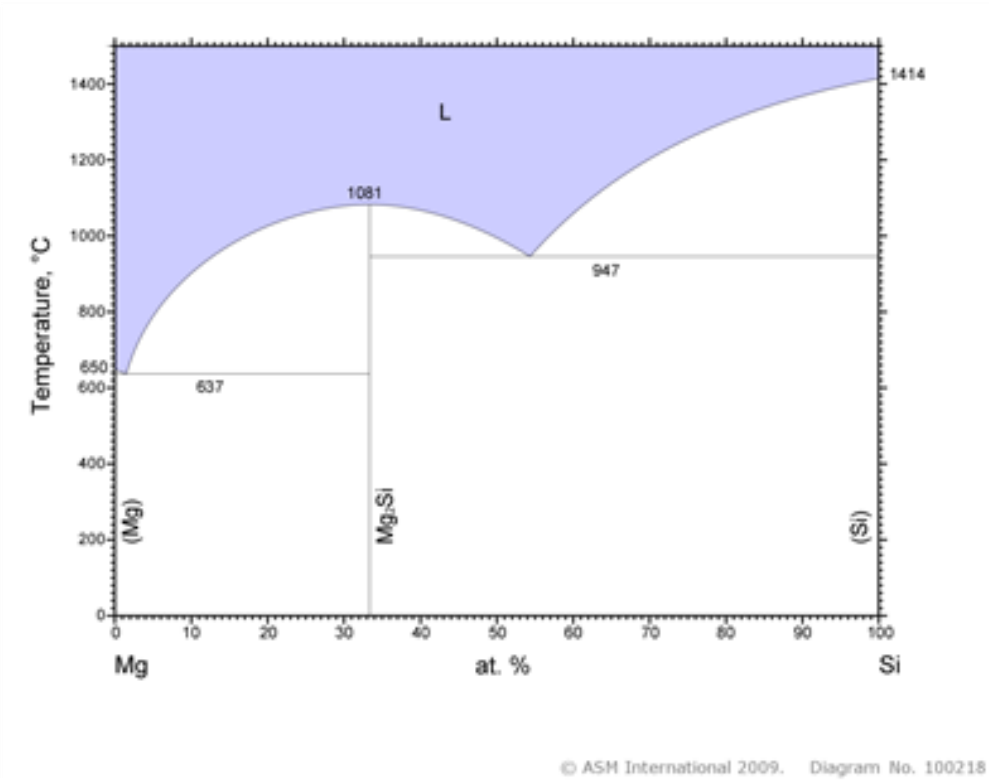

Figure 1.5: A Mg – Si phase diagram [29].

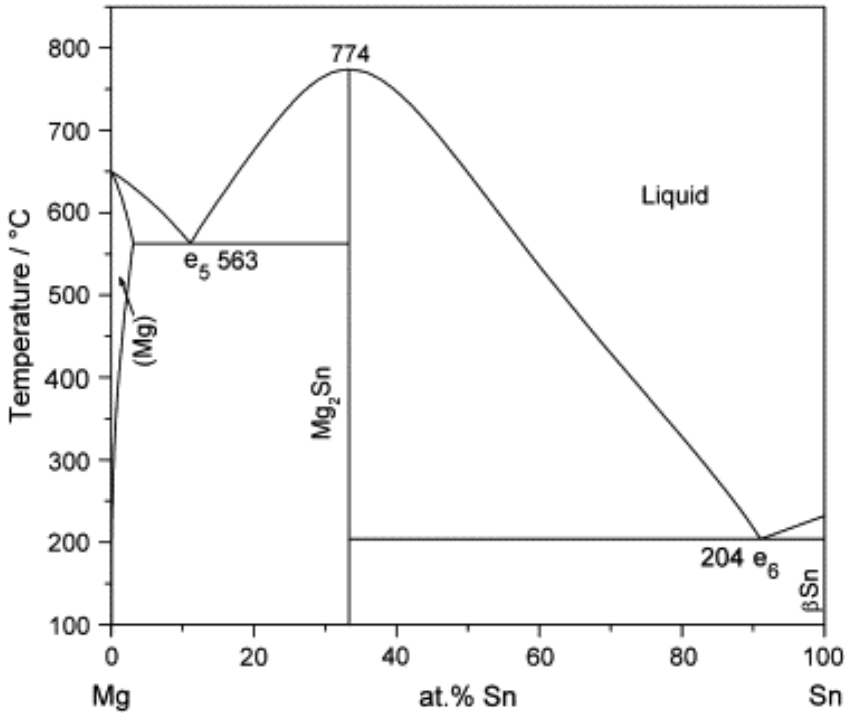

Figure 1.6: A Mg – Sn phase diagram [30].

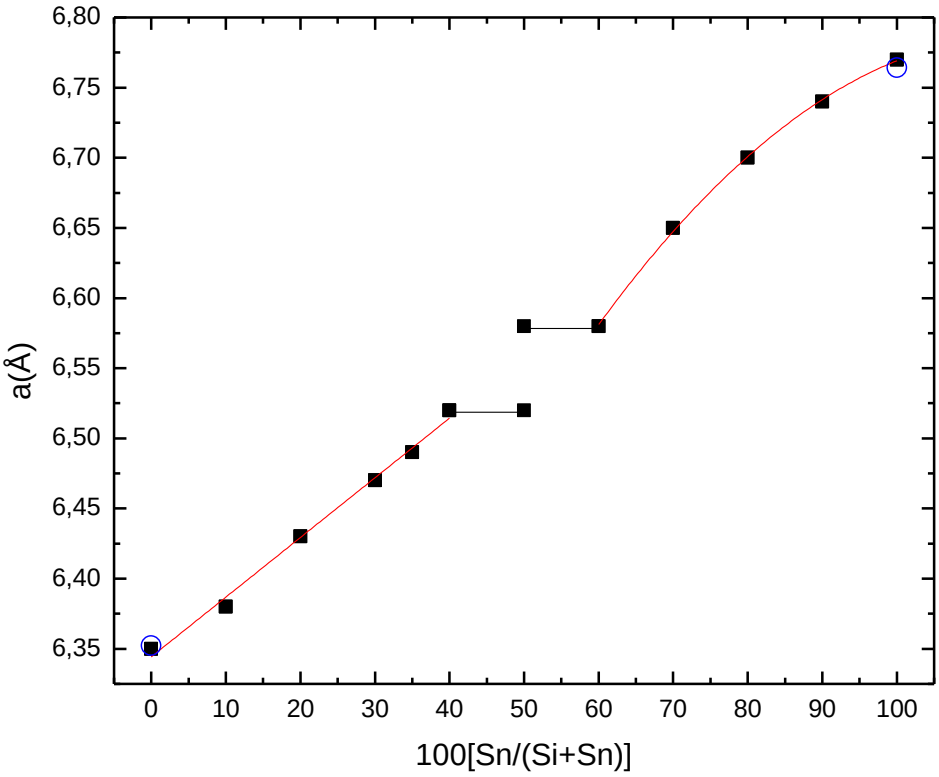

Figure 1.7: A curve of lattice constant vs. composition for $Mg_2Si_{1-x}Sn_x$ fitted to results obtained by Nikitin et al. [6].

2. An introduction to crystallography and diffraction

A very brief introduction to crystallography and diffraction is given, as it is necessary for understanding and interpreting TEM diffraction patterns.

2.1 Crystal structures and lattice symmetries

A crystal structure is described by a lattice and a basis (also known as a motive) at each lattice point. A lattice is a periodic array of mathematical points, defined by a lattice translation vector *t*.

$$t = ua + vb + wc \tag{2.1}$$

where ***a, b, c*** are three linearly independent vectors and *u, v, w* are integers.

In a perfect crystal, each point is associated with a basis, which could be an atom or a group of atoms [32]. Crystal lattices are usually divided into seven crystal systems or 14 Bravais lattices. Positions of atoms within a unit cell are given by a vector *r*.

$$r = xa + yb + zc \tag{2.2}$$

where $0 \leq x, y, z > 1$ for a unit cell with dimensions *a, b, c*.

Lattices in both real and reciprocal space may be described by symmetry operations. There are four macroscopic symmetry elements described by these operations, which superimpose a set of lattice points onto another:

- Identity (1): A lattice point is superimposed onto itself. Although this is obvious, one must not forget that this operation is necessary for all lattices.
- Rotation axes (1, 2, 3, 4 and 6): Lattice points are rotated around a centre of symmetry onto other lattice points. The rotation angle for an *n*-fold rotation axis is 360 °/*n*.
- Mirror planes (m): Lattice points are reflected onto another side of a mirror plane.

- Inversion centres (-1): Lattices with an inversion centre have a centre of symmetry. Lattice points that are in positions *x, y, z* with respect to the centre of symmetry are superimposed onto positions *-x,-y,-z*. Inversion centres are often combined with rotation axes (-2, -3, -4 and -6).

These symmetry elements describe 32 different crystallographic point groups. There are two microscopic symmetry operations, which also involve translations of lattice points:

- Screw axes (2_1, 3_1, 3_2, 4_1, 4_2, 4_3, 6_1, 6_2, 6_3, 6_4 and 6_5): A set of lattice points is superimposed onto another by rotation followed by translation along a vector parallel to the rotation axis. The large number and the subscript describe the rotation angle and translation distance, respectively.
- Glide planes (a, b, c, n, e and d): A set of lattice points are reflected onto the other side of a mirror plane, and then translated along a vector parallel to the mirror plane. The letter indicates the distance and direction of the translation.

By combining the macroscopic and microscopic symmetry elements, 230 crystallographic space groups can be described. As an example, the antifluorite structure has space group Fm-3m, where "F" indicates face-centering, the first "m" indicates a mirror plane parallel to {100} planes, -3 indicates a three-fold roto-inversion axis perpendicular to {111} planes, and the last m indicates a mirror plane parallel to {110} planes.

2.2 Diffraction from crystals

2.2.1 Bragg condition

Diffraction methods are very efficient for characterizing crystal structures. When a solid is irradiated with photons, electrons or neutrons, the incoming waves are scattered in the material. Photons are scattered by the electron clouds, neutrons are scattered by nuclear forces with atomic nuclei and by magnetic forces with magnetic moments, and electrons are scattered by the combined electrostatic potential of electron clouds and atomic nuclei. Planes of atoms will behave like semi-transparent, specularly reflecting surfaces. It has been proved that the nature of such mirror-like reflections are independent of the positions of the atoms on the plane relative to the incident beam at a given incident angle [33]. Within a set of parallel planes of atoms, each plane transmits and reflects some of the incoming waves. Diffraction occurs when specularly reflected waves from adjacent planes interfere with each other

constructively. Constructive interference occurs when the path difference between waves reflected from adjacent planes is equal to an integer multiple of the wavelength. See Fig. 2.1. This is given by Bragg's law:

$$2d \sin\theta = n\lambda \tag{2.3}$$

where d is the interplanar spacing, θ is the semi-angle between incident and reflected waves, n is an integer and λ is the wavelength of the diffracting waves.

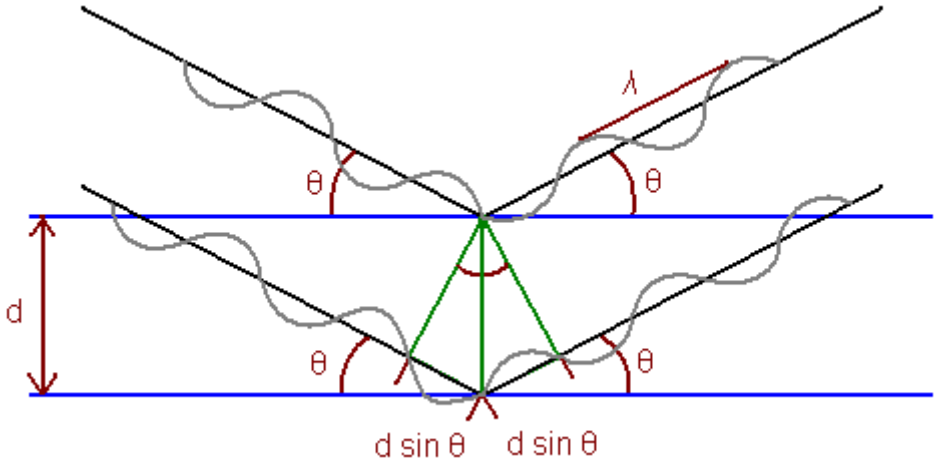

Figure 2.1: Constructive interference occurs when the path difference between waves reflected from adjacent planes, $2d\sin\theta$, is equal to an integer multiple of the wavelength, $n\lambda$.

2.2.2 Reciprocal space

A crystal with a certain lattice in real space has another lattice in reciprocal space. Diffraction patterns from crystals are two-dimensional projections of such three-dimensional reciprocal lattices. The relation between reciprocal lattice vectors a^*, b^*, c^* and real space lattice vectors a, b, c is presented in equation (2.4).

$$\begin{aligned} \boldsymbol{a^* = b \times c / V} \\ \boldsymbol{b^* = c \times a / V} \\ \boldsymbol{c^* = a \times b / V} \end{aligned} \tag{2.4}$$

where $V = \boldsymbol{a} \cdot (\boldsymbol{b} \times \boldsymbol{c})$ is the volume of the unit cell in real space[1]. The lattice points are defined by a reciprocal lattice vector $\boldsymbol{g}$:

$$\boldsymbol{g} = h\boldsymbol{a^*} + k\boldsymbol{b^*} + l\boldsymbol{c^*} \tag{2.5}$$

where h, k, l are integers. Crystallographic planes in real space are indexed with Miller indices (hkl). Such a plane intersects a unit cell in real space at position [a/h b/k c/l]. Parallel planes scatter coherent waves into the same point, so that a set of planes in real space are equivalent to a point in reciprocal space.

2.2.3 The Ewald sphere construction

The Ewald sphere construction consists of a sphere in reciprocal space with radius $k = 1/\lambda$ and a reciprocal lattice (see Fig. 2.2). The reciprocal lattice belongs to the material being irradiated. $\boldsymbol{k_I}$ and $\boldsymbol{k_D}$ are the wave vectors of the incident beam and diffracted beams, respectively, and are parallel to the propagation direction of the waves they represent. $\boldsymbol{k_I}$ ends in the origin of the reciprocal lattice. The purpose of this construction is to show which reflections will appear in a diffraction pattern. Each lattice point that intersects the sphere corresponds to a reflection that satisfies the Bragg condition. In fact, $\boldsymbol{\Delta k} = \boldsymbol{g}$, where $\boldsymbol{g}$ is a reciprocal lattice vector and $\boldsymbol{\Delta k} = \boldsymbol{k_D} - \boldsymbol{k_I}$ is the difference between the diffracted wave and the incident wave, is another form of Bragg's law. The set of intersected points on the same reciprocal lattice plane as the point in the origin is called the zero order Laue zone (ZOLZ). The plane with intersected points above the ZOLZ is called the first order Laue zone (FOLZ), the plane above that the second order Laue zone (SOLZ), and so on. All Laue zones greater than the ZOLZ are referred to as higher order Laue zones (HOLZ).

[1] In solid state physics and quantum mechanics, reciprocal values (lattice vectors, wave vectors, indices etc.) often have a factor of 2π, which is usually omitted by material scientists.

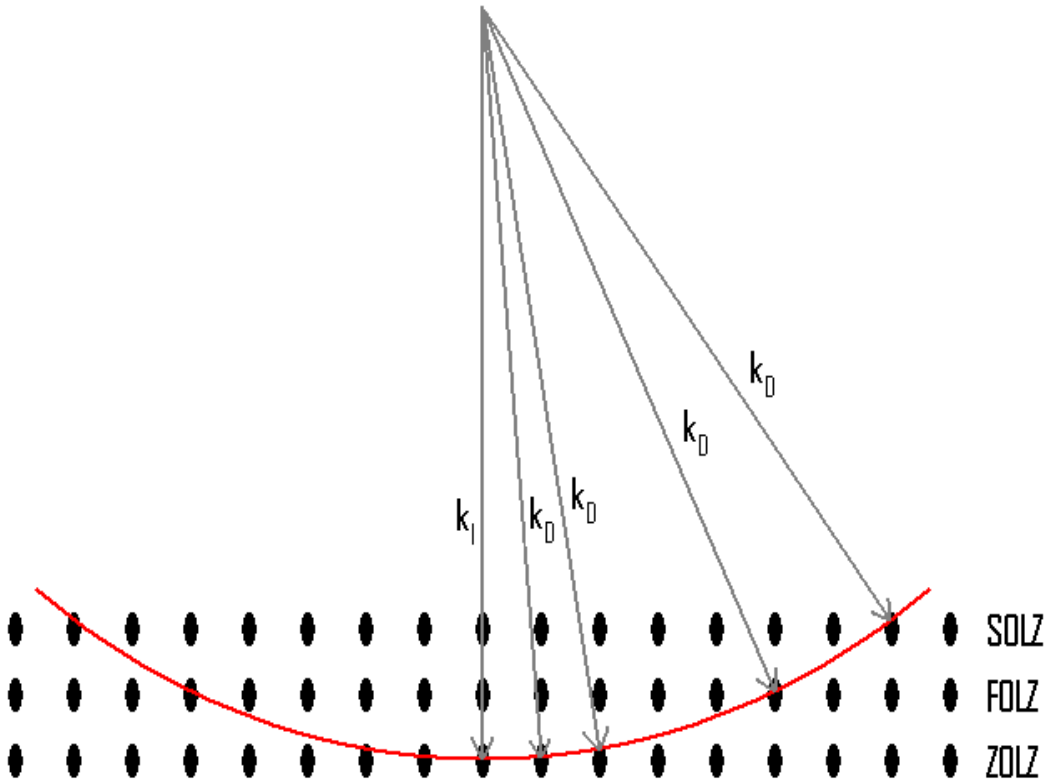

Figure 2.2: A two-dimensional projection of an Ewald sphere construction. Bragg's condition is satisfied when the difference between a diffracted wave vector and the incident wave vector, $\boldsymbol{\Delta k} = \boldsymbol{k_D} - \boldsymbol{k_I}$, is equal to a reciprocal lattice vector, $\boldsymbol{g}$.

Electron waves have very short wavelengths (λ = 0.000251 Å for 200 kV electrons), so the Ewald sphere is large. Large Ewald spheres are almost flat at surfaces of specimens, and therefore intersect a lot of points in reciprocal space. In very thin specimens, the reciprocal lattice points are rods. The rods have their long dimension parallel to the plane of the surface. When such specimens are irradiated with electron waves in a TEM, some of the rods may intersect the Ewald sphere, although they do not satisfy Bragg's condition. Thus, these points may appear on electron diffraction patterns. If the incident waves are X-rays, the Ewald sphere becomes smaller, because X-rays have much longer wavelengths (λ = 1.54 Å for Cu $K\alpha_1$ X-rays) than electron waves. Hence, there are relatively few lattice points that satisfy the Bragg condition and will appear in XRD patterns.

2.2.4 Structure factors

The kinematical intensities of Bragg reflections are proportional to the square of the structure factor of the unit cell. The structure factor, *F*, is calculated by adding scattering factors, *f*, of

all the atoms or ions, while taking their respective positions into account. The general equation for calculating structure factors is as follows:

$$F_{(h,k,l)} = \sum_{j=1}^{n} f_{(j)} \exp\left[2\pi \cdot i(hx_{(j)} + ky_{(j)} + lz_{(j)})\right] \quad (2.6)$$

where *x*, *y*, *z* represent the position of atom *j* with scattering factor *f*, and *h*, *k*, *l* are the indices of the Bragg reflections [32].

As an example, the structure factor is calculated for solid solutions of $Mg_2Si_{1-x}Sn_x$ below (see equation 2.7). Each reciprocal lattice point in $Mg_2Si_{1-x}Sn_x$ is associated with an $Si_{1-x}Sn_x$ atom on the point and two Mg atoms displaced [¼ ¼ ¼] and [-¼ -¼ -¼] from it. The structure factor is calculated from equation 2.6.

$$F_{hkl} = \left[x f_{Sn} + (1-x) f_{Si} + f_{Mg}\left(e^{\frac{\pi i}{2}(h+k+l)} + e^{-\frac{\pi i}{2}(h+k+l)}\right)\right] \times \left[1 + e^{\pi i(h+k)} + e^{\pi i(h+l)} + e^{\pi i(k+l)}\right] \quad (2.7)$$

The term in the round brackets after f_{Mg} can be simplified by the following rule:

$$e^{ix} + e^{-ix} = 2\cos x \quad (2.8)$$

The structure factor can then be expressed as follows:

$$F_{hkl} = \left[x f_{Sn} + (1-x) f_{Si} + 2 f_{Mg} \cos\left(\frac{\pi}{2}(h+k+l)\right)\right] \times \left[1 + e^{i\pi(h+k)} + e^{i\pi(h+l)} + e^{i\pi(k+l)}\right] \quad (2.9)$$

Electrons interact more strongly with atoms in a sample than X-rays do. As previously mentioned, while incident X-rays are only scattered by electron clouds of atoms or ions, electron waves are scattered by both electron clouds and atomic nuclei. Electron scattering factors f_e are related to X-ray scattering factors f_x by the Mott formula:

$$f_e = C\left(\frac{Z - f_x}{q^2}\right) \quad (2.10)$$

where *C* is a constant, *Z* the atomic number of the atom and *q* the momentum transfer. For simplicity, it was assumed that $Mg_2Si_{1-x}Sn_x$ contains neutral atoms when carrying out the

calculations above. The electron scattering factors, which depend on interplanar distances in the crystals, were found from Doyle and Turner [34].

Although an *fcc* lattice is body centred cubic (*bcc*) in reciprocal space, the presence of Mg atoms in the tetrahedral holes change the relative intensities of reflections in diffraction patterns. Equation 2.11 shows how to calculate the composition at which certain reflections disappear.

$$x = \frac{f_{Si} - 2f_{Mg}\cos\left(\frac{\pi}{2}(h+k+l)\right)}{f_{Sn} - f_{Si}} \tag{2.11}$$

Based on calculations carried out in this project for solid solutions of $Mg_2Si_{1-x}Sn_x$, 200 reflections are expected to disappear for $x = 0.28$ in XRD patterns and for $x = 0.50$ in electron diffraction patterns.

3. Synthesis methods and characterization techniques

The following describes the synthesis methods and characterization techniques used in the present work.

3.1 Synthesis

3.1.1 Solid state synthesis

In this text solid state synthesis refers to syntheses where the main reactants and products are in the solid state. Some generalise the term by including all synthesis in which at least one of the reactants is a solid (such as solid-gas reactions, decomposition, dehydration and intercalation reactions) [35], and use the terms ‘ceramic method’ or ‘shake and bake’ if all reactants are solids during reaction. The generalisation of the term “solid state synthesis” will be used for the synthesis of Mg_2Si from elemental Mg and Si, although Mg reacts in the liquid or gas phase.

Solid state synthesis is a popular technique for synthesizing powders, because it is notorious for its simplicity, the reactants are usually readily available, and it doesn’t need chemicals that will not end up in the product. The main disadvantages of the method are that it requires high temperatures, reactants may react with contaminations in the containers or with the container itself, and the product may be nonhomogeneous.

Many solids do not react with each other at room temperature. Even if it is thermodynamically favourable for them to react, the reactions are hindered by kinetics. The kinetic barrier can sometimes be overcome by increasing the temperature of the system. If the temperature is raised high enough, quite often to approximately 2/3 of the melting point in Kelvin of the reactant with the lowest melting point, atoms or ions of the different solids diffuse into adjacent particles to form new solid particles. The reaction rates depend on the contact area of the reactants, the nucleation rates of the product, and the diffusion rates through products and intermediate layers. Particle size and shape strongly influence reaction times; high surface areas are desirable [35].

Solid state synthesis is sometimes confused with sintering, where a powder or solid, often a product of solid state synthesis, is consolidated and densified when it is heated to a temperature below its melting point or solidus. However, a slight amount of sintering always occurs during solid state reactions, and vice versa. Sintering or hot pressing, which is sintering under pressure, is necessary if bulk samples are needed, e.g. for measuring thermoelectric properties.

3.1.2 Solidification of bulk materials from a homogeneous melt

The morphology of a product that has been solidified from a homogeneous melt depends on the rate of cooling. When a melt is cooled, nucleation and crystal growth occurs. The temperature range at which crystal growth occurs is higher than that for homogeneous nucleation (see Fig. 3.1 [36]). Heterogeneous nucleation, e.g. nucleation at impurities, dust and edges, occurs at higher temperatures than homogeneous nucleation. If a melt is cooled slowly, crystal nuclei have time to grow into large crystals, and the system is closer to thermodynamic equilibrium. If, however, a melt is quenched, the nuclei will not have enough time to grow into large homogeneous crystals. The tendency of a melt to become a crystalline or amorphous solid does of course also depend on the chemistry of the liquid, not only on the cooling rate.

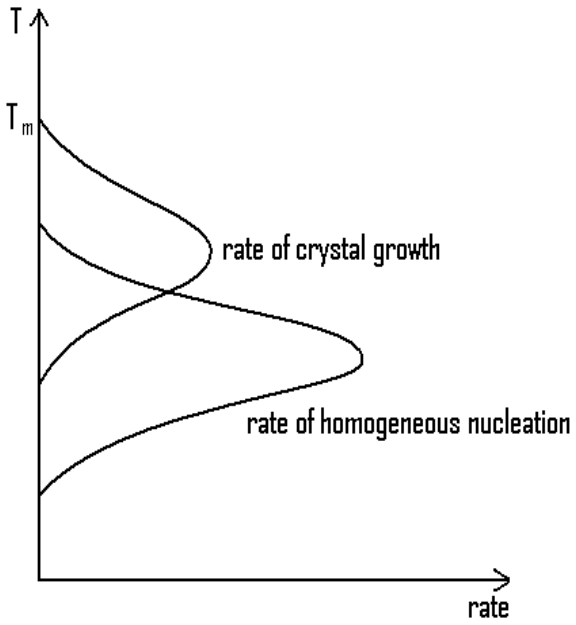

Figure 3.1: The tendency of nucleation and crystal growth as a melt is cooled. (Adapted from [36], p. 632.)

3.1.3 Flux synthesis

When reactants are mixed in a liquid flux medium, cooling may result in single crystals. The medium can either be one of the reactants or something completely different from all of the reactants. If the medium is one of the reactants, it has to be in excess. Nuclei are formed, and atoms or ions travel through the flux medium to the nuclei, allowing single crystals to grow, as long as there is enough of the flux medium to keep the crystals separated from each other. The size of the crystals depends on the identity of the reactants and fluxing medium, and the cooling rate.

3.2 Characterization

3.2.1 Powder X-ray diffraction

XRD can be used for determining the overall structure of crystalline solids. In powder XRD a powder of a sample is illuminated with monochromatic X-rays. The X-rays scatter elastically. In X-ray diffractometers diffracted (reflected or transmitted) X-rays are detected by a moveable or stationary detector. Fig. 3.2 shows a schematic of an X-ray diffractometer with

Bragg-Brentano θ-θ geometry. The X-ray source and detector move while the irradiated sample is rotating.

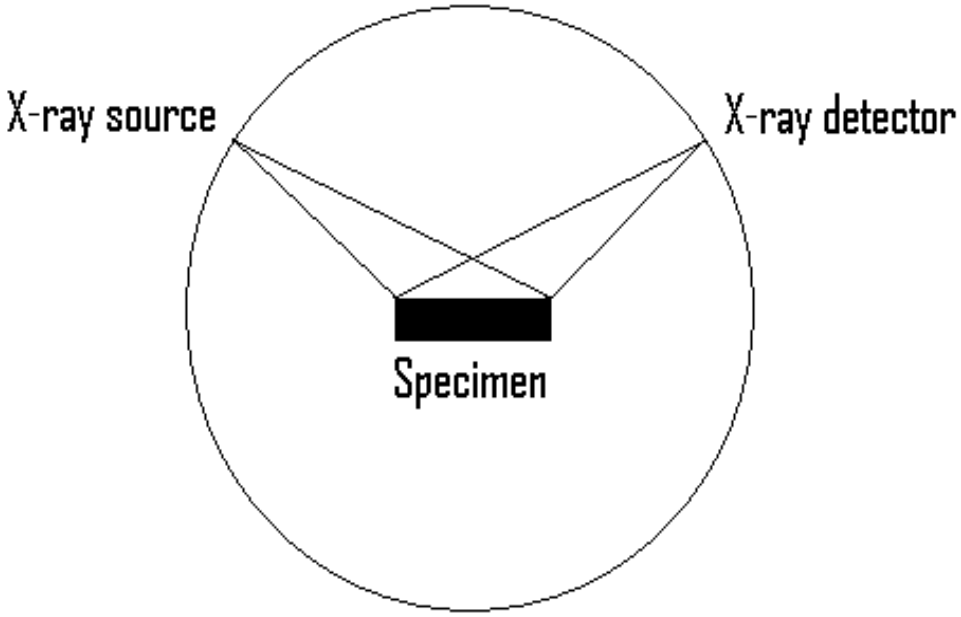

Figure 3.2: A schematic of an X-ray diffractometer with Bragg-Brentano geometry.

3.2.2 Optical microscopy

In optical microscopes and stereomicroscopes, samples are illuminated with visible light and images obtained from some of the light scattered by the specimen are magnified. Fig. 3.3 shows an overview of a typical reflection microscope [38]. The sample is illuminated from above (as in the figure) or below, and a magnified image of the reflected light is observed. Reflection microscopes can provide bright field (BF) and dark field (DF) images (not to be confused with BF and DF imaging in TEM, see section 3.2.4.1). In BF illumination in optical microscopy, light that is scattered diffusively does not scatter into the objective lens. In DF illumination, the middle of the cone of light illuminating the sample is blocked. Only the outer layer of the cone of light illuminates the sample surface. Diffusely scattered light will now be scattered into the objective lens and appear bright.

In stereomicroscopes, the light illuminates the sample from an angle instead of from directly above (or below). There are two objective lenses. The image of the specimen observed with the left eye and that of the right eye are viewed from different angles, resulting in a three-dimensional image. If the illuminating light and the objective lens are on the same side of the

specimen plane, specularly reflecting surfaces appear dark, since the light is reflected away from the objective lens above the samples, as opposed to reflection microscopes where such surfaces appear shiny.

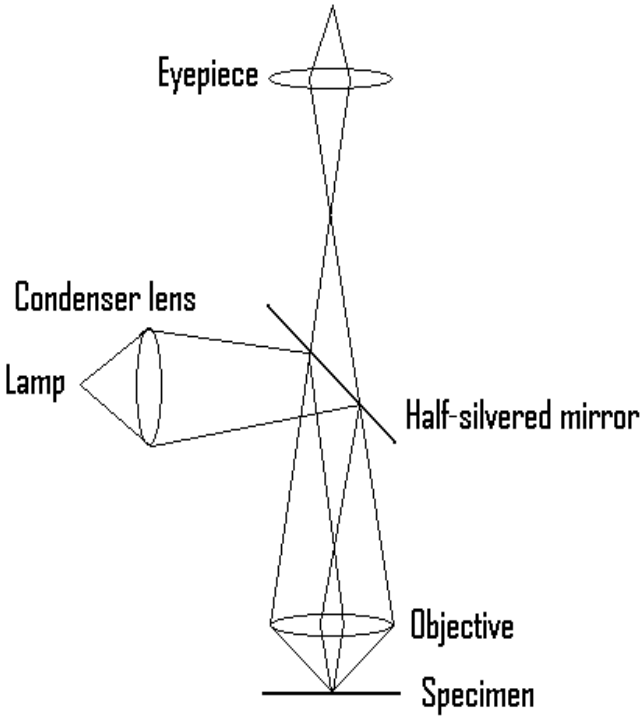

Figure 3.3: An overview of a typical optical reflection microscope. (Adapted from [38], p. 135.)

The main advantages of optical microscopy are that it is non-destructive, provides large coloured images so that it is easy to get an overview of a whole sample, and sample preparation is relatively easy. The main disadvantage is the poor spatial resolution. This is because wavelengths of visible light are a few 100 nm, whereas interatomic distances in solids are a few Ångstrøms. In order to obtain atomic resolution, the illuminating media has to have wavelengths shorter than or of the same order of magnitude as the atomic structure of the materials in the specimen. Another weakness is the low depth of focus, especially at high magnifications. However, this problem can be overcome by using a multifocus function. A sequence of pictures is taken, while step-wise varying the focus parameter. A computer program makes a new image by combining the best focused parts from all of the images.

3.2.3 Scanning electron microscopy

SEM is a very versatile instrument in the field of materials science. Just as optical microscopy (but to a lesser extent), it is a non-destructive method, the samples are easy to prepare, and it is very effective for studying large samples. SEMs have a depth of focus much greater than optical microscopes, and can provide information about topography, morphology, chemistry, crystallography and grain orientations.

Fig. 3.4 shows an overview of the most important parts in a SEM. At the top of the microscope column, electrons are emitted from an electron gun by thermionic emission (tungsten filaments or lanthanum hexaboride (LaB_6) crystals) or electron tunnelling (field emission guns (FEGs)). The surface of the specimen is scanned with an electron probe in a raster pattern. Secondary electrons (SE), backscattered electrons (BSE) and characteristic X-rays are the most important detected signals. The resolution is determined by the volume from which the signal electrons or X-rays are formed, and so SEs result in greater resolution than BSEs, which in turn result in greater resolution than X-rays. Both intensity and resolution are affected by how the emitted electrons and X-rays reach the detector.

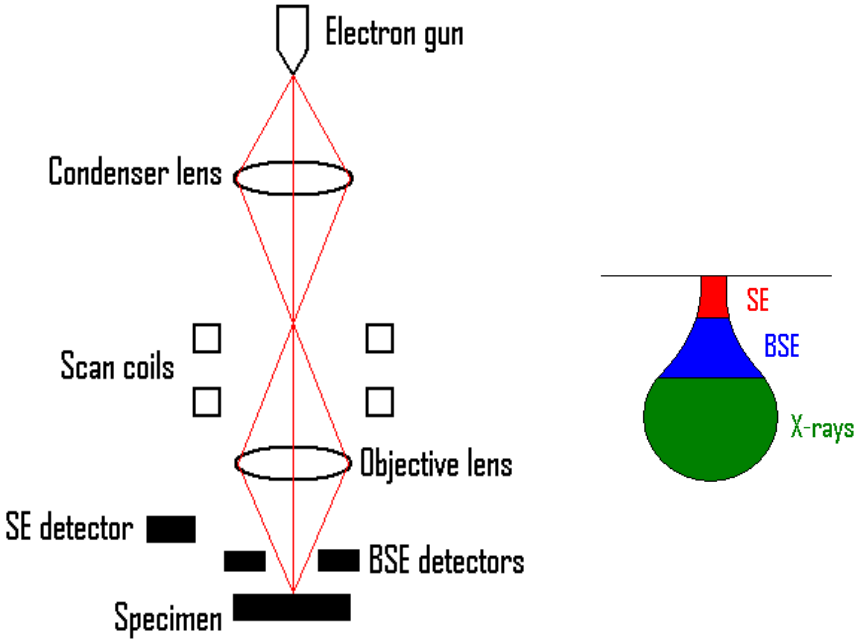

Figure 3.4: Left: The main components of a SEM. The red lines represent electron beams. Right: The distribution of SE-, BSE- and characteristic X-ray emissions that occur inside the specimen (right). Other kinds of signals have been omitted in the illustration. For samples containing mostly heavy elements, the interaction volume is more disc-shaped, rather than pear-shaped.

An SE is created by inelastic scattering events when an incoming electron kicks out a weakly bound electron from outer orbitals of an atom in the sample. SEs are of low energy, but there are many of them, more than the number of incoming electrons. Information about the topography of the sample can be obtained from SE images, because the surface constitutes a large part of the interaction volume of SEs. Only SEs near the surface may escape from the sample, and therefore topographical information is obtained. If the electron is knocked out of an atom near the surface, it is called an SE1. If it results from a collision with a BSE that has returned to the surface, it is called an SE2. The scattered electron that was a BSE before such a collision is also called an SE2, if it has lost enough energy. SE1s result in higher spatial resolution than SE2s, due to the smaller emission volume.

Some incoming electrons are scattered by electrostatic interactions with the nuclei of the atoms in the sample. Such electrons are called backscattered electrons (BSEs), and are of higher energy than SEs, because they occur from elastic scattering events. If the path of a BSE is changed by almost 180 ° and it escapes from the surface, the electron reaches the BSE detector and contributes to the BSE image. If the electron was backscattered by only one atom it is called a BSE1, but if the backscattering is due to more than one scattering event it is a BSE2. BSE1s provide images of higher resolution than those of BSE2s, because of the smaller excitation volume of BSE1s. There are far fewer BSEs than SEs. BSEs provide information about the average atomic number, and also (to a lesser extent) topographical information. The brighter the part of a material appears in a BSE image, the greater the average atomic number.

Emitted X-rays provide information about the chemistry of samples. When an incoming electron knocks out an electron in an atomic orbital of low energy, an electron from a higher energy orbital will fall down to replace the missing electron in order to keep the total energy as low as possible. This results in the emission of an X-ray photon or an Auger electron. Each chemical element has its characteristic set of electron transition energies and X-ray emission. The spatial resolution of emitted X-rays is poor compared to that of SEs and BSEs. Characteristic X-ray analyses can be performed on a single spot (spot analysis) for quantitative analysis, or on spots along a line (line scan) or on whole images (elemental mapping) to give a qualitative overview of where the different elements are.

3.2.4 Transmission electron microscopy

Specimens are irradiated with electrons in TEMs and SEMs. The theoretical resolution limit is greatly improved with electron waves, as their wavelengths are much shorter than those for visible light (λ = 0.000251 Å for 200 kV electrons). However, the theoretical limit is far from reached, because of aberrations in the electromagnetic lenses, in particular spherical aberration [39].

TEMs are used for imaging, diffraction and spectrometry. Fig. 3.5 shows an illustration of the types of detectable signals when a specimen is irradiated with electrons. The most important ones are transmitted electrons and characteristic X-rays. In TEM, chemical analysis is performed by EDS as in SEMs, but with better spatial resolution and weaker intensities. The spatial resolution is greater and the intensity of emitted X-rays are worse in TEMs because characteristic X-ray emission comes from smaller areas.

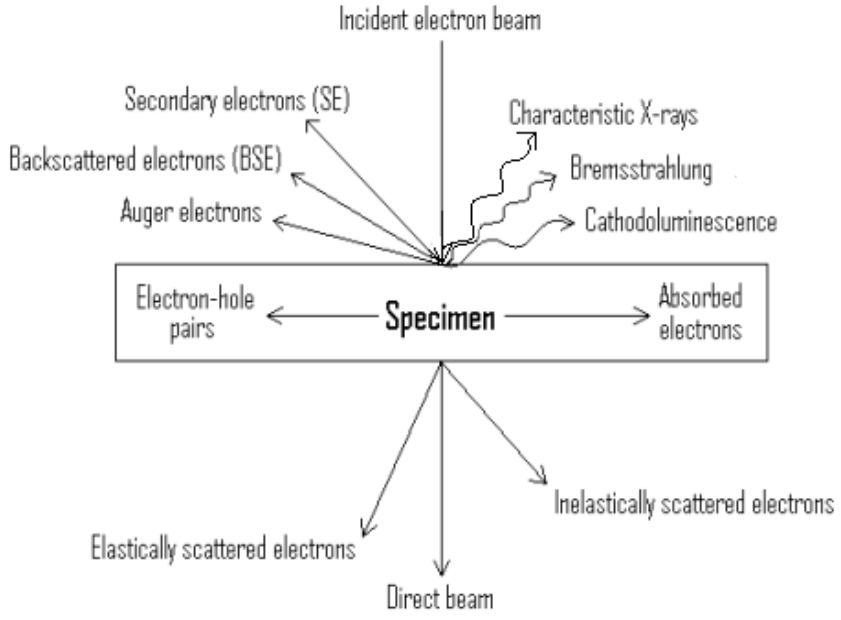

Figure 3.5: A schematic of detectable signals in a TEM specimen.

Electrons are emitted from an electron gun by thermionic emission or electron tunnelling (see chapter 3.2.3). The electron beam is focused by electromagnetic lenses and limited by apertures. The electromagnetic lenses create magnetic fields, which rotate images of electron

beams along the optical axis in the TEM. The brightness and shape of the beam is controlled by the first and second condenser lenses and apertures. The specimen is between the poles of the objective lens. Electrons travel through the objective lens pre-field before illuminating the specimen. Then the transmitted electrons enter the objective lens post-field, which focuses the image onto the image plane (see Fig. 3.6). It is the exit plane waves of the electrons that are imaged, not the specimen itself. The exit plane waves are Fourier transformed into the back focal plane (BFP) of the objective lens. The Fourier transformed waves are diffraction patterns. This pattern is inversely Fourier transformed into the image plane, which is an enlarged image of the exit plane waves. After the objective lens, the electrons travel through intermediate lenses and the projector lens. In imaging modes, the first intermediate lens is set to a strength in such a way that the image plane is projected onto the viewing screen in the TEM. For diffraction techniques, the first intermediate lens is weakened so that the diffraction pattern in the BFP is projected onto the viewing screen.

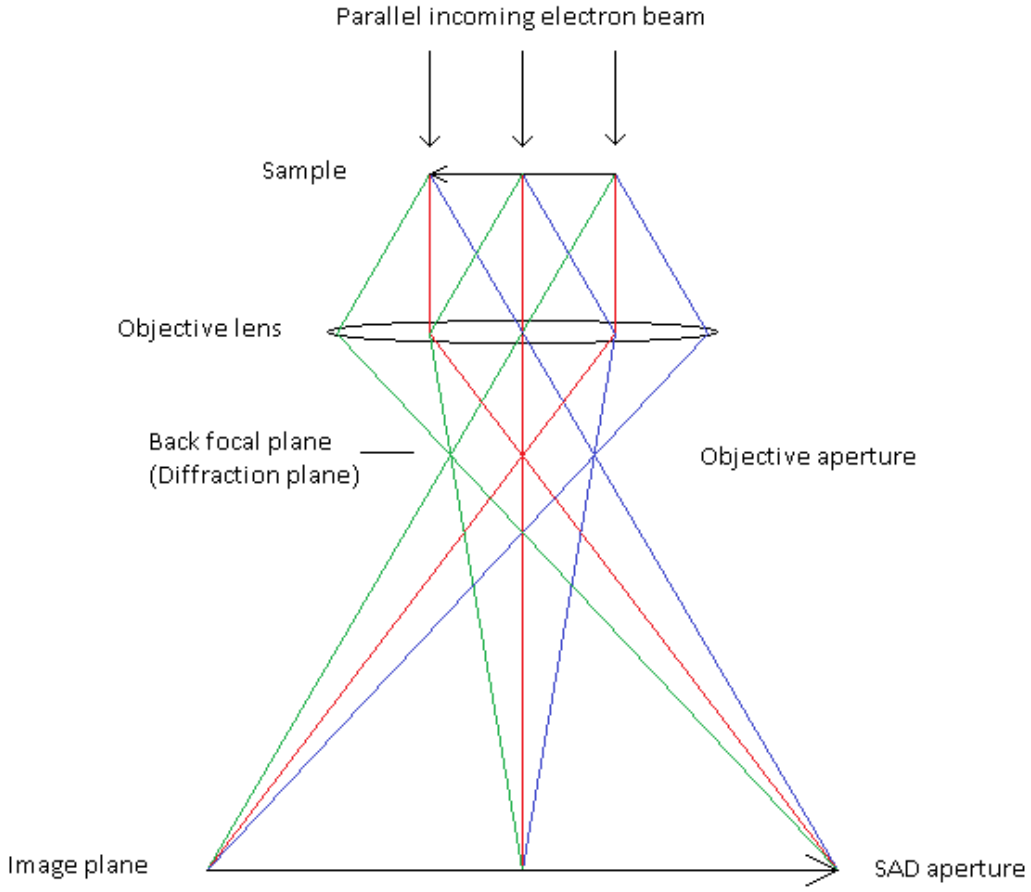

Figure 3.6: Ray diagrams showing trajectories of electron beams after transmitting through a specimen in a TEM. The objective aperture and SAD aperture are in the BFP and image plane, respectively.

3.2.4.1 Imaging techniques

The objective aperture in the BFP can be used to enhance image contrast. Such diffraction contrast occurs when the objective aperture limits transmitted electrons to those that have been diffracted in a certain direction. If only the direct beam (such as the red beam in Fig. 3.6) is allowed to pass through, the resulting image is called a bright field (BF) image. If the electron beam is tilted, so that another diffracted beam (such as the green or blue beams in Fig. 3.6) travels through the aperture, a dark field (DF) image is formed.

High resolution transmission electron microscopy (HRTEM) uses phase contrast for imaging at atomic resolution. The incident electron beam is parallel to the optic axis, large apertures are used in the BFP, and the image is slightly underfocused. The intensity of a wave is proportional to the square of the wave function. By squaring a wave function, all of the phase information disappears. However, electromagnetic lenses are not perfect. Phase contrast is converted into amplitude contrast by combining the effects of lens aberrations and defocusing images [40]. This is known as through-focus imaging.

3.2.4.2 Diffraction techniques

The two main diffraction techniques are selected area electron diffraction (SAED) and convergent beam electron diffraction (CBED). In both methods, the BFP of the objective lens in the TEM is imaged onto the viewing screen. The incident electron beams are parallel in SAED patterns and convergent in CBED patterns.

In SAED, a selected area diffraction (SAD) aperture is inserted in the image plane in the TEM. By inserting it, transmitted electron waves are limited to those that exit from a selected area of the specimen. SAD patterns consist of spots, and each spot corresponds to a reflection from a crystallographic plane. Distances between the central beam, 000, and diffracted reflections, *hkl*, are used as input for calculating interplanar distances in crystals, which in turn can be used to calculate crystal lattice parameters. Fig. 3.7 shows the geometry that is used to calculate distances between planes from diffraction patterns. A distance R in a diffracted pattern is related to an interplanar distance d by the following equation:

$$Rd = L\lambda \tag{3.1}$$

where L is the camera length, i.e. the distance between the specimen and viewing screen, and λ is the wavelength of the electrons. This approximation holds, because the $\theta_B << L$.

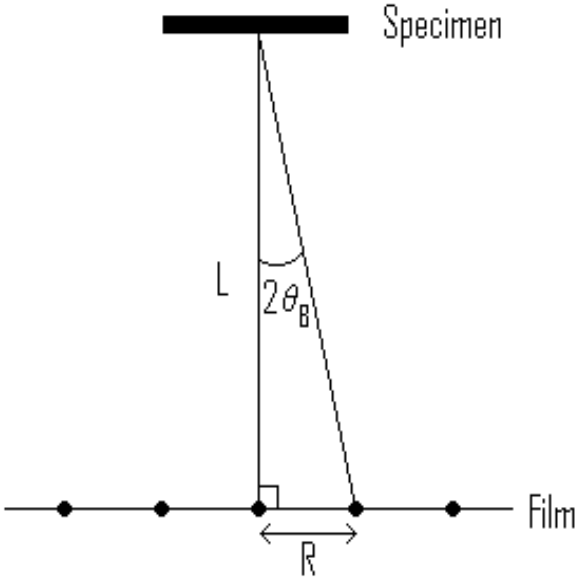

Figure 3.7: Geometry showing the relation between camera length, *L*, and measured distance between the direct beam and a diffracted beam, *R*.

The other common diffraction technique is convergent beam electron diffraction (CBED). In CBED mode the electron beam illuminating the specimen is converged, resulting in the Bragg reflections becoming large discs in the diffraction plane (see Fig. 3.8). CBED patterns contain three-dimensional information, whereas SAD patterns only contain two-dimensional information.

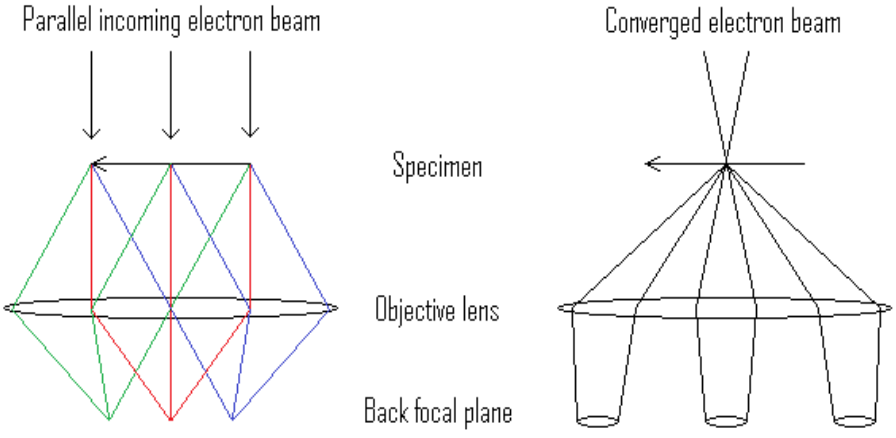

Figure 3.8: A comparison of the diffraction techniques SAD (left) and CBED (right).

In CBED patterns, screw axes and glide planes result in lines within discs next to the central disc. Many CBED patterns are needed if the analysed structure is unknown. Therefore, tilt series are necessary. The specimen is tilted along the main axis and diffraction patterns are recorded together with tilt data.

3.2.4.3 Dynamical effects

The theory of electron diffraction presented in this text so far considers kinematical scattering. Electrons are only scattered from a plane once before exiting the specimen. This approximation holds only for very thin specimens. The theory goes very well with specimens thinner than 5 nm, but can be used for samples with thicknesses < 50 nm. Dynamical scattering events are important in thicker specimens, because electrons are more likely to scatter multiple times within thick samples. Double scattering in single crystals may result in SAD patterns with kinematically forbidden reflections. Electrons that are scattered by a plane with Miller indices ($h_1k_1l_1$), may subsequently behave as a new incoming electron wave and be scattered by another plane with indices ($h_2k_2l_2$) in the same crystal or by a plane from another crystal. As shown by summing reciprocal lattice vectors corresponding to these planes, a new reflection may appear in the SAD patterns (see equation 3.2).

$$g_{h_1k_1l_1} + g_{h_2k_2l_2} = g_{(h_1+h_2)\,(k_1+k_2)\,(l_1+l_2)} \tag{3.2}$$

If the specimen is tilted out of a zone axis, reflections caused by multiple scattering may disappear from diffraction patterns.

4. Experimental

4.1 Reactants, atmospheres and tools

4.1.1 Materials and liquids

An overview of the materials and liquids that were used for synthesis and sample preparation is presented in Table 4.1.

Table 4.1: The materials and liquids used for synthesis and specimen preparation, including relevant information about purity, concentration, m.p., b.p. and manufacturer.

Materials & liquids	**Comments**	**Company**
Absolute ethanol prima (C_2H_5OH)	99.5 % concentration	Kemetyl Norge AS [41]
Acetone (C_3H_6O)	GPR Rectapur > 99.5 % concentration	VWR International AS [42]
Boron oxide (B_2O_3)	powder purity > 97 % melting point 450 °C boiling point 2202 °C	Fluka [43]
Crystal bond 509		Agar Scientific [44]
Demotec 33 resin		Demotec [45]
Diamond polishing lubricant, Green		Struers [46]
Diamond polishing lubricant, Yellow		Struers [46]
DuroCit resin	made by mixing DuroCit powder and liquid	Struers [46]
Gatan G1 epoxy		Gatan [47]
Isopropanol prima ($(CH_3)_2CHOH$)	pharma grade	Kemetyl Norge AS [41]
Magnesium (Mg)	45-250 µm powder purity > 99.8 % melting point 650 °C boiling point 1091 °C	Goodfellow [48]
Methanol (CH_3OH)		VWR International AS [42]
Silicon (Si)	wafers solar grade melting point 1410 °C	unknown origin
Tin (Sn)	zone refined sticks purity = 99.999 % melting point 232 °C	Fluka [43]
Toluene (C_7H_8)	100 % concentration	VWR International AS [42]

4.1.2 Furnaces and sample preparation tools

An overview of furnaces and sample preparation tools is presented in Table 4.2.

Table 4.2: The furnaces and sample preparation tools used for synthesis and specimen preparation in this project.

Furnaces & tools	**Comments**	**Company**
Alumina (Al_2O_3) crucibles with lids		
Copper (Cu) rings	glued to TEM specimens for ion beam thinning 3.05 mm in diameter 2 mm × 1 mm and 2 mm × 1.5 mm slots	Agar Scientific [44]
Struers polishing cloth	Dur (6 µm diamond), Moll (3 & 1 µm diamond) and Nap (¼ µm diamond)	Struers [46]
Finder grids	H7 Cu grids	Agar Scientific [44]
Holey carbon films on Cu grids	400 Mesh Cu	Agar Scientific [44]
Horizontal sylinder furnace	surrounds an alumina tube concealing samples in an argon (Ar, purity = 99.999 %) atmosphere	
Ion beam thinner	Gatan precission ion polishing system (PIPS) Model 691	Gatan [47]
Muffle oven	Nabertherm	
Waterproof silicon carbide (SiC) paper FEPA	# 120, 220, 320, 500, 800, 1000, 1200, 2400 and 4000	Struers [46]
Teflon cup		
Ultrasonicator	Branson 3510	

4.2 Synthesis

Mg is very volatile and oxidizes easily. In order to compensate for the loss of Mg, excess Mg is added to and mixed with the reactants in all of the samples in this project. The nominal compositions of the synthesized materials, before excess Mg is added, are $Mg_2Si_{1-x}Sn_x$ with x = 0.00, 0.25, 0.50, 0.75 and 1.00. Table 4.3 shows an overview of which synthesis methods and temperatures were used on each composition. The reaction equations corresponding to all samples are given under their respective descriptions. In order to distinguish between nominal compositions of samples and characterized phases within the specimens, and to

distinguish between samples with the same nominal compositions but made from a different method, the sample name will be followed by the maximum temperature at which reactions occured.

Table 4.3: An overview showing the synthesis methods and temperatures (°C) used for the samples of different nominal compositions.

Sample	Solid state synthesis	Solidification of a homogeneous melt	Boron oxide flux synthesis
Mg_2Si	600-700*		
$Mg_2Si_{0.75}Sn_{0.25}$	700	1150	
$Mg_2Si_{0.50}Sn_{0.50}$			700
$Mg_2Si_{0.25}Sn_{0.75}$	750	1100, 1150	
Mg_2Sn		900	

*According to Schubert and Hüsing, solid state synthesis comprises all syntheses where at least one of the reactants is a solid [35].

4.2.1 Mg_2Si

Powders of Mg_2Si were made by mixing Mg and Si powders, with excess Mg varying from 0 to 5 mol %, pressing the mixtures into pellets, and heating the pellets to 600-700 °C for 5 – 12 hours in an Ar furnace. The reaction equation is presented in equation 4.1.

$$2Mg(l,g) + Si(s) \rightarrow Mg_2Si(s) \quad (4.1)$$

The samples will from now on be referred to as Mg_2Si-700.

4.2.2 Mg_2Sn

A sample of Mg_2Sn was prepared by mixing Mg powder and filed Sn with 50 mol % excess Mg. The mixture was placed in an alumina crucible and heated to 900 °C for 80 minutes in an Ar furnace. See equation 4.2. The solid was crushed into a powder before being characterized.

$$2Mg(l,g) + Sn(l) \rightarrow Mg_2Sn(l) \quad (4.2)$$

This sample will from now on be referred to as Mg_2Sn-900.

4.2.3 $Mg_2Si_{0.50}Sn_{0.50}$

4.2.3.1 Boron oxide flux method

Following the synthesis procedure of Gao et al. [19], stoichiometric amounts of filed Sn, Si powder and Mg powder, with 10 mol % extra Mg, were mixed and covered with B_2O_3 powder in an alumina crucible, and heated to 700 °C for 10 hours in an oven with air as atmosphere. Several samples were made in this way, and the powders were usually compacted in the crucibles. However, Mg-Si-Sn and Mg-Si-Sn-B_2O_3 mixtures were also pressed into pellets. The Mg-Si-Sn pellets were covered by B_2O_3. See equation 4.3.

$$4Mg(l,g) + Si(s) + Sn(l) \rightarrow 2Mg_2Si_{0.50}Sn_{0.50}(s) \quad (4.3)$$

In the rest of this text these samples will be referred to as $Mg_2Si_{0.50}Sn_{0.50}$-700.

4.2.4 $Mg_2Si_{0.75}Sn_{0.25}$

4.2.4.1 Solid state synthesis

Stoichiometric amounts of Mg_2Si-700 and Mg_2Sn-900 were crushed and mixed with 5 wt. % extra Mg powder, and pressed into a pellet of 13 mm in diameter. The pellet was placed in an alumina crucible and heated in an Ar furnace at 700 °C for 2 days. The product was crushed, mixed with 5 mass % extra Mg, pressed into a pellet, and heated again at 700 °C for 2 days. This was repeated one more time. See equation 4.4.

$$3Mg_2Si(s) + Mg_2Sn(s) \rightarrow 4Mg_2Si_{0.75}Sn_{0.25}(s) \quad (4.4)$$

These samples will from here on be referred to as $Mg_2Si_{0.75}Sn_{0.25}$-700.

4.2.4.2 Solidification of a homogeneous melt

One sample of nominal composition $Mg_2Si_{0.75}Sn_{0.25}$ was synthesized. Stoichiometric amounts of Mg_2Si-700 and Mg powder and filed Sn were mixed with 10 wt. % Mg in excess.

The mixture was pressed into a pellet, placed in an alumina crucible and heated in an Ar furnace at 1150 °C for three hours. The reaction equation is presented in equation 4.5.

$$3Mg_2Si(l) + 2Mg(l,g) + Sn(l) \rightarrow 4Mg_2Si_{0.75}Sn_{0.25}(l) \quad (4.5)$$

This sample will from now on be referred to as $Mg_2Si_{0.75}Sn_{0.25}$-1150.

4.2.5 $Mg_2Si_{0.25}Sn_{0.75}$

4.2.5.1 Solid state synthesis

Stoichiometric amounts of Mg_2Si-700 and Mg_2Sn-900 were crushed, mixed in an agate mortar with a pistil, and pressed into a pellet of 13 mm in diameter. The pellet was placed in an alumina crucible and heated in an Ar furnace to 750 °C and kept at that temperature for a day. After cooling down to room temperature, the product was crushed, pressed and heated again at 750° C for a day under Ar atmosphere. See equation 4.6.

$$Mg_2Si(s) + 3Mg_2Sn(s) \rightarrow 4Mg_2Si_{0.25}Sn_{0.75}(s) \quad (4.6)$$

These samples will be referred to as $Mg_2Si_{0.25}Sn_{0.75}$-750.

4.2.5.2 Solidification of a homogeneous melt

Stoichiometric amounts of Mg_2Si-700 and Mg_2Sn-900 were crushed and mixed with 5 wt. % added Mg in a mortar, and placed in an alumina crucible. The mixture was heated to 1100 °C, which is close to the melting point of Mg_2Si (1102 °C), in an Ar furnace, and kept at that temperature for an hour. See equation 4.7.

$$Mg_2Si(l) + 3Mg_2Sn(l) \rightarrow 4Mg_2Si_{0.25}Sn_{0.75}(l) \quad (4.7)$$

This product will be referred to as $Mg_2Si_{0.25}Sn_{0.75}$-1100. The same procedure was followed for two other samples, but elemental Mg powder and filed Sn were used instead of Mg_2Sn-900 powder as reactants. The two samples were kept at 1100 °C and 1150 °C for 2h and 4h, respectively. See equation 4.8.

$$Mg_2Si(l) + 6Mg(l,g) + 3Sn(l) \rightarrow 4Mg_2Si_{0.25}Sn_{0.75}(l) \quad (4.8)$$

The two products will from now on be called $Mg_2Si_{0.25}Sn_{0.75}$-1100 and $Mg_2Si_{0.25}Sn_{0.75}$-1150.

4.3 Characterization

Powder XRD was performed on all products, most of them with Si as a reference material for correcting displacement errors, and without Si to see if there was any Si phase in the samples. All products were viewed in the optical stereomicroscope. Optical reflection microscopy and SEM were only used on bulk homogeneous solids that were cooled from a homogeneous melt, namely $Mg_2Si_{0.75}Sn_{0.25}$-1150, $Mg_2Si_{0.25}Sn_{0.75}$-1100 and $Mg_2Si_{0.25}Sn_{0.75}$-1150. All specimens were studied thoroughly in the JEOL 2000FX TEM, while only a few were analysed in the JEOL 2010F TEM.

Table 4.4 summarizes the characterization techniques that were used on the different samples. OM stands for optical microscopy in the table. Further discussion of the characterization methods are given in the following sections.

Table 4.4: An overview of the characterization methods performed on the different samples.

Sample	XRD	OM (stereo)	OM (reflection)	SEM	TEM
Mg_2Si-700	x	x			x
$Mg_2Si_{0.75}Sn_{0.25}$-700	x	x			x
$Mg_2Si_{0.75}Sn_{0.25}$-1100	x	x	x	x	x
$Mg_2Si_{0.50}Sn_{0.50}$-700	x	x		x	x
$Mg_2Si_{0.25}Sn_{0.75}$-750	x	x			x
$Mg_2Si_{0.25}Sn_{0.75}$-1100	x	x	x	x	x
$Mg_2Si_{0.25}Sn_{0.75}$-1150	x	x	x	x	x
Mg_2Sn-900	x	x			x

4.3.1 Optical microscopy

In the present project a Motic SMZ168 optical stereomicroscope was used to evaluate the powders of all samples. The colour of the powders were identified, and aided the removal of glassy (or other unwanted) material, and in some cases enabling separation of different coloured powders.

A Reichert-Jung MeF3 reflection microscope was used to study polished cross section samples to get an overview of the microstructure and phases present in the bulk samples.

A Jenoptic ProgRes C5 camera was equipped to both microscopes. The multifocus function [49] (see chapter 3.2.2) in ProgRes Capture was used for obtaining sharp pictures of areas with high topography, because of the poor depth of field in optical microscopes.

4.3.2 Scanning electron microscopy

Two SEMs were used in the project. The first is a Quanta 200 FEI FEG SEM. It can be used for both high and low vacuum SEM. It is equipped with an X-ray detector and an EDS system (EDAX Genesis). ZAF corrections were used in quantifying the obtained spectra. Carbon is the lightest detectable element. As the name of the SEM implies, the electron gun is a field emission gun (FEG), in which electron tunnelling occurs.

The other SEM is a tabletop microscope, TM3000, combined with a Quantax EDS system. The lightest detectable element is carbon, and quantification of EDS spectra was corrected by the ZAF method. EDS analyses are performed relatively quickly. Elemental mapping is completed within minutes instead of hours.

Composites of $Mg_2Si_{0.50}Sn_{0.50}$-700 and Gatan G1 epoxy, and the bulk samples $Mg_2Si_{0.75}Sn_{0.25}$-1150, $Mg_2Si_{0.25}Sn_{0.75}$-1100 and $Mg_2Si_{0.25}Sn_{0.75}$-1150 that were studied in the optical reflection microscope were studied in the Quanta 200 FEG SEM. Different phases were identified by combining EDS (both spot analyses and elemental mapping) and SE- and BSE-imaging. The ion thinned TEM specimens (see section 4.3.4.3) were analysed in both SEMs first, in order to locate areas of interest near the holes, so that they would be easily found in the TEM afterwards.

4.3.3 X-ray diffraction

A Bruker D8 Discover X-ray diffractometer with a Lynxeye detector and a Bruker D5000 X-ray diffractometer with a Braun position sensitive detector were used in the present project.

They have Bragg-Brentano θ-2θ geometries, and their incidetnt X-rays are CuKα_1-rays selected by a germanium (111) monochromator. Incident angles were chosen from 10 to 90 degrees. In addition to displacement errors, X-offset also had to be corrected in scan files obtained with the Bruker D5000 diffractometer.

All samples of $Mg_2Si_{1-x}Sn_x$ were crushed into fine powders and characterized by powder XRD. Ethanol was used to spread the powders on all but one XRD sample holder, where toluene was used instead. The scan files were corrected with respect to the added Si, and analysed in Eva Version 13.0.0.3 [50]. Peaks corresponding to phases of interest were refined with UnitCell Version 0.95 [51] in order to determine lattice constants.

4.3.4 Transmission electron microscopy

4.3.4.1 The instruments

Two analytical TEMs operated at 200 kV were used in this project; JEOL 2000FX and JEOL 2010F. A Gatan double tilt sample holder was used in the JEOL 2000FX, allowing high tilt angles (+/- 45° in the *x*-direction, +/- 36° in the *y*-direction). The 2000FX is equipped with a Si(Li) X-ray detector and an EDS system (Noran system six). The lightest detectable element is sodium. The correction method Cliff-Lorimer without absorption was used in the quantification of the EDS spectra. The electron gun has a lanthanum hexaboride (LaB_6) crystal as filament. Such thermionic emitters provide a high brightness and total beam current and have a long life time (500-1000 hours), but are fragile, unstable and require a high vacuum (~10^{-7} torr) [39].

The JEOL2010F is equipped with a thin window X-ray detector and an EDS system (Noran Vista). Boron is the lightest detectable element. The Cliff-Lorimer correction method without absorption was used. The electron gun is a field emission gun (FEG). The main advantages with FEGs are a very high brightness and a long lifetime (> 1000 hours), but they have unstable currents and require a very high vacuum (~10^{-10} Torr) [39].

4.3.4.2 Calibration

The camera length, *L*, of the JEOL 2000FX was calibrated with a Si standard and with powders of Mg_2Si and Mg_2Sn, where the lattice parameters were found by XRD. Diffraction patterns were measured in different directions on the films, and a sinusoidal curve of camera length as a function of direction on the film was made (see Fig. 4.1). Calibration was carried out on samples in eucentric height and with OBJ focus = 7.03.

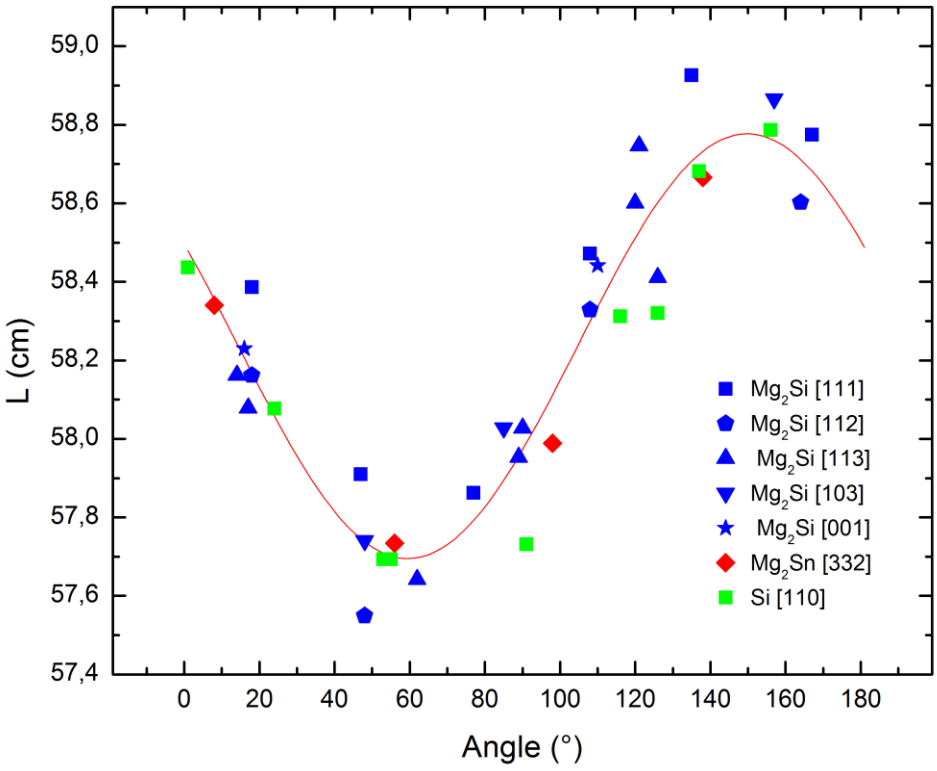

Figure 4.1: Camera length *L* as a function of measured directions on films. The angles are measured in the counterclockwise direction relative to a horizontal vector pointing toward the right-hand side from the central reflection.

It is not really the camera length *L* that has been calibrated in the JEOL 2000FX TEM. It is actually the camera constant $K = L\lambda$ that has been calibrated, but by assuming that the wavelengths of the incident electrons are equal to their nominal value, $\lambda = 0.00251$ nm, one can refer to the calibration procedure as calibrating the camera length, *L*. It was concluded that the directional dependence of *L* is mostly due to asymmetry in the objective lens.

4.3.4.3 Specimen preparation

Around 20 powder TEM samples were prepared by the following method: Each sample was crushed and stirred in ethanol in an agate mortar with a pistil. One or two drops of the ethanol with immersed particles were placed on a holey carbon film on a square Cu grid or on a finder grid. A drop of a suspension of Si particles in ethanol was added to some of the specimens as well, as a reference material for diffraction patterns.

Around ten composite specimens were made as well. Some $Mg_2Si_{0.50}Sn_{0.50}$-700 powder was mixed in Gatan G1 epoxy in a Teflon cup. Then the composite was heated until the epoxy had hardened, and subsequently removed from the cup. After that, the mixture was ground, glued to Cu-rings, and cut into discs around the Cu-rings. Finally, the discs were ion milled until there were relatively large holes (~0.3 mm in diameter) in them, with many crystals in thin edges around the hole. The ion milling was carried out in the precision ion polishing system (PIPS), in which the specimen is rotating while being irradiated with Ar ions. The incident angles of the ion sources above and below the rotating specimen were set to 8 ° and 7.5 °, respectively. Ion beam thinning was performed for 2 – 8 hours, depending on the specimen thickness. The voltage of the Ar beams was set to 5 kV until a large hole (~ 0.3 mm in diameter) appeared in the samples, and then it was reduced to 3 kV for half an hour before they were turned off.

A part of the composite of a powder product in Gatan G1 epoxy was sandwiched and hardened between two sets of two Si wafers. The sample was ground on opposite sides of the wafers, then glued to a Cu-ring, and finally ion milled in the PIPS.

The bulk samples, namely $Mg_2Si_{0.75}Sn_{0.25}$-1150, $Mg_2Si_{0.25}Sn_{0.75}$-1150 and $Mg_2Si_{0.25}Sn_{0.75}$-1100, were cut into thin pieces, ground, polished, glued to Cu rings and ion milled in the PIPS.

4.3.4.4 Characterization techniques with transmission electron microscopy

All specimens were examined in the JEOL 2000FX. One of the ion milled composite specimens of $Mg_2Si_{0.50}Sn_{0.50}$-700 was also studied in the JEOL 2010F. The techniques that were used include bright field (BF) and dark field (DF) imaging, high resolution transmission

electron microscopy (HRTEM; only in the JEOL 2010F), selected area diffraction (SAD), convergent beam electron diffraction (CBED; only in the JEOL 2000FX) and EDS. CBED mode was only used while tilting in the 2000FX, but if the particles moved a lot during tilting, tilting was performed in SAD mode instead. Diffraction patterns and EDS spectra were recorded from the same areas. Some high resolution images were Fourier transformed in Gatan DigitalMicrograph [52]. Tilt series were performed on several particles. The angles between the zone axes were calculated from the following equation:

$$\cos\theta_{12} = \cos(\beta_2 - \beta_1)\ \cos\alpha_1\ \cos\alpha_2 + \sin\alpha_1 \sin\alpha_2 \qquad (4.9)$$

where θ_{12} is the angle the TEM specimen has been tilted, α_1 and β_1 are the *x*- and *y*-tilt angles before tilting, and α_2 and β_2 are the *x*- and *y*-tilt angles after tilting [53]. The angles between certain zone axes in a face centred cubic lattice are listed in Table 4.5.

Table 4.5: Calculated angles between certain zone axes in cubic lattices.

Zone axes	Overall angles
[001] and [114]	19.5°
[114] and [113]	5.77°
[113] and [112]	10.0°
[112] and [111]	19.5°
[111] and [332]	10.0°
[332] and [110]	25.2°
[110] and [001]	45.0°
[001] and [103]	18.4°
[103] and [101]	26.6°

5. Results

All samples made by solid state synthesis were powders. All samples synthesized by heating the mixtures above the melting temperature of all reactants (see Table 4.3, Section 4.2) ended up as bulk solids (see Fig. 5.1), except for the $Mg_2Si_{0.25}Sn_{0.75}$-1100 sample made by mixing Mg_2Si and Mg_2Sn, which ended up as a powder instead. Since the latter sample did not melt, it will no longer be considered in this text. Specimens with nominal composition $Mg_2Si_{0.50}Sn_{0.50}$ became powders when Mg-Si-Sn mixtures were neither mixed with B_2O_3 nor pressed into pellets before heating. Otherwise the products were solid and sometimes glassy materials. Toluene was used instead of ethanol for spreading powder from one of these samples onto an XRD sample holder. This is because glassy B_2O_3 surfaces dissolved in ethanol. Powders and solid products had bluish grey colours. One sample of $Mg_2Si_{0.50}Sn_{0.50}$ consisted of blue and brown particles (see Fig. 5.2). According to XRD, the brown particles were mostly Sn, but also contained cassiterite (SnO_2) and periclase (MgO), so they were not characterized further in this project.

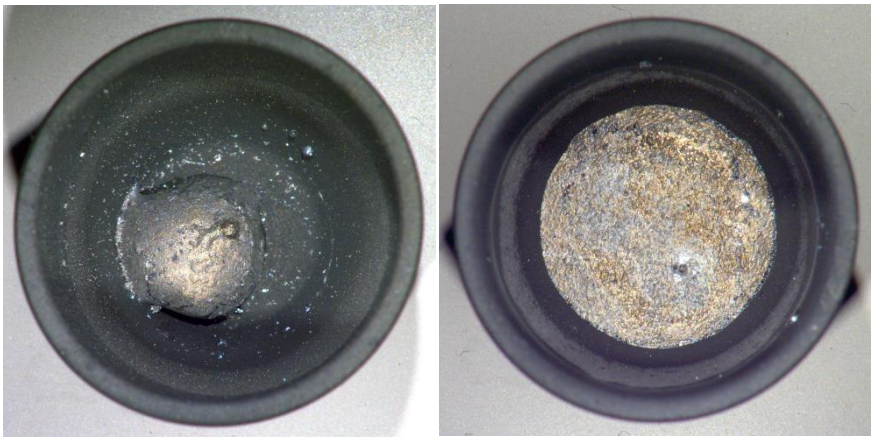

Figure 5.1: Stereomicroscope images of the products of $Mg_2Si_{0.75}Sn_{0.25}$-1150 (left) and $Mg_2Si_{0.25}Sn_{0.75}$-1150 (right). The top of the crucibles are 24 mm in diameter.

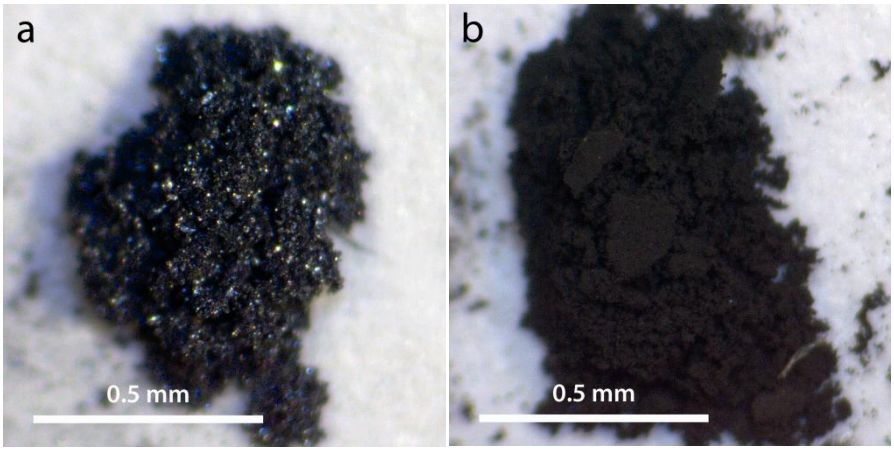

Figure 5.2: An optical stereomicroscope image showing blue and brown crystals from a sample with nominal composition $Mg_2Si_{0.50}Sn_{0.50}$. The blue particles (a) are $Mg_2Si_{1-x}Sn_x$ and the brown ones (b) are mostly Sn.

In the rest of this text, phases of $Mg_2Si_{1-x}Sn_x$ on the Si-rich side of the immiscibility gap (see binary phase diagram in Fig. 1.1) will be referred to as "Mg_2Si". Similarly, "Mg_2Sn" refers to $Mg_2Si_{1-x}Sn_x$ on the Sn-rich side of the immiscibility gap. Elemental phases are written in brackets, such as (Mg), (Si) and (Sn).

5.1 Microstructure observations and compositional analysis

The three bulk samples $Mg_2Si_{0.25}Sn_{0.75}$-1100, $Mg_2Si_{0.25}Sn_{0.75}$-1150 and $Mg_2Si_{0.75}Sn_{0.25}$-1150 were investigated by optical reflection microscopy and analytical SEM. They consist of different phases, as shown in the overview images in Figs. 5.3 and 5.4. Fig. 5.3 is an image of a large area of $Mg_2Si_{0.75}Sn_{0.25}$-1150 obtained with the optical reflection microscope. Fig. 5.4 is a backscattered electron image of $Mg_2Si_{0.25}Sn_{0.75}$-1150 obtained in the Quanta 200 FEI FEG SEM, giving an overview of how the bulk specimens appear in the SEMs at relatively low magnification. Based on colour and contrast in the images, there are at least four different phases, as indicated with numbers in both figures. One phase ("phase 1") consists of large dendritic crystals (~ 200 µm in diameter), surrounded by another ("phase 2"), which is in turn surrounded by a eutectic mixture ("phase 3"). There are crystals (~20 µm in diameter) of a fourth phase dispersed throughout the specimens ("phase 4"), but most of the volume consists of the three other phases. (These names will only be used for optical microscope images and the overview SEM image.) The samples are not homogeneous and have not

reached equilibrium. However, they have a homogeneous distributions of the phases. Hence, they are homogeneous on a large scale.

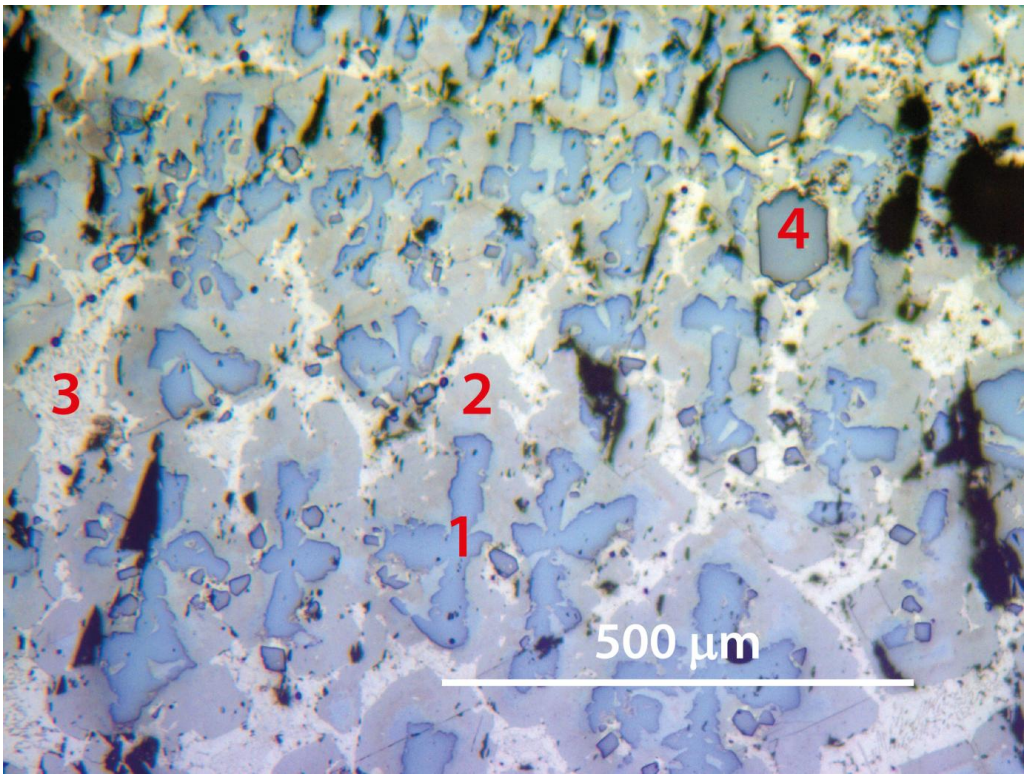

Figure 5.3: An overview image of sample $Mg_2Si_{0.75}Sn_{0.25}$-1150 obtained in the reflection optical microscope, showing the presence of dendritic crystals (1), surrounded by another phase (2), surrounded by yet another phase (3), and some other crystals (4).

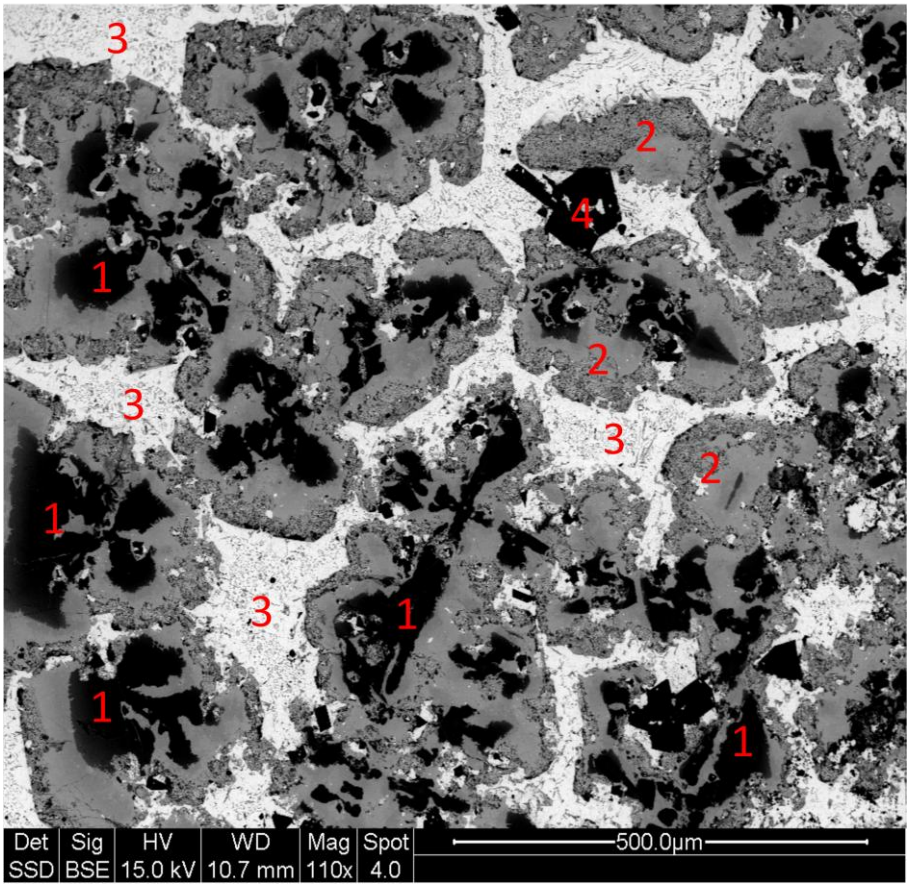

Figure 5.4: An overview of $Mg_2Si_{0.25}Sn_{0.75}$-1150. Dendritic "Mg_2Si" crystals (1) are surrounded by "Mg_2Sn" crystals (2), which are in turn surrounded by a eutectic mixture of (Sn) and Mg_2Si (3). Si crystals (4) are present throughout the specimen. The phases have been numbered in the same way as those in the optical microscope image in Fig. 5.3.

5.1.1 $Mg_2Si_{0.25}Sn_{0.75}$-1100

Fig. 5.5 shows an image of sample $Mg_2Si_{0.25}Sn_{0.75}$-1100. There are at least four different phases. The contrast in "phase 2" varies between the areas close to "phase 1" and those close to the eutectic mixture.

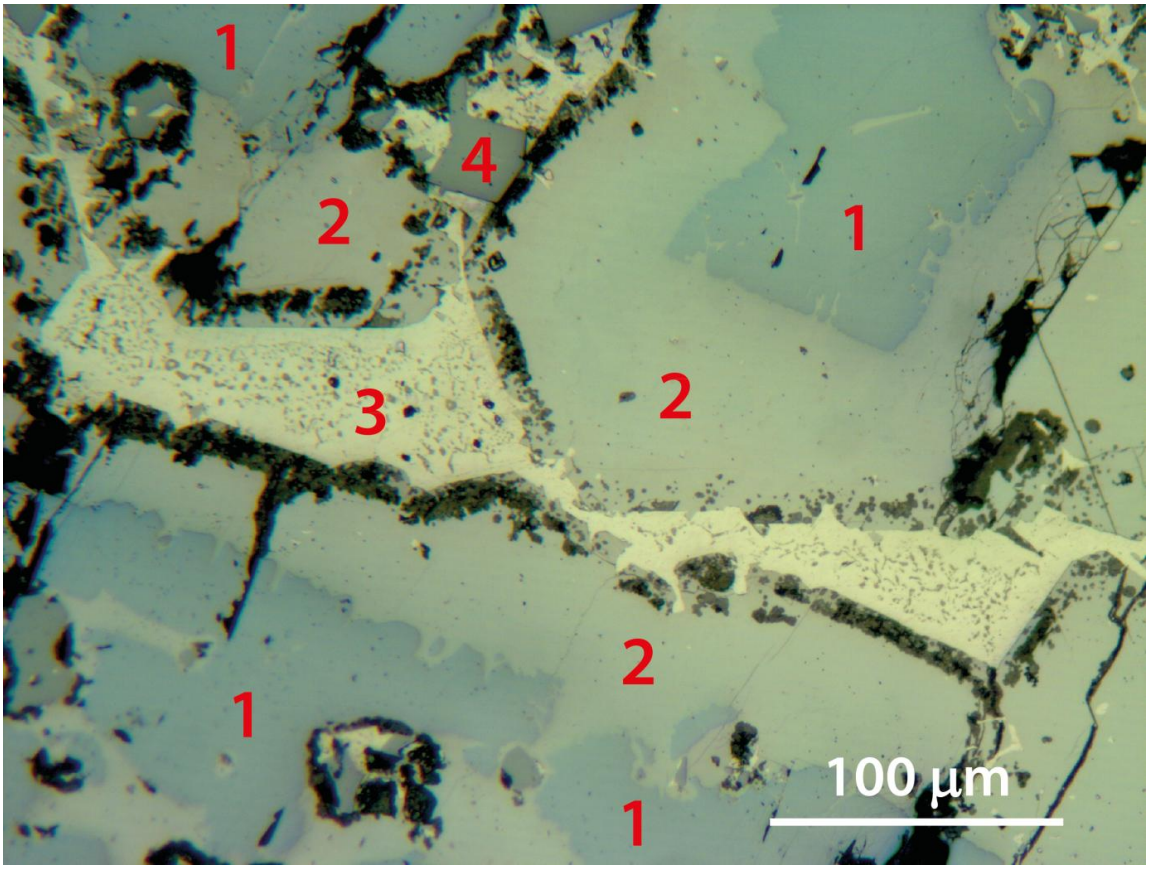

Figure 5.5: An image of sample $Mg_2Si_{0.25}Sn_{0.75}$-1100. The phases include at least four different phases: dendritic crystals (1), another phase surrounding them (2), a eutectic mixture (3) and other small crystals (4). Parts of "phase 2" close to "phase 3" have an oxide layer.

Fig. 5.6 shows a BSE image with corresponding elemental maps of an area in $Mg_2Si_{0.25}Sn_{0.75}$-1100, obtained in the SEM. The sample contains Mg, O, Si and Sn.

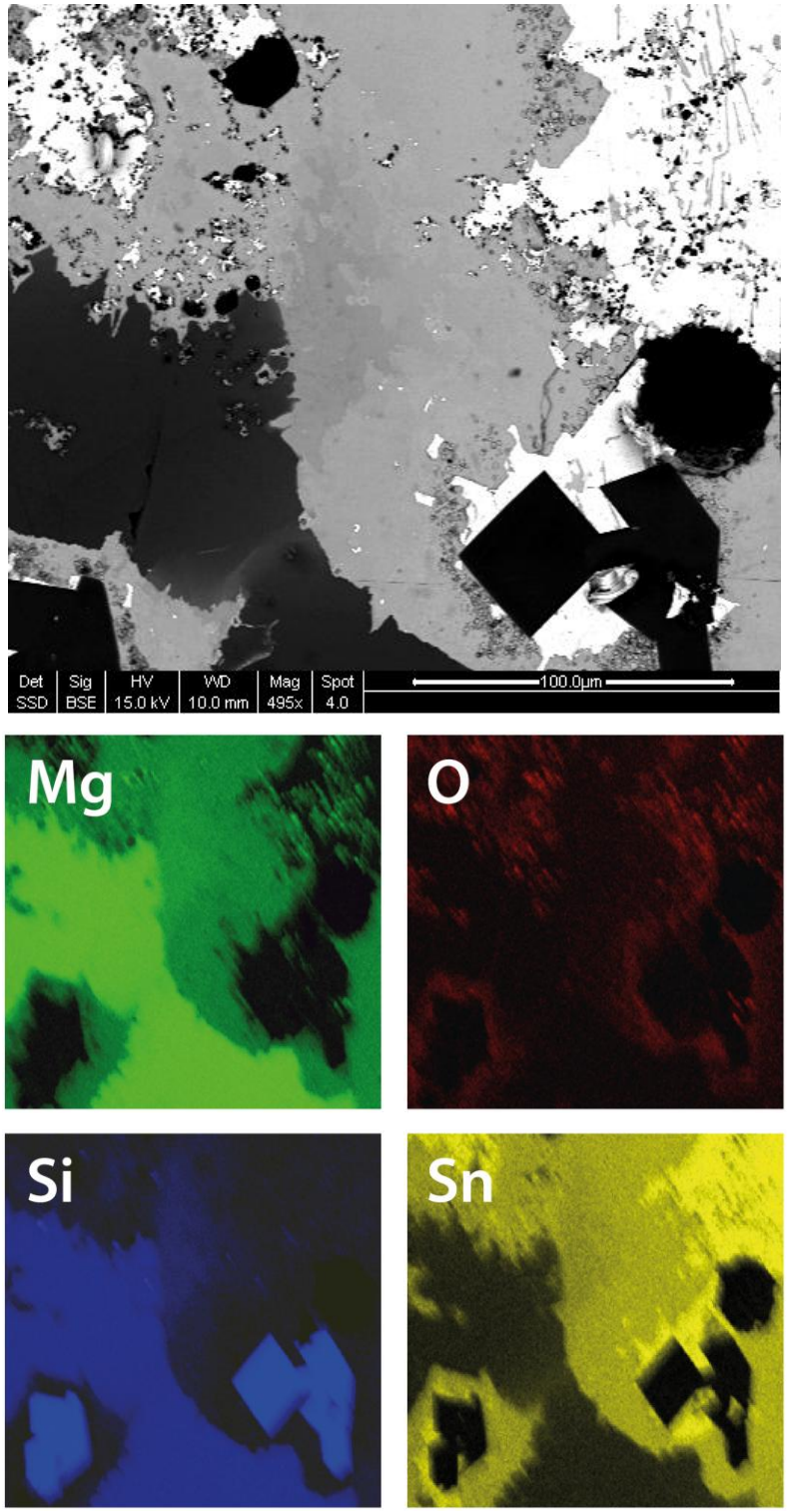

Figure 5.6: Elemental maps of an area of sample $Mg_2Si_{0.25}Sn_{0.75}$-1100, showing the presence of Mg (green), O (red), Si (blue) and Sn (yellow). The uppermost image is a BSE image.

Fig. 5.7 shows a BSE image of the specimen with numbers indicating areas of different compositions. According to EDS spot analyses, there are areas of $Mg_2Si_{1-x}Sn_x$ with compositions x = 0.10, 0.22, 0.69, 0.82 and 0.94. Points 1 and 2 are from "phase 1" (see Fig. 5.5), and points 3, 4 and 5 correspond to "phase 2". An oxide layer had formed on the surface during specimen preparation, because water was used as a coolant during grinding, and water-based lubricant (Diamond polishing suspension, green [46]) was applied during polishing. Si crystals were found all over the sample. The brightest areas of the BSE image (7) are a eutectic mixture consisting of small Mg_2Si particles in a (Sn) matrix.

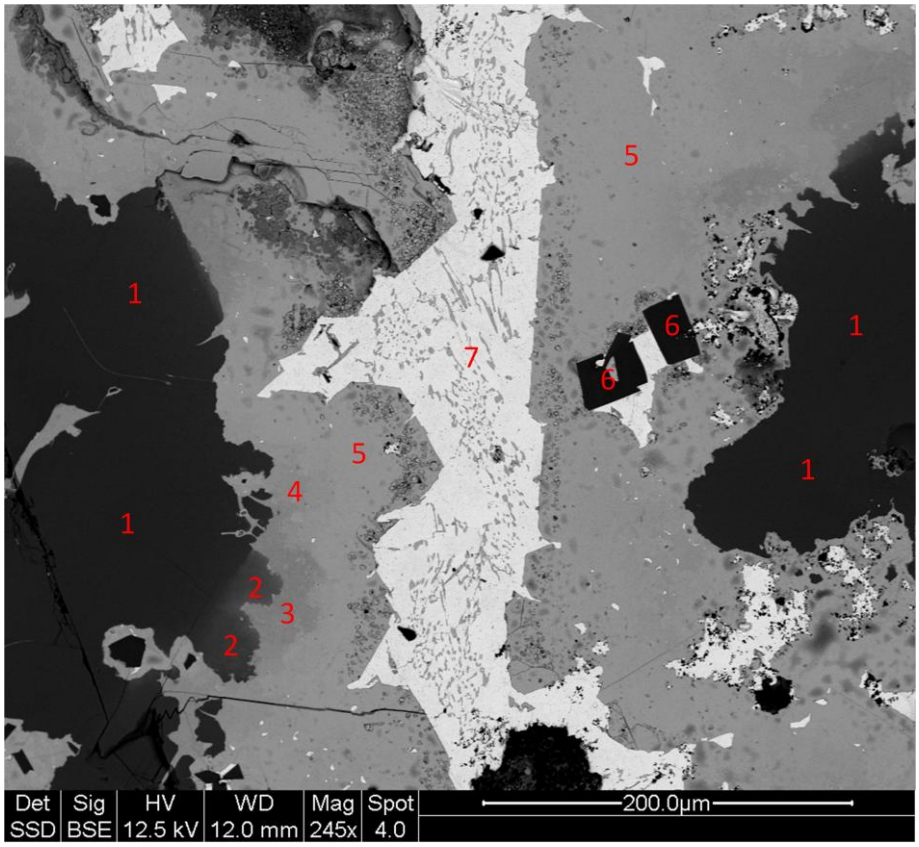

Figure 5.7: A BSE image of specimen $Mg_2Si_{0.25}Sn_{0.75}$-1100. Areas with different compositions are numbered: 1) $Mg_2Si_{0.90}Sn_{0.10}$, 2) $Mg_2Si_{0.78}Sn_{0.22}$, 3) $Mg_2Si_{0.31}Sn_{0.69}$, 4) $Mg_2Si_{0.18}Sn_{0.82}$, 5) $Mg_2Si_{0.06}Sn_{0.94}$ and 6) Si. 7) marks the eutectic mixture of Mg_2Si particles in a (Sn) matrix.

5.1.2 $Mg_2Si_{0.25}Sn_{0.75}$-1150

An image of an area of $Mg_2Si_{0.25}Sn_{0.75}$-1150 obtained in the optical microscope is presented in Fig. 5.8. At least four different phases are observed. The contrast in "phase 2" varies

between “phase 1” and “phase 3”. Parts of “phase 2” close to “phase 3” are oxidized (see the yellow “2” on Fig. 5.8), because grinding of the surface of the specimen was done in water.

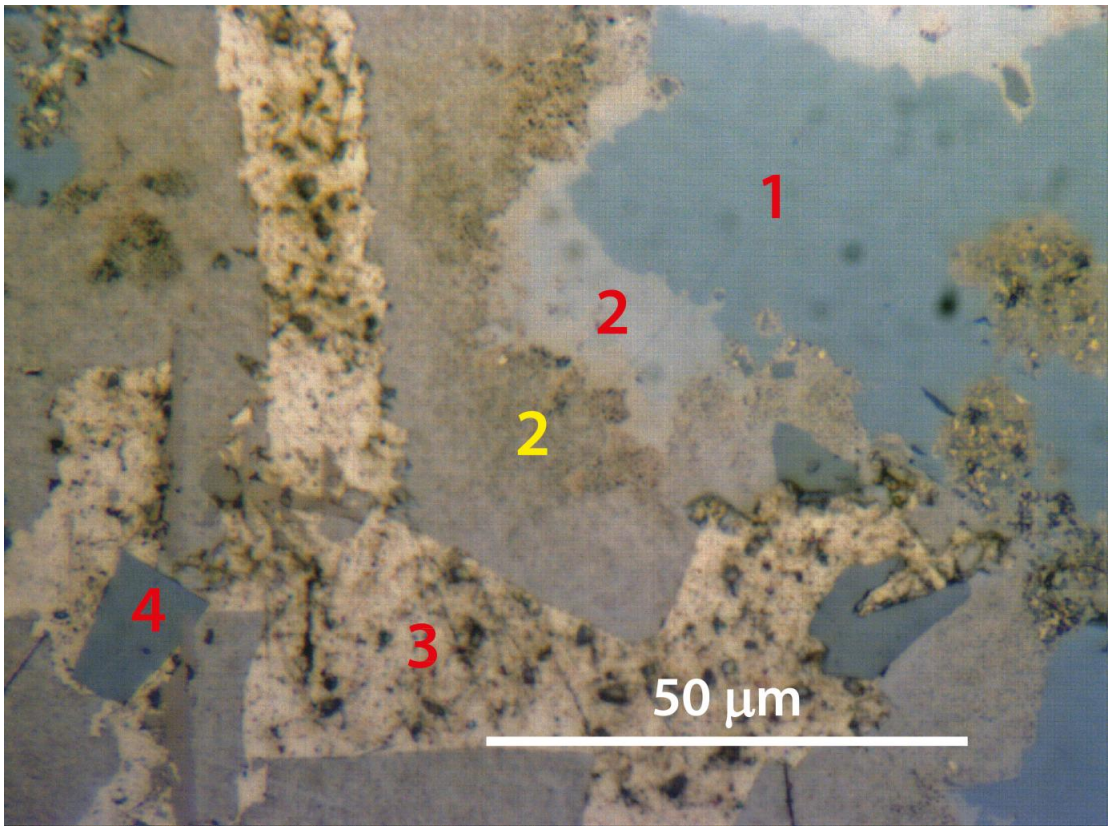

Figure 5.8: An image of sample $Mg_2Si_{0.25}Sn_{0.75}$-1150, obtained in the optical microscope. The phases are dendritic crystals (1), another phase around the first (2), a eutectic mixture (3), and other crystals (4). Parts of “phase 2” have been oxidized (yellow 2).

A BSE image with corresponding elemental maps of an area of $Mg_2Si_{0.25}Sn_{0.75}$-1150 are presented in Fig. 5.9. The sample contains Mg, Si and Sn. Oxygen was excluded in the analysis.

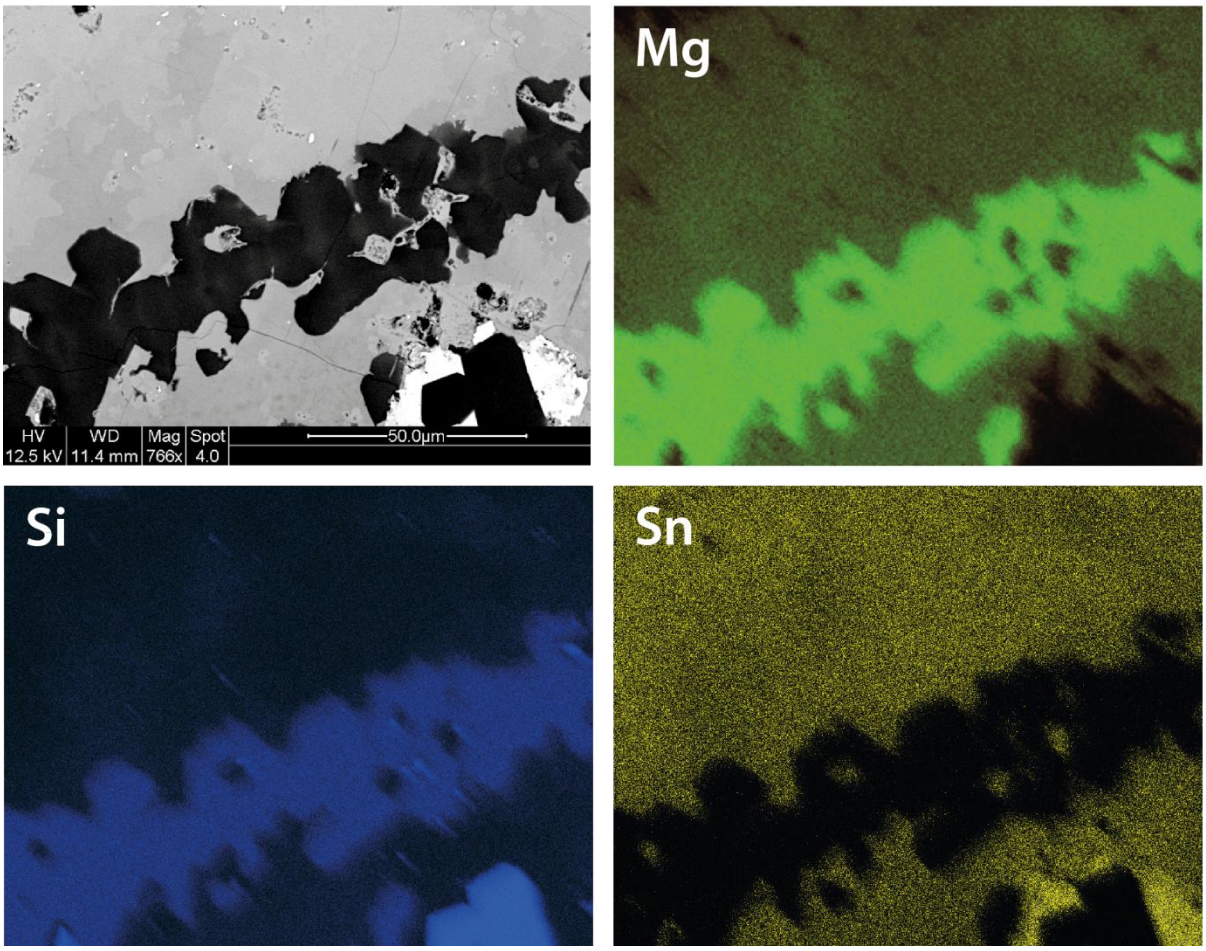

Figure 5.9: Elemental maps of sample $Mg_2Si_{0.25}Sn_{0.75}$-1150, showing the presence of Mg (green), Si (blue) and Sn (yellow).

A BSE image of $Mg_2Si_{0.25}Sn_{0.75}$-1150 is given in Fig. 5.10. The specimen had areas of $Mg_2Si_{1-x}Sn_x$ with x = 0.21, 0.31, 0.67, 0.72 and 0.77. Points 1 and 2 correspond to "phase 1" (see Fig. 5.8), and points 3, 4 and 5 are from "phase 2". Si crystals were found in many different areas, and MgO particles were found in the eutectic mixture of (Sn) and Mg_2Si. Two phases of $Mg_2Si_{1-x}Sn_x$ with slightly different contrast in the BSE image have the same overall composition of x = 0.77. The difference in contrast is caused by channelling effects. The penetration depth of electrons within a phase in a sample depends on the orientation of the crystals. Hence, electrons travel deeper into crystals of certain orientations than into others of the same phase, and so the corresponding areas appear darker in BSE images.

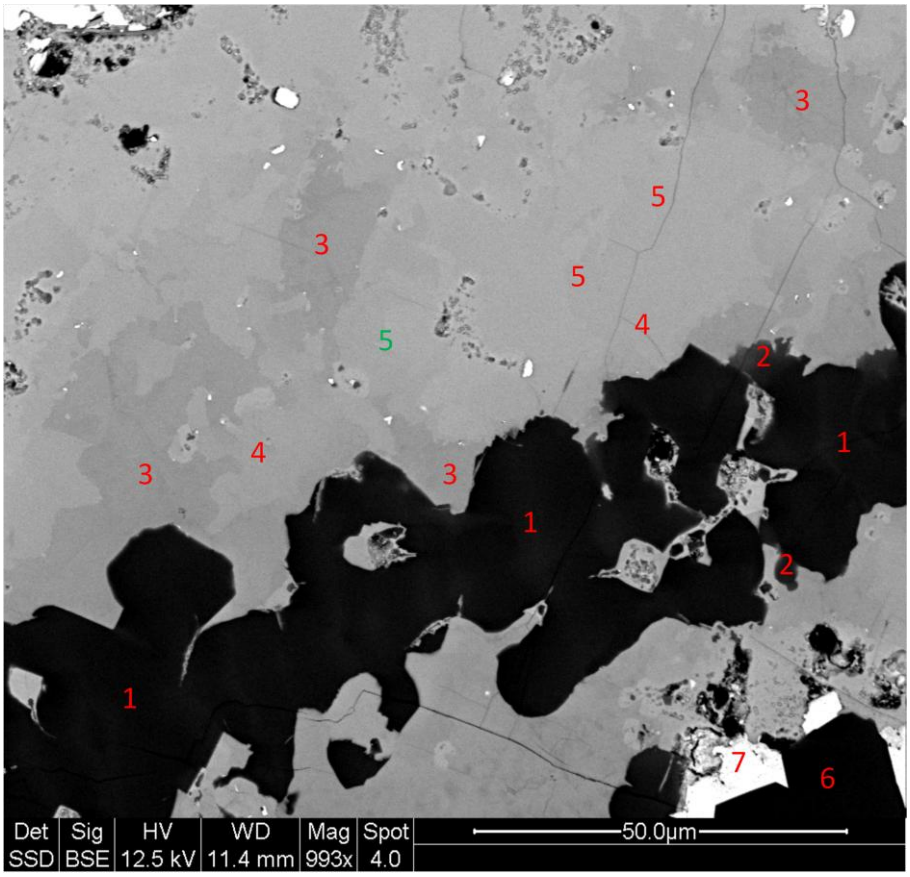

Figure 5.10: A BSE image of specimen $Mg_2Si_{0.25}Sn_{0.75}$-1150. Areas with different compositions are numbered: 1) $Mg_2Si_{0.79}Sn_{0.21}$, 2) $Mg_2Si_{0.69}Sn_{0.31}$, 3) $Mg_2Si_{0.33}Sn_{0.67}$, 4) $Mg_2Si_{0.28}Sn_{0.72}$, 5) $Mg_2Si_{0.23}Sn_{0.77}$, 6) Si crystals and 7) a eutectic mixture of Sn and Mg_2Si. The phase indicated with a green "5" has the same brightness as phase 4. The brightness of phase 5 varies because of the channeling effect.

5.1.3 $Mg_2Si_{0.75}Sn_{0.25}$-1150

Fig. 5.11 shows an optical microscope image of sample $Mg_2Si_{0.75}Sn_{0.25}$. As in the other two samples, it contains at least four different phases, one of which varies in contrast between two others phases (1 and 3), and is partly covered by an oxide layer (2). The oxide layer is due to the reactivity of the phase with water during grinding.

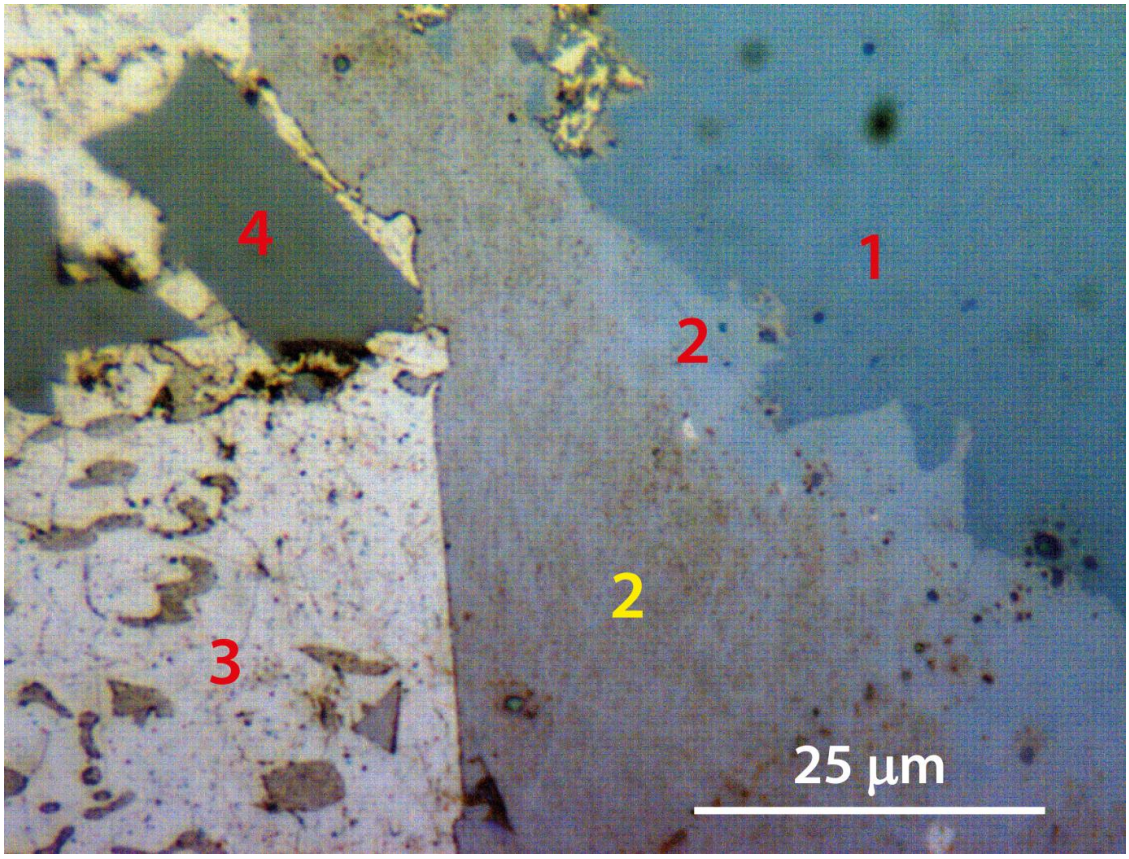

Figure 5.11: A BF image of sample $Mg_2Si_{0.75}Sn_{0.25}$-1150. The indicated phases are "Mg_2Si" (1), "Mg_2Sn" (2), a eutectic mixture of (Sn) and Mg_2Si (3) and Si crystals (4). "Mg_2Sn" surfaces have been oxidized over time.

A BSE image and corresponding elemental maps obtained in the SEM are presented in Fig. 5.12. Oxygen was excluded in the analyses. The elemental maps show the presence of Mg, Si and Sn.

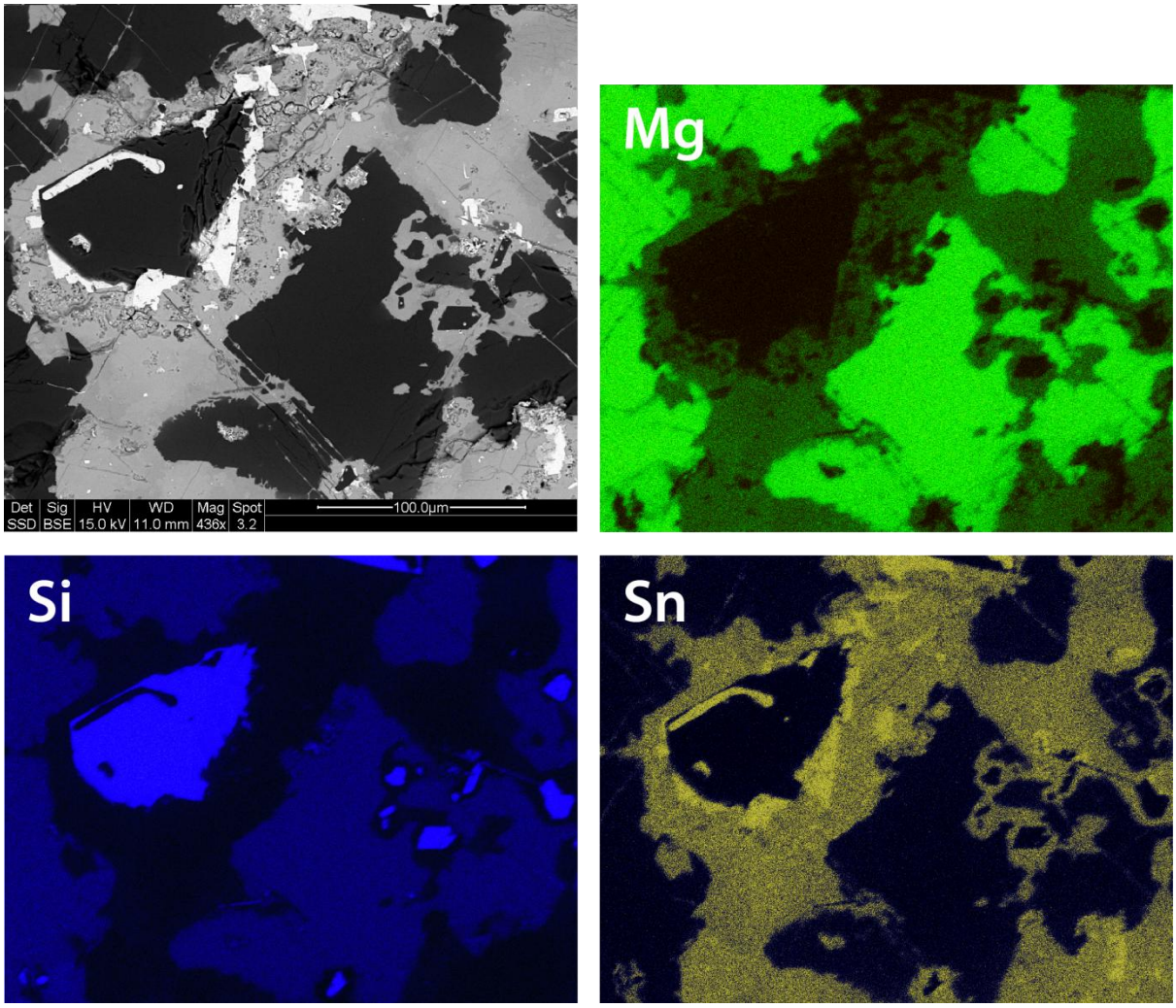

Figure 5.12: Elemental maps of sample $Mg_2Si_{0.75}Sn_{0.25}$-1150, showing the presence of Mg (green), Si (blue) and Sn (yellow).

Figure 5.13 shows a BSE image of $Mg_2Si_{0.75}Sn_{0.25}$-1150. The $Mg_2Si_{1-x}Sn_x$ phases had compositions corresponding to x = 0.08, 0.15, 0.55 and 0.65. Points 1 and 2 correspond to "phase 1" (see Fig. 5.11), and points 3 and 4 are related to "phase 2". Si crystals were dispersed in the different phases. The eutectic mixture consisted of Sn and Mg_2Si.

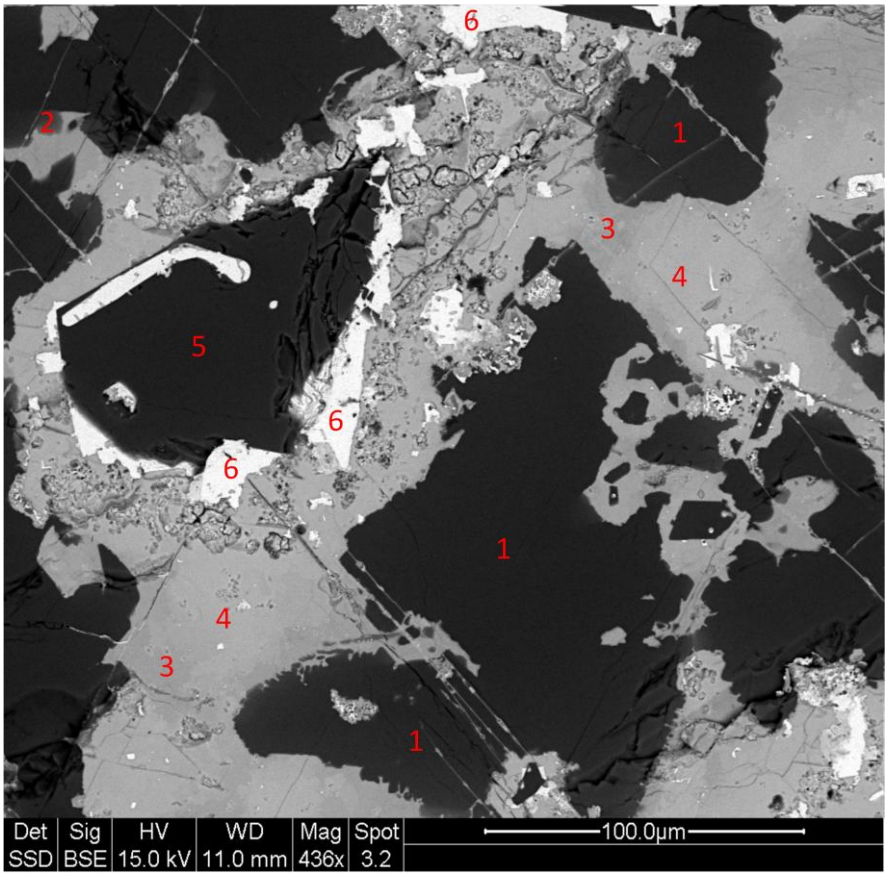

Figure 5.13: A BSE image of specimen $Mg_2Si_{0.75}Sn_{0.25}$-1150. Areas with different compositions are numbered: 1) $Mg_2Si_{0.92}Sn_{0.08}$, 2) $Mg_2Si_{0.85}Sn_{0.15}$, 3) $Mg_2Si_{0.45}Sn_{0.55}$, 4) $Mg_2Si_{0.35}Sn_{0.65}$, 5) Si crystals and 6) a eutectic mixture of Sn and Mg_2Si.

5.1.3 Summary of microstructure and compositions in the bulk specimens

The bulk materials, namely $Mg_2Si_{0.25}Sn_{0.75}$-1100, $Mg_2Si_{0.25}Sn_{0.75}$-1150 and $Mg_2Si_{0.75}Sn_{0.25}$-1150, contained at least four different phases. One phase consisted of large dendritic crystals, approximately 200 µm in diameter, of $Mg_2Si_{1-x}Sn_x$ rich in Si ("Mg_2Si"). They were surrounded by a Sn-rich $Mg_2Si_{1-x}Sn_x$ phase ("Mg_2Sn"), which were in turn surrounded by a eutectic mixture of (Sn) and Mg_2Si. Both "Mg_2Si" and "Mg_2Sn", especially the latter, varied in composition. "Mg_2Si" was richest in Si far away from "Mg_2Sn", while "Mg_2Sn" was richer in Si close to "Mg_2Si" and richer in Sn near the eutectic mixture. It was evident from the optical microscope images of $Mg_2Si_{0.25}Sn_{0.75}$-1150 and $Mg_2Si_{0.75}Sn_{0.25}$-1150 that "Mg_2Sn" had oxidic layers close to the eutectic mixture, but EDS analyses in the SEM also showed the presence of oxygen in the elemental maps.

Si crystals ("phase 4"), which were around 20 µm in diameter, were found in different places, but most of the volume in the specimens consisted of the other three phases. The relative amounts of the different phases depended on the nominal compositions of the samples. Most of $Mg_2Si_{0.75}Sn_{0.25}$-1150 consisted of "Mg_2Si" and "Mg_2Sn". In $Mg_2Si_{0.25}Sn_{0.75}$-1100 and $Mg_2Si_{0.25}Sn_{0.75}$-1150, the most predominant phases were "Mg_2Sn" and eutectic mixtures of (Sn) and Mg_2Si. Each bulk sample had a similar homogeneous distribution of the phases, but single phase materials were not obtained. Therefore, they were only homogeneous on a large scale.

Table 5.1 summarizes the compositions of the $Mg_2Si_{1-x}Sn_x$ phases obtained by EDS spot analysis. The values for *x* were determined by dividing the number of Sn atoms by the sum of Si and Sn atoms. The quantifications of the EDS spectra usually provided lower values of Mg (typically a few %) than the stoichiometric values for Mg_2(Si, Sn). As *x* increased in $Mg_2Si_{1-x}Sn_x$, the amount of Mg seemed to decrease in some of the samples, both in TEM and SEM.

Table 5.1: Compositions of the $Mg_2Si_{1-x}Sn_x$ phases in the bulk samples, obtained by EDS spot analysis in the Quanta 200 FEI SEM.

Sample	Composition (x)
$Mg_2Si_{0.25}Sn_{0.75}$-1100	0.10 0.22 0.69 0.82 0.94
$Mg_2Si_{0.25}Sn_{0.75}$-1150	0.21 0.31 0.67 0.72 0.77
$Mg_2Si_{0.75}Sn_{0.25}$-1150	0.08 0.15 0.55 0.65

After lying unprotected in a drawer for five months, samples $Mg_2Si_{0.25}Sn_{0.75}$-1100, $Mg_2Si_{0.25}Sn_{0.75}$-1150 and $Mg_2Si_{0.75}Sn_{0.25}$-1100 had Sn fibres sticking out from their surfaces (see Fig. A.2 in the appendix), and the "Mg_2Sn" phases had oxidized (as seen in the images in Figs. 5.8 and 5.11).

5.2 Powder X-ray diffraction

The refined lattice parameters of $Mg_2Si_{1-x}Sn_x$ from strong peaks in the following X-ray diffractograms are presented in Table 5.2. The values are given with four digits. Diffractograms of powders from the bulk specimens ($Mg_2Si_{0.25}Sn_{0.75}$-1100, $Mg_2Si_{0.25}Sn_{0.75}$-1150 and $Mg_2Si_{0.75}Sn_{0.25}$-1150) have three strong peaks each, while they consist of $Mg_2Si_{1-x}Sn_x$ phases with four or five different compositions according to EDS analyses in the SEM (see Table 5.1 in section 5.2.3).

Table 5.2: Lattice parameters refined from the strongest $Mg_2Si_{1-x}Sn_x$ peaks from the presented X-ray diffractograms.

Sample	**Lattice parameters [Å]**
Mg_2Si-700	6.352
$Mg_2Si_{0.75}Sn_{0.25}$-700	6.398 6.714
$Mg_2Si_{0.75}Sn_{0.25}$-1150	6.372 6.668 6.754
$Mg_2Si_{0.50}Sn_{0.50}$-700	6.355 6.462 6.659
$Mg_2Si_{0.25}Sn_{0.75}$-750	6.645 6.668 6.728
$Mg_2Si_{0.25}Sn_{0.75}$-1100	6.382 6.649 6.760
$Mg_2Si_{0.25}Sn_{0.75}$-1150	6.393 6.664 6.758
Mg_2Sn-900	6.764

Figure 5.14 shows a part of a powder X-ray diffractogram from an Mg_2Si-700 sample, which was synthesized by solid state reactions, and that of sample Mg_2Sn-900, which was made by solidifying a melt. The peaks in the diffractogram of Mg_2Si-700 correspond to phases of Mg_2Si with lattice parameter a = 6.352 Å, (Mg), (Si), (Sn) and periclase MgO. The diffractogram of Mg_2Sn-900 has peaks corresponding to Mg_2Sn with a = 6.764 Å, (Mg) and

(Sn). The d-values are labelled (in Ångtrøm) for the $Mg_2Si_{1-x}Sn_x$ peaks in all of the diffractograms in this text.

The diffractogram of sample $Mg_2Si_{0.50}Sn_{0.50}$-700, which was synthesized in a B_2O_3 flux, is presented in Figure 5.15. The diffractogram has peaks from phases covering almost the entire range of lattice parameters for $Mg_2Si_{1-x}Sn_x$, and small individual peaks with a = 6.355 indicating the presence of pure Mg_2Si. The two strongest peaks correspond to phases with lattice parameters a = 6.462 and 6.659 Å.

Figure 5.16 shows the X-ray diffractogram of $Mg_2Si_{0.75}Sn_{0.25}$-700. The sample was made by solid state synthesis. The positions of the peaks from the phases of $Mg_2Si_{1-x}Sn_x$ correspond to interplanar distances consistent with lattice parameters a = 6.398 and 6.714 Å. The Si peaks are very tall, because the XRD was performed with Si powder as a reference.

The X-ray diffractogram of $Mg_2Si_{0.25}Sn_{0.75}$-750, which was also made by solid state synthesis, is presented in Fig. 5.17. The $Mg_2Si_{1-x}Sn_x$ peaks are in the form of triplets, although the 111- and 200 peaks appear as doublets, because of overlapping of adjacent peaks. The positions of the three peaks within each triplet correspond to phases with a = 6.645, 6.668 and 6.678 Å.

Powder XRD of bulk $Mg_2Si_{0.75}Sn_{0.25}$-1150 resulted in the diffractogram in Fig. 5.18. There is a set of single peaks close to the position of Mg_2Si peaks, and there are at least two sets of overlapping peaks close to the positions of Mg_2Sn peaks. The strongest peaks on the Si-rich side corresponds to a phase with a = 6.372, and the two most defined sets of peaks on the Sn-rich side a = 6.668 and 6.754 Å.

The X-ray diffractograms of $Mg_2Si_{0.25}Sn_{0.75}$-1100 and $Mg_2Si_{0.25}Sn_{0.75}$-1150, which were made by cooling a melt, are shown in Fig. 5.19. Both $Mg_2Si_{0.25}Sn_{0.75}$-1100 and $Mg_2Si_{0.25}Sn_{0.75}$-1150 have single peaks corresponding to "Mg_2Si" and at least two sets of overlapping peaks corresponding to "Mg_2Sn". The lattice parameters refined from the interplanar spacings calculated from the positions of the strongest peaks in $Mg_2Si_{0.25}Sn_{0.75}$-1100 are 6.382, 6.649 and 6.760, and those of $Mg_2Si_{0.25}Sn_{0.75}$-1150 are 6.393, 6.664 and 6.758 Å.

The conclusion is that in addition to $Mg_2Si_{1-x}Sn_x$ phases, all of the samples in this project contain some metallic Sn (except Mg_2Si-700), elemental Si (except Mg_2Sn-900) and periclase (MgO). Equilibrium was not obtained in any of the samples. Peaks are found on both sides of the positions of expected peaks for single phases with the nominal composition, in such a way that a mass balance is fulfilled in the system.

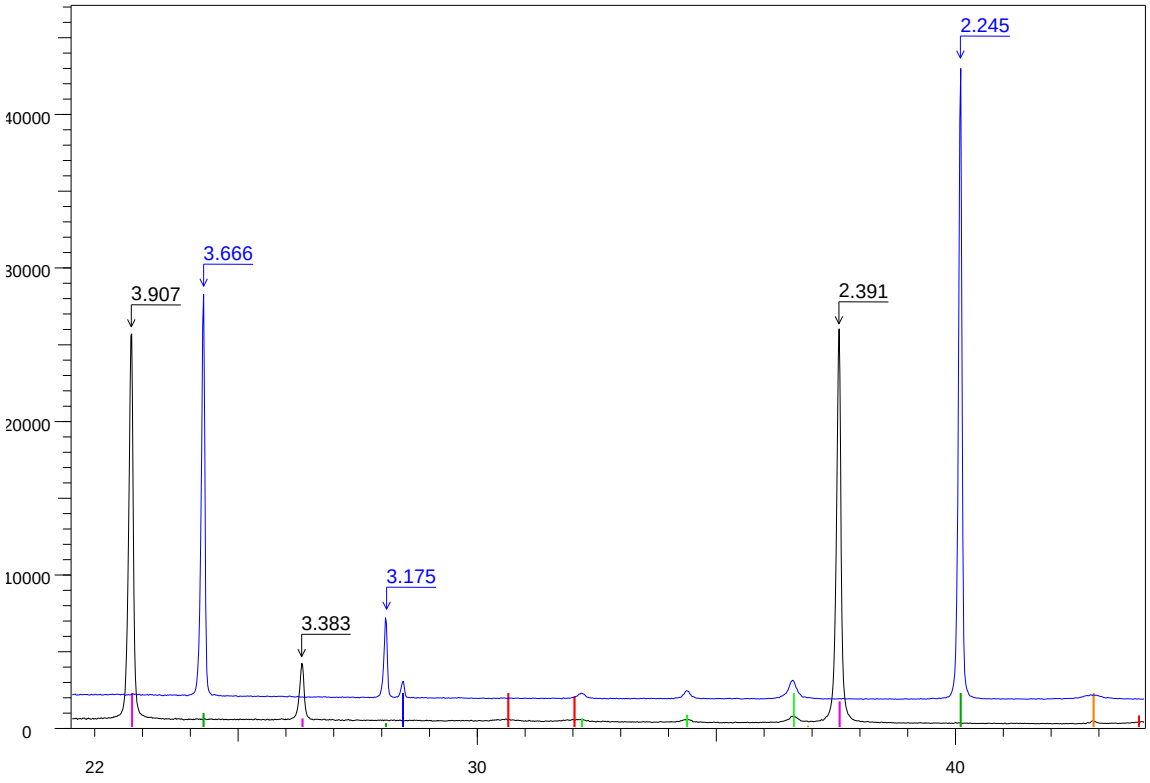

Figure 5.14: X-ray diffractograms of samples Mg_2Si-700 (blue) and Mg_2Sn (black). Mg_2Si-700, which was made by solid state synthesis, contains Mg_2Si (dark green), (Mg) (light green), (Si) (blue) and MgO (orange). Mg_2Sn-900, which was made by cooling a melt, contains Mg_2Sn (pink), (Mg) and (Sn) (red).

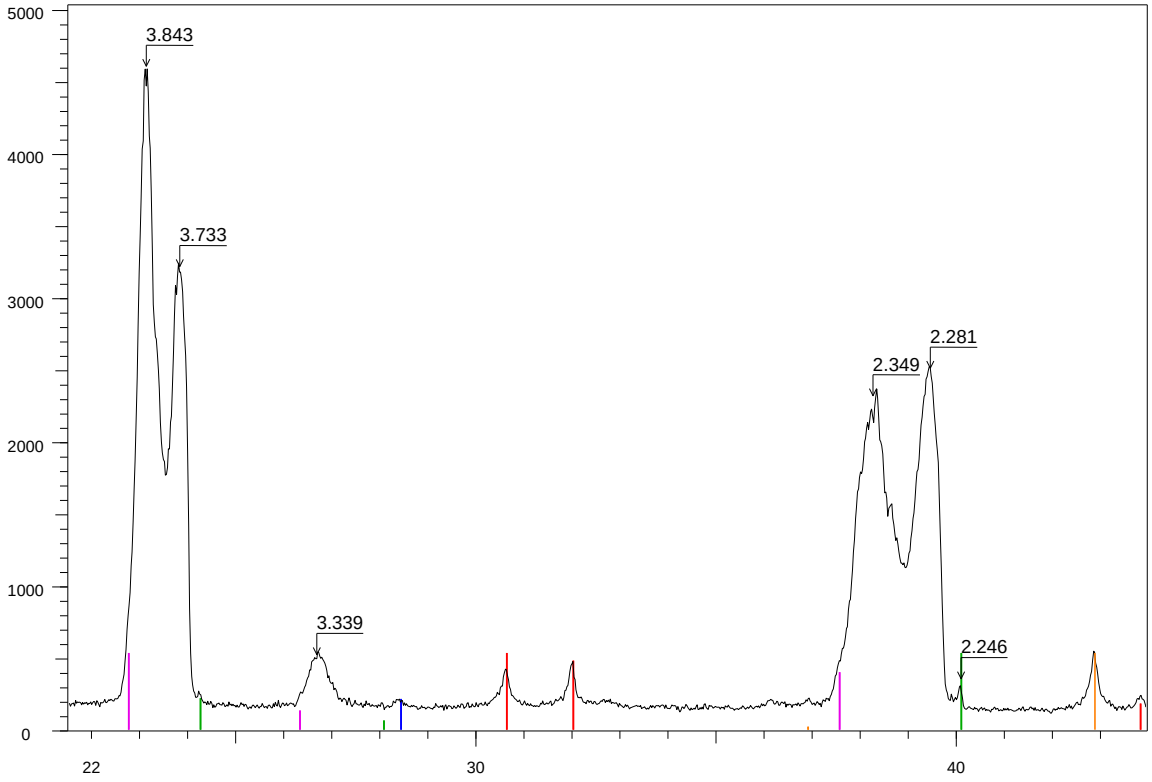

Figure 5.15: The X-ray diffractogram of an $Mg_2Si_{0.50}Sn_{0.50}$-700 sample, which was synthesized in a B_2O_3 flux, showing that it contains phases of $Mg_2Si_{1-x}Sn_x$ with a wide range of lattice parameters, (Sn) (red), (Si) (blue) and MgO (orange). The three strongest peaks correspond to phases with lattice parameters 6.355, 6.462 and 6.659 Å. The peak positions are shown for Mg_2Si (green) and Mg_2Sn (pink).

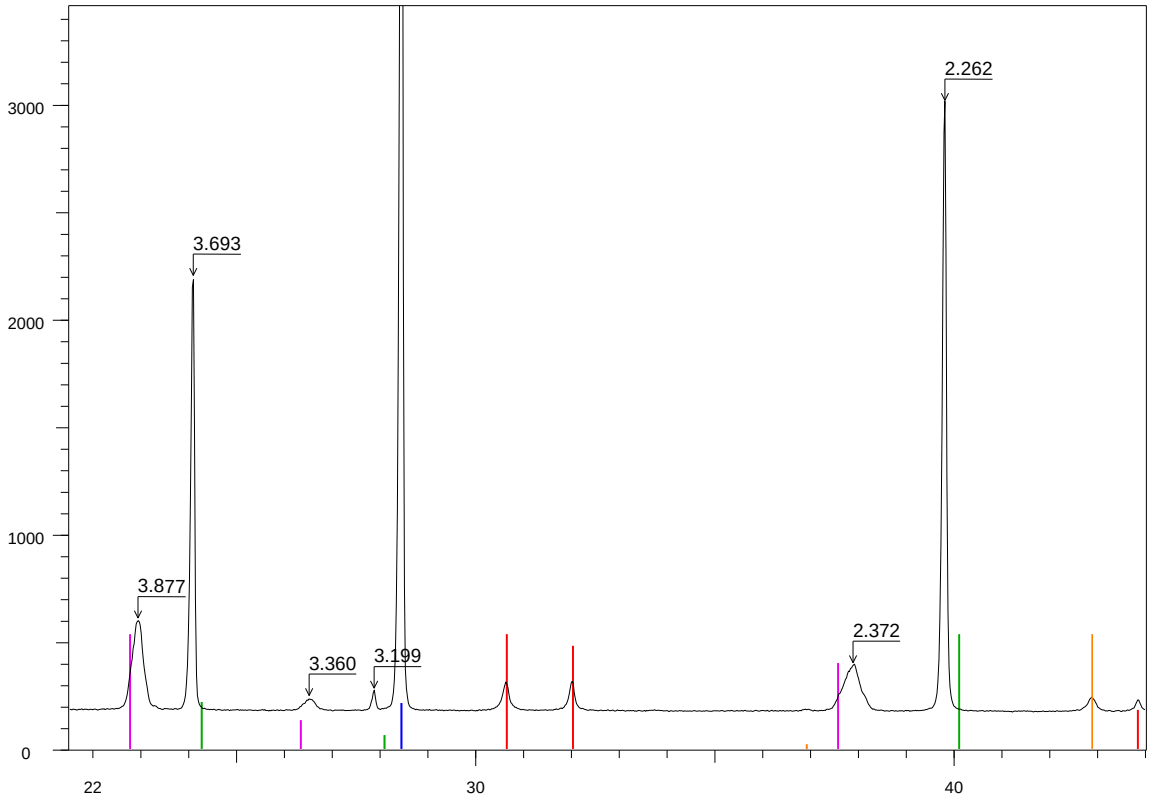

Figure 5.16: The X-ray diffractogram of $Mg_2Si_{0.75}Sn_{0.25}$-700, which was made by solid state synthesis, showing the presence $Mg_2Si_{1-x}Sn_x$ phases with interplanar distances consistent with lattice parameters of 6.398 and 6.714 Å, (Sn) (red) and MgO (orange). Si (blue) was added as a reference to this specimen, which is why the Si peaks are very tall. Peak positions are indicated for Mg_2Si (green) and Mg_2Sn (pink).

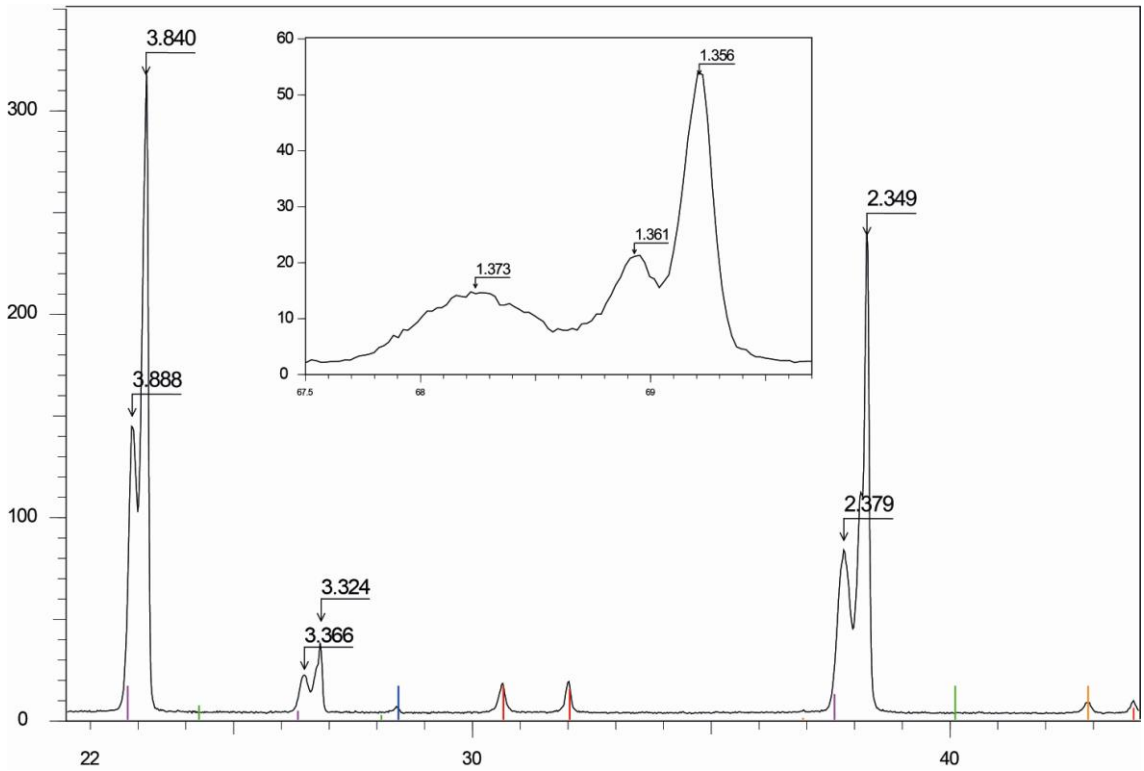

Figure 5.17: The X-ray diffractogram of $Mg_2Si_{0.25}Sn_{0.75}$-750, which was made by solid state synthesis. The sample contains $Mg_2Si_{1-x}Sn_x$ phases with different compositions resulting in overlapping peaks in the form of doublets and triplets, (Sn) (red), (Si) (blue) and MgO (orange). The peak positions are indicated for Mg_2Si (green) and Mg_2Sn (pink). The strongest peaks correspond to phases with lattice parameters of 6.645, 6.668 and 6.728 Å. The inset shows a triplet of the 420 peaks.

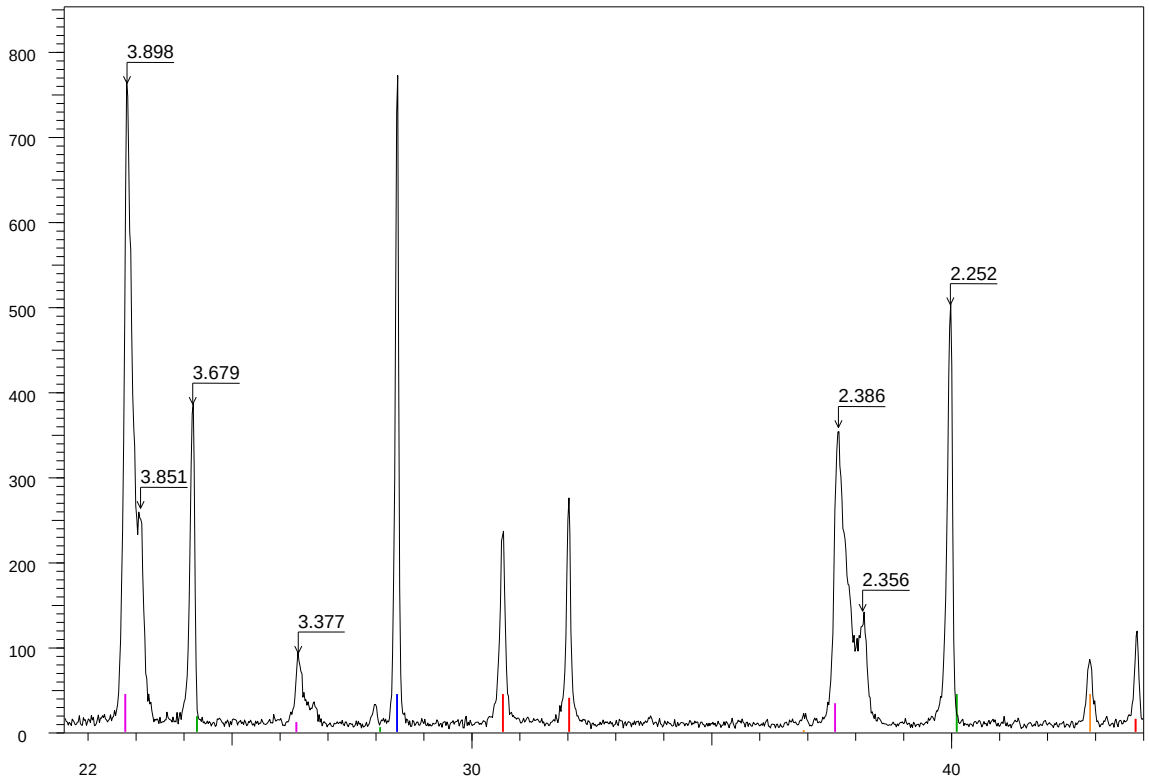

Figure 5.18: The X-ray diffractogram of $Mg_2Si_{0.75}Sn_{0.25}$-1150, which was made by solidifying a melt, showing the presence of $Mg_2Si_{1-x}Sn_x$ phases with different lattice parameters, (Sn) (red), (Si) (blue) and MgO (orange). Peak positions are indicated for Mg_2Si (green) and Mg_2Sn (pink). The strongest peaks correspond to phases with lattice parameters 6.371, 6.668 and 6.754 Å.

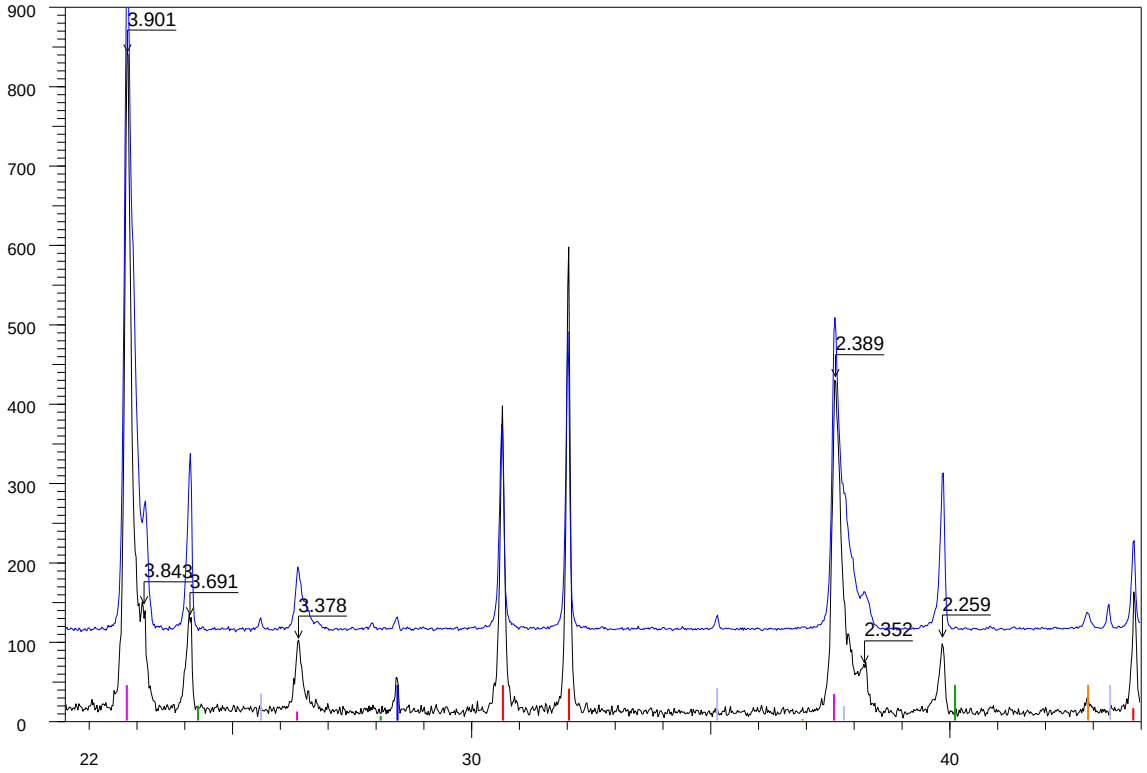

Figure 5.19: X-ray diffractograms of $Mg_2Si_{0.25}Sn_{0.75}$-1150 (black) and $Mg_2Si_{0.25}Sn_{0.75}$-1100 (blue), showing the presence of $Mg_2Si_{1-x}Sn_x$ with different lattice parameters, (Sn) (red), (Si) (blue) and MgO (orange). $Mg_2Si_{1-x}Sn_x$ also contains some Al_2O_3 (purple). Peak positions for Mg_2Si and Mg_2Sn are indicated (green and pink, respectively). The strongest $Mg_2Si_{1-x}Sn_x$ peaks correspond to phases with a = 6.393, 6.664 and 6.758 Å.

5.3 Nanostructural studies with transmission electron microscopy

Many $Mg_2Si_{1-x}Sn_x$ particles with several different values of x were analysed in powder, powder-glue composite and bulk TEM specimens with SAD and EDS in the JEOL 2000FX TEM. Many of the particles had inclusions of (Sn). Most of the crystals without (Sn) inclusions in the powder specimens were ~ 1.2 µm in diameter, and had compositions of $x \sim 0.12$ according to EDS analyses. Figs. 5.20, 5.21 and 5.22 present a bright field (BF) image, an energy dispersive spectrum, and a tilt series, respectively, from such a typical particle. The BF image of the particle is viewed along the [001] zone axis, and the composition is $Mg_2Si_{0.88}Sn_{0.12}$. According to the SAD patterns, the lattice parameter of the crystal is a = 6.369 Å. Several tilt series of selected area diffraction (SAD) patterns in the

JEOL 2000FX, such as the one in Fig. 5.22, confirmed that disordered $Mg_2Si_{1-x}Sn_x$ single crystals have face centred cubic lattices.

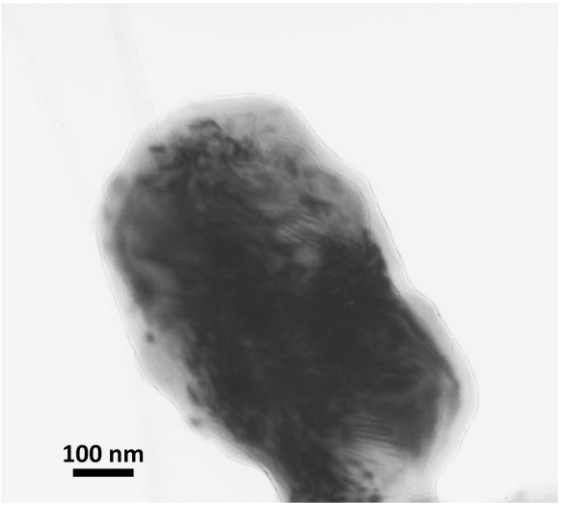

Figure 5.20: A BF image of an $Mg_2Si_{1-x}Sn_x$ particle, viewed along the [001] zone axis.

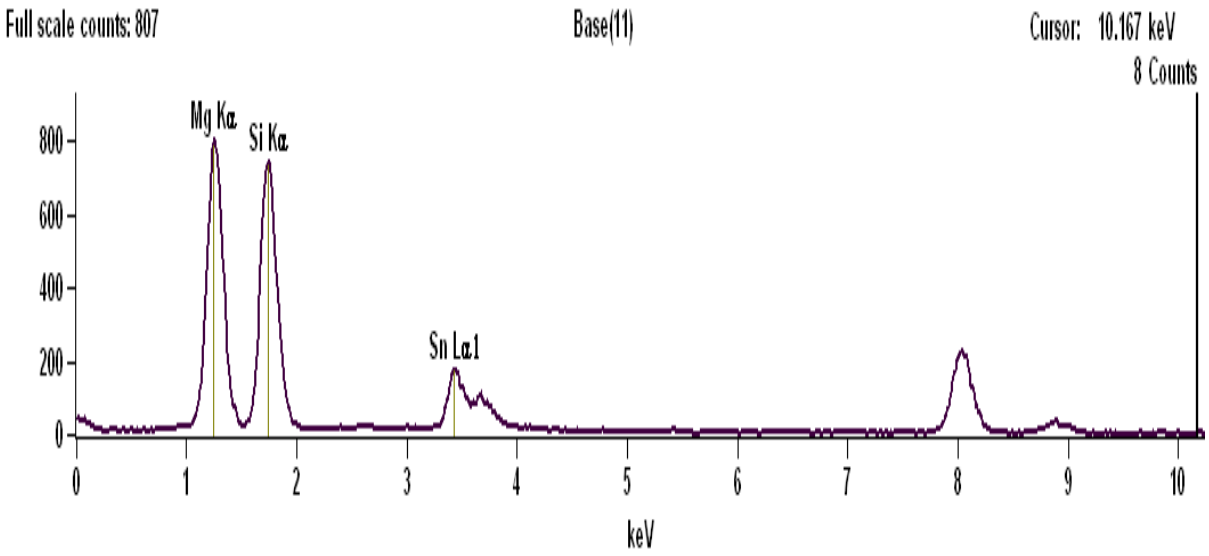

Figure 5.21: A quantified EDS spectrum obtained from a particle with composition $Mg_2Si_{0.88}Sn_{0.12}$.

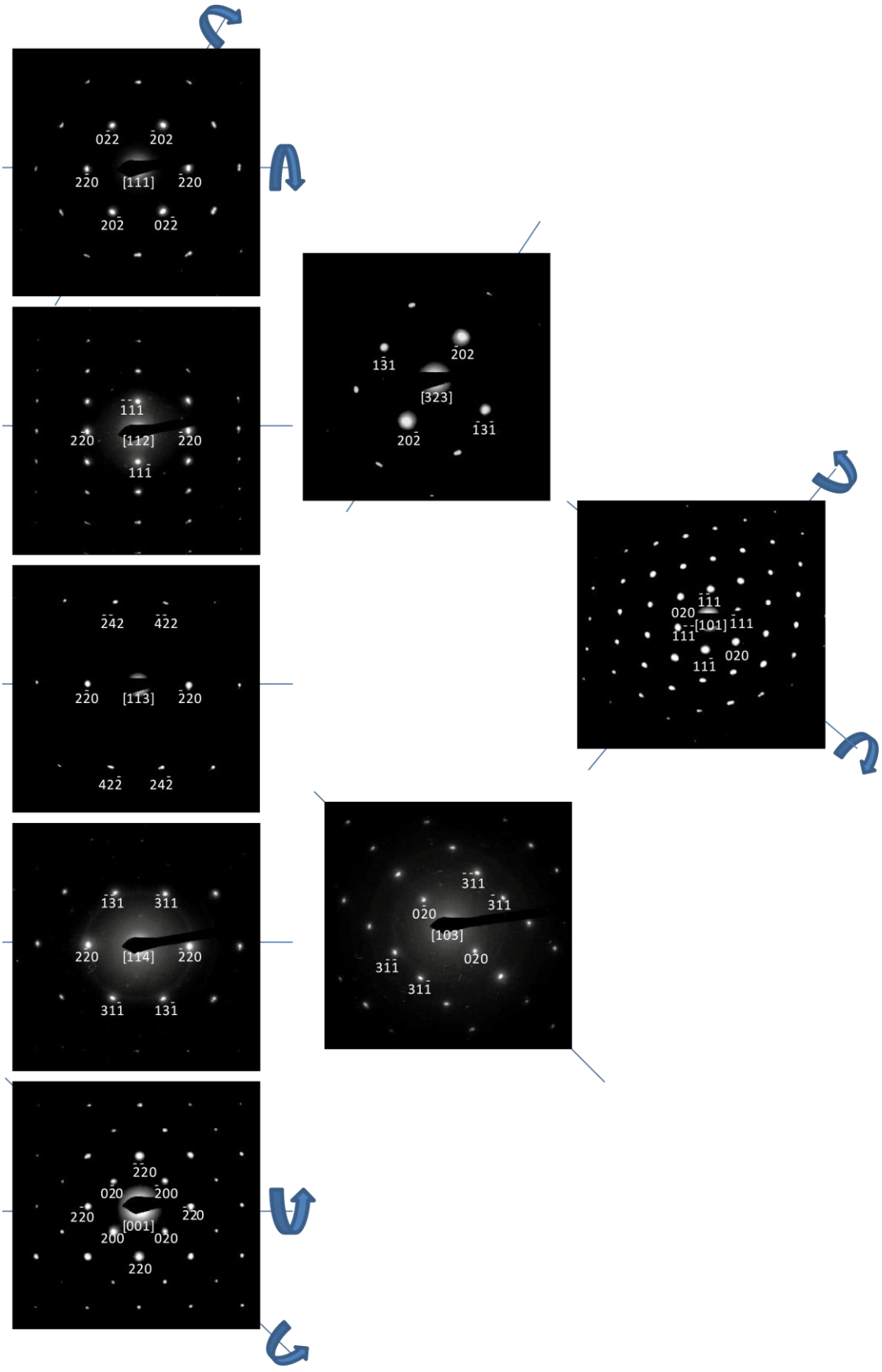

Figure 5.22: A tilt series map for a crystal with lattice parameter a = 6.369 Å and overall composition of $Mg_2Si_{0.88}Sn_{0.12}$.

Although most of the small crystals of $Mg_2Si_{1-x}Sn_x$ that were found with TEM had compositions with low values of *x*, a lot of time was spent on looking for single crystals with *x* close to 0.25, 0.50 and 0.75, because a few of them had weak reflections in some of their SAD patterns. They were only found in powder and powder-glue composite specimens of $Mg_2Si_{0.25}Sn_{0.75}$-750 and $Mg_2Si_{0.50}Sn_{0.50}$-700. Fig. 5.23 shows a tilt series of diffraction patterns of such a particle, with x = 0.56 and a = 6.612 Å. The diffraction patterns viewed along the [112] and [001] zone axes have weak reflections, which are kinematically forbidden in *fcc* lattices.

Fig. 5.24 shows the [112] diffraction pattern from the tilt series in Fig. 5.23. There are weak reflections midway between certain strong reflections in the 220- and parallel series. For instance, there is a -110 reflection between 000 and -220.

The [001] diffraction pattern in the tilt series in Fig. 5.23 has some weak reflections almost midway between certain strong reflections, and some reflections close to certain strong ones. The weak reflections very close to the main reflections will be referred to as satellites. The satellites are probably caused by a different effect than the reflections further away from the main reflections (as will be described in Chapter 6), they will be considered separately.

Fig. 5.25 shows a [100] diffraction pattern with weak reflections almost in the middle between two main reflections, similarly to those in the [001] diffraction pattern in the tilt series in Fig. 5.23. These reflections, which are kinematically forbidden in crystals with an fcc lattice, are in the form of spikes that stretch out toward their two closest reflections. The spikes are displaced from the middle of the two adjacent reflections by approximately 5 %. For instance, there is a weak reflection between the 020- and 022-reflections. It stretches toward both 020 and 022, but the centre is displaced toward 022. In this particle, x = 0.27 and a = 6.443 Å.

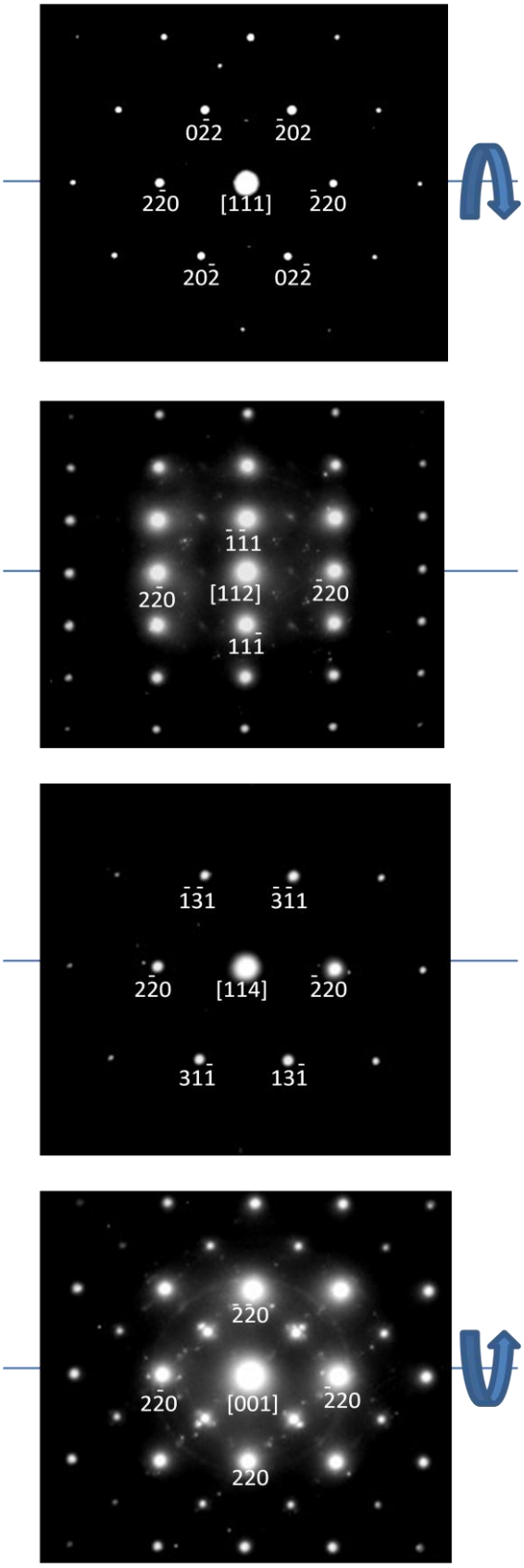

Figure 5.23: A tilt series of diffraction patterns of a particle with extra reflections in the [001] and [112] projections. The particle has a lattice parameter of a = 6.663 Å and an overall composition of $Mg_2Si_{0.44}Sn_{0.56}$.

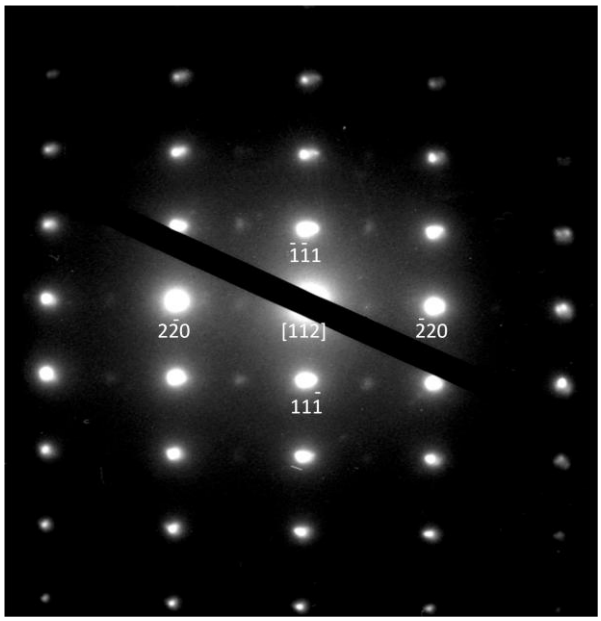

Figure 5.24: A [112] diffraction pattern of an $Mg_2Si_{0.44}Sn_{0.56}$ crystal. There are weak reflections in between two strong reflections, such as the -110 reflection between 000 and -220.

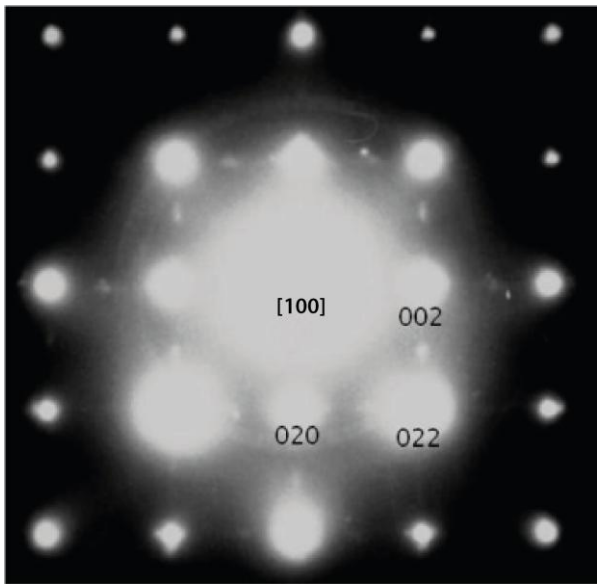

Figure 5.25: A [100] diffraction pattern of an $Mg_2Si_{0.73}Sn_{0.27}$ particle with a = 6.443 Å. There are weak reflections between two adjacent reflections, distorted from the middle by approximately 5 %.

A diffraction pattern of another particle, with x = 0.67 and a = 6.624 Å, viewed along the [113] zone axis is presented in Figure 5.26. There are extra reflections close to the central beam, as indicated in the figure. They belong to the 111-series of reflections and come from the first order Laue zone (FOLZ).

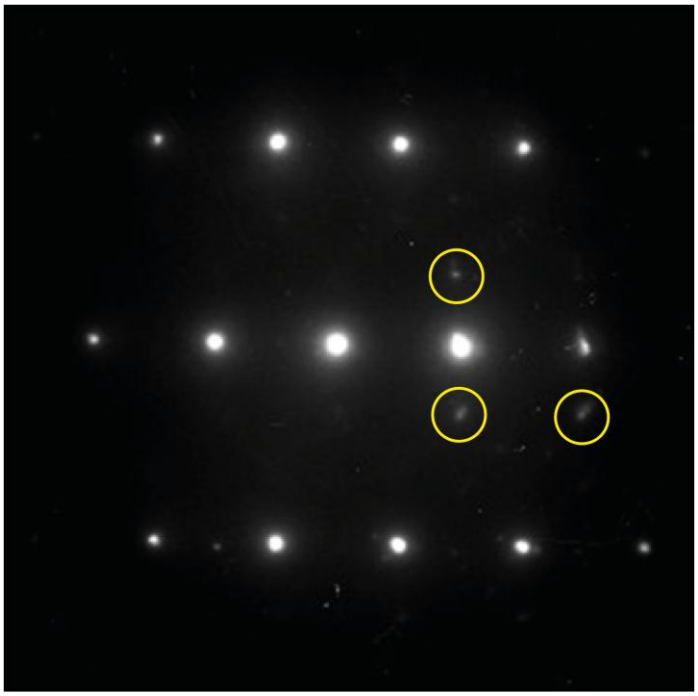

Figure 5.26: A [113] diffraction pattern with 111-type reflections from the FOLZ.

Figure 5.27 shows an [001] diffraction pattern of an $Mg_2Si_{0.44}Sn_{0.56}$ particle with a = 6.616 Å. It is similar to the [001] diffraction pattern in the tilt series of Fig. 5.23. The *hkl*-reflections where half of the sum of h and k is odd, i.e. $\frac{1}{2}h + \frac{1}{2}k = 2n + 1$, where n is an integer, are surrounded by four weak reflections, often referred to as satellites. The [001] diffraction pattern in the tilt series of Fig. 5.23 has four satellites around 200-type reflections, as well as the extra reflections almost midway between two strong reflections.

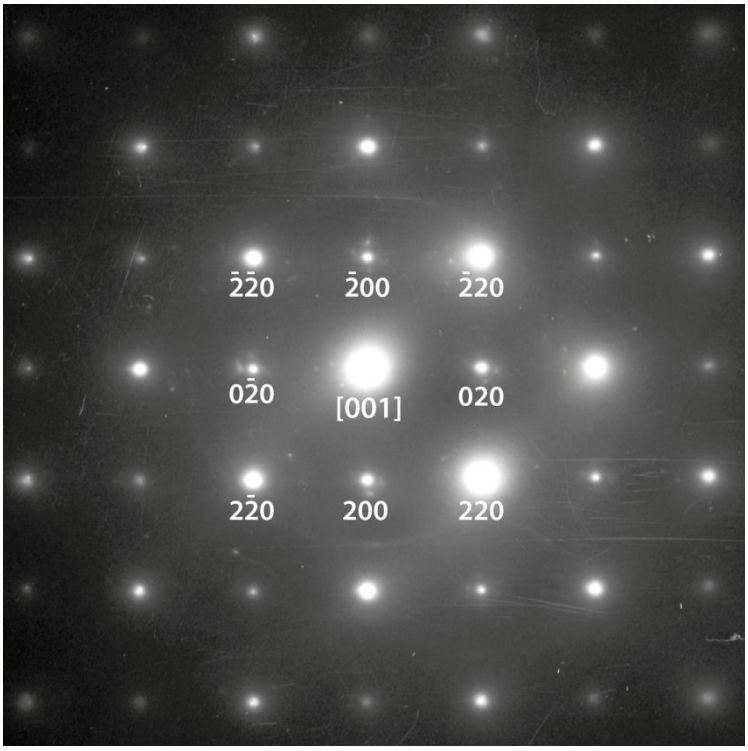

Figure 5.27: An [001] diffraction pattern of an $Mg_2Si_{0.44}Sn_{0.56}$ particle with a = 6.616 Å. The hkl-reflections with ½ h + ½ k = 2n + 1 are surrounded by four satellites.

Figure 5.28 shows a bright field (BF) image of a part of an ion beam thinned TEM specimen and two [110] diffraction patterns from two different areas of the specimen in the BF image. In the first diffraction pattern, the reflections along the 200 series have a weak reflection close to them, on the side furtherest from the direct beam. In the second, all of the reflections are surrounded by four weaker reflections. The satellites around 200 and -200 furthest away from the direct beam are more intense than the other satellites.

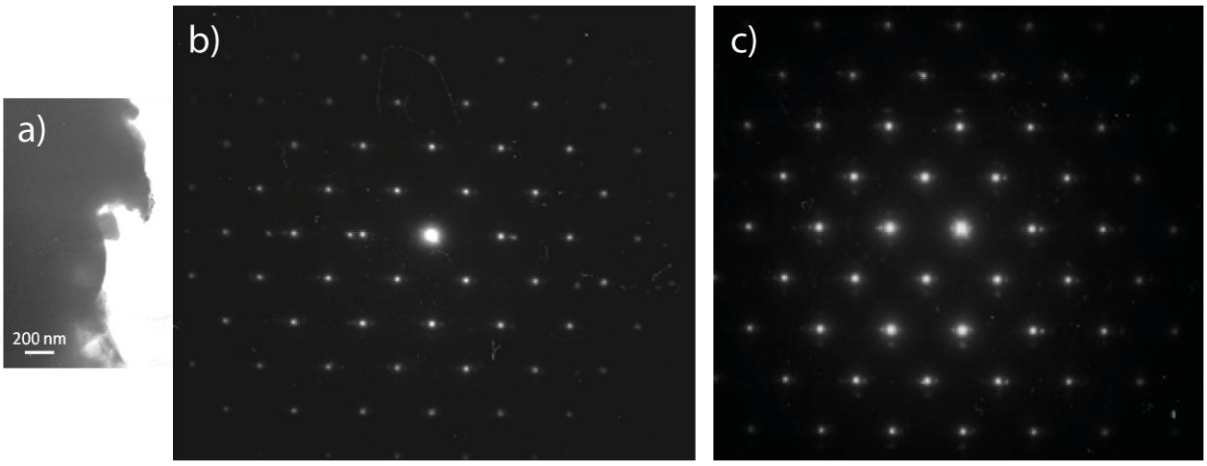

Figure 5.28: a) A BF image of $Mg_2Si_{0.39}Sn_{0.61}$ with a = 0.6.670 Å. b) A [110] diffraction pattern where the 200 series of reflections have weak satellites next to them, on the side furthest away from the direct beam. c) A [110] diffraction pattern where all of the main reflections are surrounded by four satellites.

A phase containing Mg, Si and N was found in an ion thinned composite specimen in the JEOL 2010F. This nitrogen-containing phase was only found in a sample made by the flux method, because the furnace it was heated in used air as atmosphere. A high resolution image and a selected area diffraction pattern of this nitride is presented in the Appendix (see Fig. A.1). Since the EDS system in the JEOL 2000FX cannot detect and quantify N, and all specimens but one were studied in the 2000FX, there is a chance that quite a few nitrides were studied during the present project.

6. Discussion

This chapter starts with a discussion of the synthesis procedures and experimental conditions in this project. The synthesis methods are evaluated and the obtained results are compared to what is published in the literature. Certain aspects of the characterization techniques are also discussed. Features of the products to be discussed include morphology, compositional analysis, phase separation, average crystal structure and local crystal structures. The last part is about diffraction effects observed in the JEOL 2000FX TEM, because little is known about the atomic structure of $Mg_2Si_{1-x}Sn_x$.

6.1 Synthesis methods

$Mg_2Si_{1-x}Sn_x$ is known to be a difficult system to work with, because of the volatility and reactivity of Mg and the difficulty of obtaining equilibrium. Another issue is the fact that several different immiscibility gaps have been reported. Equilibrium was not obtained in this project, as can be seen in many of the X-ray diffractograms and optical microscope and SEM images. The Mg powder used in the experiments carried out in this project had been exposed to air and was oxidized. It is unknown to what extent this may have affected the syntheses. The presence of small amounts of MgO in every sample could be due to this.

6.1.1 Solid state synthesis

As shown in section 5.2, the X-ray diffractogram of sample Mg_2Si-700 had single, non-overlapping peaks corresponding to Mg_2Si. The X-ray diffractogram of $Mg_2Si_{0.75}Sn_{0.25}$-700 also showed single, non-overlapping diffraction peaks from Si-rich ("Mg_2Si") and Sn-rich ("Mg_2Sn") antifluorite structures, but the peaks of "Mg_2Sn" were broader than those of "Mg_2Si" (see Fig. 5.16). Peak positions in the diffractograms did not change much after increasing the annealing time by a factor of two or three. $Mg_2Si_{0.75}Sn_{0.25}$-700 was the only $Mg_2Si_{1-x}Sn_x$ sample with $x \neq 0$ or 1 that gave single "Mg_2Si" and "Mg_2Sn" peaks, and is therefore the sample closest to equilibrium. The lattice parameters of the structures found by refining the diffraction peaks are a = 6.398 and 6.741, and correspond to compositions of x = 0.13 and 0.83, respectively (see Table 6.1 in ch. 6.2.4). Hence, these studies imply that the immiscibility gap in the phase diagram of Mg_2Si – Mg_2Sn ranges from x = 0.13 to x = 0.83 at

700 °C. Sample $Mg_2Si_{0.25}Sn_{0.75}$-750 had "Mg_2Sn" peaks in the form of triplets. The product had not reached equilibrium.

6.1.2 Solidification of homogeneous melts

There were no problems with synthesizing Mg_2Sn. Thermodynamic equilibrium was not obtained in samples $Mg_2Si_{0.25}Sn_{0.75}$-1100, $Mg_2Si_{0.25}Sn_{0.75}$-1150 or $Mg_2Si_{0.75}Sn_{0.25}$-1150. The melts may have mixed better had they been heated in a high-frequency furnace. The reason why Mg + Sn + Mg_2Si melted at 1100 °C and Mg_2Si + Mg_2Sn did not, could be that Mg_2Sn has a higher melting point (778 °C) than Mg (650 °C) and Sn (232 °C).

Figure 6.1 shows an example of what could happen when a melt of nominal composition $Mg_2Si_{0.75}Sn_{0.25}$ cools down, if the phase diagram has an immiscibility gap between $Mg_2Si_{0.60}Sn_{0.40}$ and $Mg_2Si_{0.40}Sn_{0.60}$. At a certain temperature the system will enter a two-phase area consisting of an "Mg_2Si" phase and a liquid (L). If a tie line is drawn inside such a two-phase area and the distance is measured from the starting composition to both boundaries along the line, the lever rule shows how much there is of each of the phases in the system. "Mg_2Si" crystals will form with compositions along the solidus line while the system is in the two-phase area, and as the temperature is lowered, the liquid phase will feed atoms to the crystals. As this happens, the liquid phase gets richer in Sn. If everything has been successful, the result should be a crystalline solid with the same composition as the nominal composition, when there is no more liquid left.

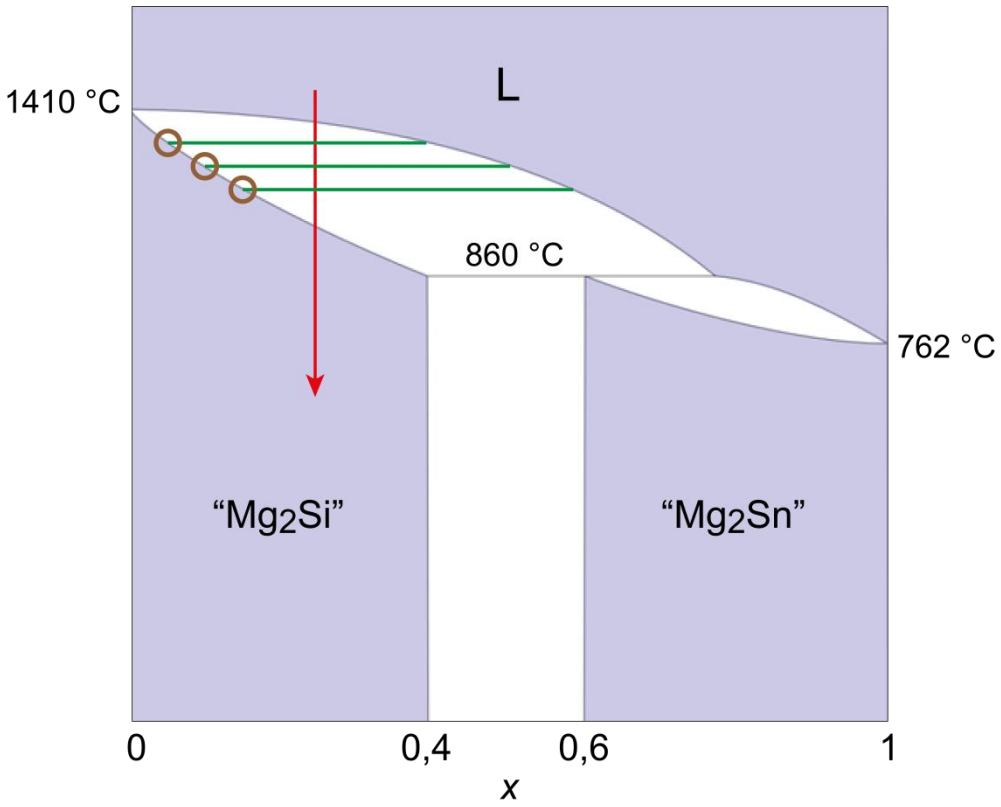

Figure 6.1: A phase diagram of the system $Mg_2Si_{1-x}Sn_x$, with a narrow immiscibility gap. The red arrow indicates the ideal phase transitions for synthesizing solids of $Mg_2Si_{0.75}Sn_{0.25}$. The green lines are tie lines at certain temperatures, showing that the present phases are “Mg_2Si” and a liquid. The brown circles indicate the compositions of “Mg_2Si” particles that may form while cooling the two-phase system (“Mg_2Si” + L).

In reality, it is not that simple. The sizes of crystals and the variations in composition within them depend on the cooling rates. The faster the cooling rates, the smaller the crystals, and the greater the composition range inside the crystals. If the melt is cooled rapidly, many small crystals rich in Si are formed. As the crystals grow there is not enough time for Sn atoms to diffuse all the way into the crystals and for Si atoms to diffuse all the way out. The product consists of crystals that vary in composition. The composition gradients are such that the crystals are rich in Si deep inside and rich in Sn in the outermost layers. While the system is being cooled down and there is still some melt in the sample, the melt is only in contact with the outermost layers of the crystals, which are rich in Sn. Since the parts richest in Si are inaccessible to the liquid, the whole system acts as if it is richer in Sn. Peritectic reactions, which is where a liquid and a solid react to form another solid (see equation 6.1), may occur for compositions of $x < 0.76$ (according to Fig. 6.1).

“Mg_2Si” + L → “Mg_2Sn” (6.1)

Crystals are then formed with the peritectic composition, and after further cooling, crystals of compositions close to Mg_2Sn are also formed.

If the melt is cooled slowly instead, there is plenty of time for diffusion and crystal growth. However, the crystals become so large that diffusion distances within them are too long. The result is a solid containing very large crystals. The compositions within the crystals vary, although not as much as in samples made by cooling rapidly. Some "Mg_2Sn" crystals grow as well.

A possible solution to the problem is to first quench the melt, so that crystals with small diffusion distances are formed, and then to anneal the system afterwards at a temperature below the solidus line, in order to get a single, homogeneous phase. In order to quench samples, e.g. in water, they must be in a closed system inside the furnace, because Mg_2Si reacts with water. Quartz glass ampoules are often used for such syntheses, but SiO_2 reacts with Mg and forms Mg-Si oxides. A tantalum (Ta) tube would be perfect, such as the ones used by Kozlov et al. [10] and Boudemagh et al. [15]. Unfortunately, Ta tubes and the tools needed to weld them and fill them with an inert atmosphere were unavailable when the experiments were carried out.

6.1.3 Flux method with boron oxide

One could question whether the B_2O_3 flux method carried out in this project really is a flux method. Powders were only formed when the reactants of the samples were covered by a layer of B_2O_3 powder (m.p. 450 °C), both in this project and by other researchers [19, 20]. The term "flux method" is correct for the syntheses where B_2O_3 powder was mixed with the reactants before heating them. However, the name "flux method" is used for all syntheses with B_2O_3 in this text, because that is what it is referred to among others who have used this method to synthesize $Mg_2Si_{1-x}Sn_x$ [19, 20].

Sodium chloride (NaCl) is quite often used to cover reactants in similar synthesis procedures, but was not used in the experiments in this project, because NaCl and Mg_2Si have similar densities. Boron oxide (B_2O_3) has a lower density than $Mg_2Si_{1-x}Sn_x$. When it is heated

together with Mg, Si and Sn, it moves to the top of the crucible. The volatility of B_2O_3 is relatively low at the temperature used in the syntheses, namely 700 °C, which is 250 ° C above the melting point of B_2O_3 [54].

The syntheses were carried out in air in an oven. The formation of oxides was a clear disadvantage. The products were glassy when the reactant powders were mixed with B_2O_3 or pressed into pellets before they were heated, because B_2O_3(l) transformed into a glass as the temperature was lowered. However, when the reactants were only covered with B_2O_3 powder, the product was $Mg_2Si_{1-x}Sn_x$ powder underneath a glassy layer of B_2O_3, which could easily be removed.

As previously mentioned, equilibrium was not reached in the experiments in this project. The X-ray diffractograms indicate a continuous distribution of phases with a range of different compositions, but there were no strong peaks corresponding to $Mg_2Si_{0.50}Sn_{0.50}$. Researchers who have synthesized a single phase of $Mg_2Si_{0.50}Sn_{0.50}$ with the B_2O_3 flux method, such as Gao et al. [19] and Chen et al. [20], hot-pressed their products. None of the samples in this project were sintered. Chen et al. [20] carried out similar experiments as Gao et al. [19] for samples of several different nominal compositions, and came to the conclusion that the system $Mg_2Si_{1-x}Si_x$ has a narrow immiscibility gap that does not cover $x = 0.50$.

6.2 Characterization

The four characterization methods used in this project, namely XRD, optical microscopy, SEM and TEM, each have their strengths and weaknesses, as explained in Chapter 3. The purpose of using all of them is that they complement each other.

6.2.1 Morphology of bulk samples

The samples that were solidified from a melt, namely $Mg_2Si_{0.75}Sn_{0.25}$-1150, $Mg_2Si_{0.25}Sn_{0.75}$-1150 and $Mg_2Si_{0.25}Sn_{0.75}$-1100, were not homogeneous and had not reached equilibrium. However, the distribution of different phases was similar in the products, as shown in the overview images obtained in the optical reflection microscope and SEM (see Figs. 5.3 and 5.4). Hence, they were homogeneous on a large scale.

Their ground and polished surfaces became oxidized over time, because they were not protected from moist in the air. Another factor that contributed to the oxidation, especially of the "Mg_2Sn" phases, is that water was used as a cooling medium during grinding, and water-based lubricant (Struers DP green [46]) was applied during polishing. Near the end of the present project, it was discovered that the surfaces should have been ground with ethanol and polished with an alcohol-based lubricant (Diamond polishing system, yellow [46]). This was attempted, and the surfaces looked much better, but there was not enough time to study the samples further.

6.2.2 Compositional analysis with energy dispersive spectroscopy

As previously mentioned, as *x* increases in $Mg_2Si_{1-x}Sn_x$, the amount of Mg seems to decrease with respect to Si and Sn in some samples according to EDS analyses. This may be because of Mg vacancies (see section 6.2.6), or by the presence of tin oxides. As previously mentioned, bulk "Mg_2Sn" is easily oxidizes if water is used as a coolant while grinding and the specimens are left unprotected for days.

6.2.3 The width of the immiscibility gap

It is still unknown where the two phase boundaries are in the Mg_2Si – Mg_2Sn system. Many researchers who reported a narrow immiscibility gap had hot-pressed their products [6, 3, 20], while others who reported a wide gap did not sinter their samples [5, 10]. Those who synthesized a single phase of $Mg_2Si_{0.50}Sn_{0.50}$ hot-pressed their products as well [17, 18, 19, 20, 21, 22]. This may, of course, be a coincidence. Although equilibrium was not obtained in the samples in this project, the samples made by solid state synthesis at 700 °C had the narrowest peaks in the X-ray diffractograms. The lattice parameters corresponding to these diffraction peaks indicate that the system has a wide miscibility gap. The samples in this project were not sintered.

Chen et al. claim that the disagreement of the range and existence of the immiscibility gap among researchers may be partly due to different amounts of Mg in their materials. The positions of the boundaries vary with the Mg content, as can be seen in the Mg-Si-Sn ternary

phase diagram (see Fig. 1.2). However, it is more probable that the system $Mg_2Si - Mg_2Sn$ has a wide miscibility gap at ambient pressures and a narrower gap at higher pressures. Hence, $Mg_2Si_{0.50}Sn_{0.50}$ could be a high pressure phase.

6.2.4 Average crystal structure of $Mg_2Si_{1-x}Sn_x$

Although some TEM diffraction patterns of $Mg_2Si_{1-x}Sn_x$ grains had weak reflections that are kinematically forbidden in face centred cubic lattices, these reflections were absent in the X-ray diffractograms. Powder XRD is used to determine what most of a sample contains, but there has to be a significant amount of a phase to give rise to visible peaks. There were very few crystals giving extra reflections in the diffraction patterns in the samples. They were found in the TEM because $Mg_2Si_{1-x}Sn_x$ crystals with compositions close to x = 0.25, 0.50 and 0.75 were selected for structural studies by selected area electron diffraction (SAED), and some of them had weak reflections in their diffraction patterns. These compositions were favoured for structural determination in the TEM, because of the possibility of finding superstructures (see section 6.2.7). Table 6.1 lists the lattice parameters refined from $Mg_2Si_{1-x}Sn_x$ peaks obtained with XRD and their corresponding compositions according to a curve relating lattice parameter and composition (see Fig. 1.7, Section 1.5). The curve was fitted to data by Nikitin et al. [6]. Also, the compositions from EDS analyses of the bulk samples in the SEM are added for comparison.

Table 6.1: Lattice parameters refined from the strongest $Mg_2Si_{1-x}Sn_x$ peaks from the presented X-ray diffractograms, the corresponding compositions of the phases according to a curve relating lattice parameter and composition based on data by Nikitin et al. [6], and compositions of the bulk samples found by SEM (see Table 5.1, Section 5.1.3).

Sample	**Lattice parameters [Å]**	**Composition [x]**	**EDS analysis with SEM**
Mg_2Si	6.352	0.00	-
$Mg_2Si_{0.75}Sn_{0.25}$-700	6.398 6.714	0.13 0.83	-
$Mg_2Si_{0.75}Sn_{0.25}$-1150	6.372 6.668 6.754	0.06 0.74 0.94	0.08 0.15 0.55 0.65
$Mg_2Si_{0.50}Sn_{0.50}$	6.355 6.462 6.659	0.027 0.28 0.72	-
$Mg_2Si_{0.25}Sn_{0.75}$-750	6.645 6.668	0.69 0.74	-

	6.728	0.86	
$Mg_2Si_{0.25}Sn_{0.75}$-1100	6.382 6.649 6.760	0.09 0.70 0.96	0.10 0.22 0.69 0.82 0.94
$Mg_2Si_{0.25}Sn_{0.75}$-1150	6.393 6.664 6.758	0.11 0.74 0.96	0.21 0.31 0.67 0.72 0.77
Mg_2Sn	6.764	1.00	-

It is not surprising that more phases seem to have been characterized in the bulk samples with SEM than with XRD. Firstly, only the strongest $Mg_2Si_{1-x}Sn_x$ peaks were chosen in the X-ray diffractograms for the table. The Sn-rich peaks in $Mg_2Si_{0.25}Sn_{0.75}$-1100 and $Mg_2Si_{0.25}Sn_{0.75}$-1150 were in the form of triplets (see Fig. 5.19), and those in $Mg_2Si_{0.75}Sn_{0.25}$-1150 were relatively broad (see Fig. 5.18), which means there were more phases with more compositions in the samples than indicated in Table 6.1. Secondly, the spatial resolution for X-ray emission influences EDS data in SEM. If a phase is thin, the data may be affected by other phases underneath.

It is strange, however, that the compositions found from XRD data are very different from the compositions measured by EDS. Phases with composition $x > 0.90$ were not found in $Mg_2Si_{0.25}Sn_{0.75}$-1150 or $Mg_2Si_{0.75}Sn_{0.25}$-1150 in the SEM, although they were found in $Mg_2Si_{0.25}Sn_{0.75}$-1100 with EDS and in all three samples with XRD.

6.2.6 The effect of Mg vacancies in $Mg_2Si_{1-x}Sn_x$

There may be Mg vacancies that contribute to lower quantified values of Mg in EDS analyses with respect to Si and Sn. Experiments performed by Nolas et al. [55] indicate that Sb-doped Mg_2Si has Mg vacancies at certain doping concentrations, while still having the same structure. Mg and Si atoms in Mg_2Si (without vacancies) are reported to have electronic charges of + 1.45 and – 2.90, respectively [31]. Si atoms are more electronegative than Sn atoms. If Sn atoms are, on average, less negatively charged than Si atoms in $Mg_2Si_{1-x}Sn_x$, there may be Mg vacancies in order to compensate for this and maintain neutrality in the material. The concentration of vacancies cannot be too large, otherwise the structure would

collapse. $Mg_2Si_{1-x}Sn_x$ crystals with a small but significant amount of Mg vacancies should have smaller lattice parameters than crystals without such vacancies. Lattice constants increase with the amount of Sn on the anion positions, but decrease with Mg vacancies. In this project, it was assumed that the effect vacancies have on lattice parameters is negligible when compared to the effect of composition.

6.2.7 Local structures and diffraction effects

There are two diffraction effects that will be discussed in this section. The first is the appearance of weak reflections in or near the middle between strong adjacent reflections seen in the [112] and [001] selected area electron diffraction (SAED) patterns. These reflections will be referred to as "superstructure reflections" in this section. They could be due to reflections in the first order Laue zone (FOLZ), multiple scattering, or they may occur from local ordering phenomena, and so two proposed superstructures will be presented and evaluated. A third possible superstructure will also be presented.

The second effect is the appearance of weak reflections around and close to some of the main reflections, observed in [001] and [101] diffraction patterns. These weak reflections will from now on be referred to as "satellites". The presence of anti-phase boundaries (APBs), inclusions of epitaxially grown Sn and double diffraction will be considered as possible causes of the satellites.

6.2.7.1 Superstructure reflections in diffraction patterns of $Mg_2Si_{1-x}Sn_x$

Fig. 6.3 shows two diffraction patterns from different $Mg_2Si_{1-x}Sn_x$ particles. They are projected along the [112] and [001] zone axes, respectively. There are weak reflections between certain main reflections of $Mg_2Si_{1-x}Sn_x$. In the Mg_2Si – Mg_2Sn system one could expect ordering of the Si – Sn sub-lattice of the same kind as in the gold-copper system. Solid solutions of Au mixed with Cu have face centred cubic (*fcc*) lattices. For certain compositions of $Au_{1-x}Cu_x$, there are composition-dependent critical ordering temperatures (T_c) under which ordering of the crystal structure occurs [39]. Cu and Au are not randomly distributed on the *fcc* lattice positions under T_c. As already mentioned, solid solutions of $Mg_2Si_{1-x}Sn_x$ have an anti-fluorite structure. The Bravais lattice is *fcc*, with Si or Sn atoms on the corners and faces, and Mg atoms in all of the tetrahedral holes. Under a possible T_c, there

may be ordering of the Si and Sn atoms, while the Mg atoms are still in the tetrahedral holes. No published results of such ordering were found in the literature for this system.

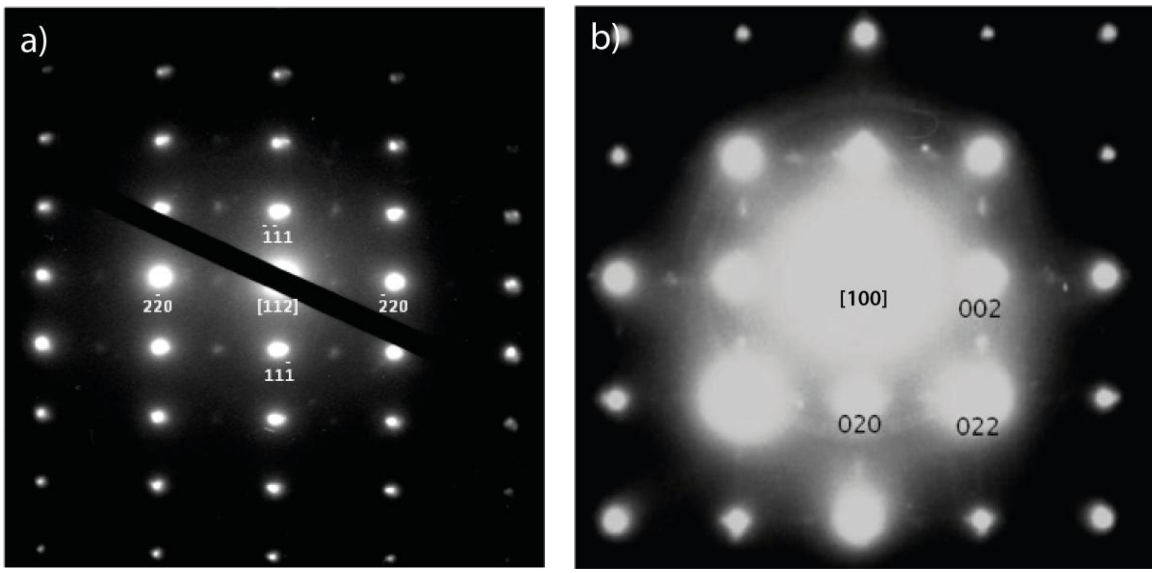

Figure 6.3: a) A [112] diffraction pattern with weak reflections between the main reflections in the 220 and parallel series. b) A [100] diffraction pattern with weak reflections between two adjacent main reflections in the 020 and parallel series, and in the 002 and parallel series.

Cu_3Au-type superstructures[2]*:*

Based on statistics, one could say (especially in regard to scattering factor calculations) that each lattice point is associated with 0.75 Cu atoms and 0.25 Au atoms for completely randomized structures of Cu_3Au. Under a certain T_c, the positions of Au and Cu are no longer randomly distributed. The lattice becomes primitive cubic, with Au atoms on the corners and Cu atoms on the faces [39]. The same type of superstructures may exist for $Mg_2Si_{1-x}Sn_x$ with x = 0.25 and 0.75. With such local ordering, the unit cell of $Mg_2Si_{0.75}Sn_{0.25}$ has Sn atoms on the corners and Si atoms on the faces, and vice versa for $Mg_2Si_{0.25}Sn_{0.75}$ (see Fig. 6.4). The Bravais lattice is primitive cubic, and so the lattice in reciprocal space should be primitive cubic as well, instead of body centred cubic (*bcc*). This structure has crystallographic space group Pm3m (cP12, number 222).

[2] There is more than one kind of ordered structure of Cu_3Au. The one discussed here is the Cu_3Au I superstructure, but will be referred to as Cu_3Au in this text.

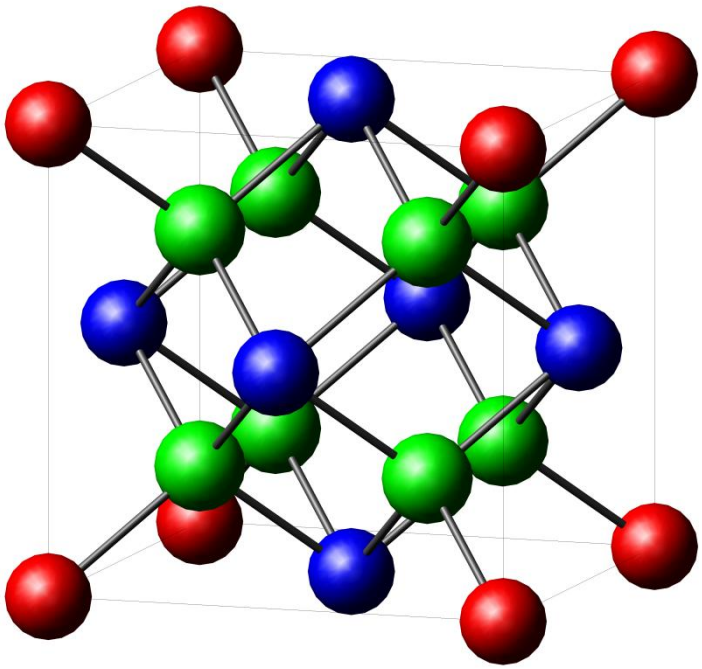

Figure 6.4: A model of a predicted filled Cu_3Au type superstructure of $Mg_2Si_{1-x}Sn_x$. The ordering is in such a way that Si atoms (red) are on the corners and Sn atoms (blue) are on the faces of a cubic unit cell of $Mg_2Si_{0.25}Sn_{0.75}$, and vice versa for $Mg_2Si_{0.75}Sn_{0.25}$. The Mg atoms (green) are still in the tetrahedral holes.

According to Vegard's law, there is a linear relationship between lattice parameter and *x* in alloys of disordered $Mg_2Si_{1-x}Sn_x$. However, there is usually a deviation to this law. Using Vegard's law and lattice constants of 6.351 Å for Mg_2Si [32] and 6.763 Å for Mg_2Sn [33], lattice parameters for $x = 0.25$ and 0.75 are 6.454 Å and 6.660 Å, respectively (see Table 6.2). Mg – Si and Mg – Sn bond lengths were calculated from the lattice parameters of the silicide and the stannide, respectively, by dividing the body diagonal of their unit cells by four. Mg – Si bond lengths are 2.750 Å and Mg – Sn bond lengths are 2.928 Å. In the unit cells of the Cu_3Au-based superstructure, the Si and Sn atoms form regular tetrahedral holes. However, Mg – Si bonds are shorter than Mg – Sn bonds. Therefore, Mg atoms are not in the middle of the tetrahedral holes. They are distorted toward the nuclei of the Si atoms, because Si atoms have a smaller radius than Sn atoms. After calculating the positions of the Mg atoms, the lattice parameters could be determined and structure factors computed.

The lattice parameters of $Mg_2Si_{0.75}Sn_{0.25}$ and $Mg_2Si_{0.25}Sn_{0.75}$ superstructures were calculated from the formulas in equations 6.2 and 6.3, respectively.

$$a = \frac{2l_{Mg-Sn} + \sqrt{6l_{Mg-Si}^2 - 2l_{Mg-Sn}^2}}{3} \quad (6.2)$$

$$a = \frac{2l_{Mg-Si} + \sqrt{6l_{Mg-Sn}^2 - 2l_{Mg-Si}^2}}{3} \quad (6.3)$$

where l_{Mg-Si} and l_{Mg-Sn} are the Mg – Si and Mg – Sn bond lengths.

Table 6.2 shows a comparison between the calculated lattice constants for solid solutions of $Mg_2Si_{0.75}Sn_{0.25}$ and $Mg_2Si_{0.25}Sn_{0.75}$ based on Vegard's law and for the superstructures. The values determined by a graph based on data by Nikitin et al. for solid solutions [6] are also given. Since calculated lattice parameters for the ordered structures are similar to those of the disordered structures with the same compositions, it is assumed that the lattice constants for the superstructures are equal to the measured values for the disordered structures. In other words, Nikitin et al.'s graph can be used for anticipating lattice parameters of Cu_3Au based superstructures.

Table 6.2: Lattice constants of disordered $Mg_2Si_{0.75}Sn_{0.25}$ and $Mg_2Si_{0.25}Sn_{0.75}$ according to Nikitin et al. [6] and calculated by Vegard's law, and that of Cu_3Au-based superstructures with the same compositions calculated from Mg-Si and Mg-Sn bond lengths.

Compound	Nikitin et al. [6]	Vegard's law	Superstructures
$Mg_2Si_{0.75}Sn_{0.25}$	6.45 Å	6.454 Å	6.449 Å
$Mg_2Si_{0.25}Sn_{0.75}$	6.68 Å	6.660 Å	6.655 Å

The structure factors of the possible superstructures were calculated for $Mg_2Si_{0.75}Sn_{0.25}$ (equation 6.4) and for $Mg_2Si_{0.25}Sn_{0.75}$ (equation 6.5). The values inside the cosine functions are multiplied by 0.492 for the Si-rich structure and 0.508 for the Sn-rich structure, in order to take into account that Mg atoms are distorted toward the nuclei of the Si atoms and away from the nuclei of the Sn atoms by 0.4 % inside tetrahedral holes.

$$F_{hkl} = f_{Sn} + f_{Si}\left(e^{\pi i(h+k)} + e^{\pi i(h+l)} + e^{\pi i(k+l)}\right)$$
$$+2f_{Mg}\cos\left(0.492\pi(h+k+l)\right)\cdot\left(1 + e^{\pi i(h+k)} + e^{\pi i(h+l)} + e^{\pi i(k+l)}\right) \quad (6.4)$$

$$F_{hkl} = f_{Si} + f_{Sn}\left(e^{\pi i(h+k)} + e^{\pi i(h+l)} + e^{\pi i(k+l)}\right)$$
$$+2f_{Mg}\cos\left(0.508\pi(h+k+l)\right)\cdot\left(1 + e^{\pi i(h+k)} + e^{\pi i(h+l)} + e^{\pi i(k+l)}\right) \quad (6.5)$$

Fig. 6.5 shows the [112] diffraction pattern from Fig. 6.3. It has been indexed as if it belonged to a primitive cubic lattice. The diffraction pattern is consistent with the predicted model of a filled Cu_3Au-type superstructure.

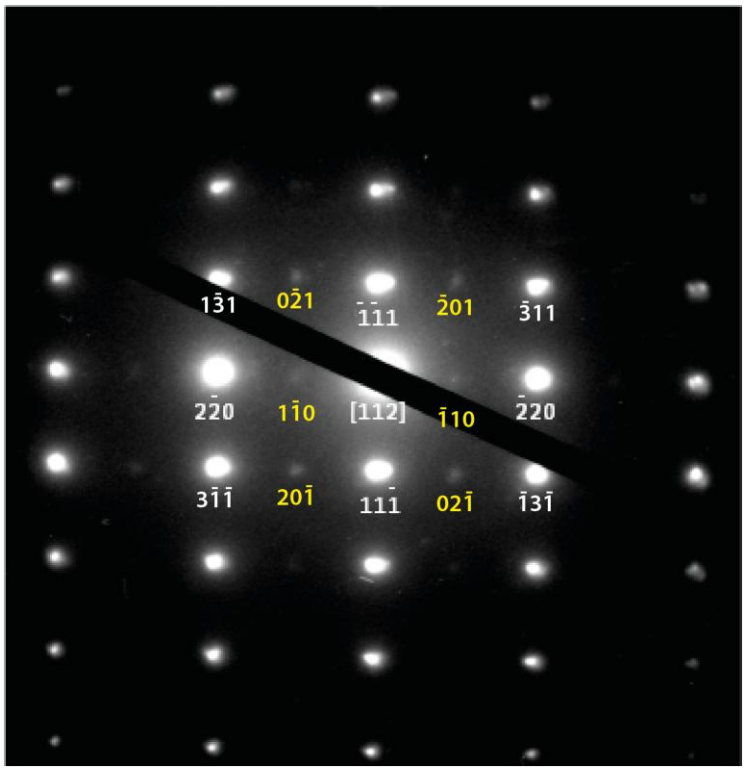

Figure 6.5: A [112] diffraction pattern indexed as a primitive cubic lattice. The superstructure reflections are indexed with yellow numbers.

After performing tilt series of diffraction patterns of several crystals in the 2000FX TEM, it was concluded that the Cu_3Au type of ordering of the Si – Sn sub-lattice had not been observed in $Mg_2Si_{0.75}Sn_{0.25}$ or $Mg_2Si_{0.25}Sn_{0.75}$, because the 110-type reflections are not present in [114], [113], [332] or [110] diffraction patterns (see tilt series in Fig. 5.23, Section 5.3).

Domains with CuAu I-type superstructures:

The copper – gold system has a composition range in which a CuAu superstructure exists under a certain T_c, where planes of Cu atoms and Au atoms alternate in the [001]-direction

[39]. This structure has a tetragonal lattice, both in real space (where $c < a$) and in reciprocal space (where $c^* > a^*$). If such ordering occurs for $Mg_2Si_{0.50}Sn_{0.50}$, the lattice is C-centred tetragonal, with alternate layers of Si and Sn atoms in the [001] direction (see Fig. 6.6). However, conventionally thinking, there is no such thing as a C-centred tetragonal Bravais lattice. In order to keep the symmetry as simple as possible, the Bravais lattice is a primitive tetragonal lattice (crystallographic space group P4/mmm, tP6, number 123), where the corners are the points corresponding to ½ ½ 0 positions from the C-centred lattice (see Fig. 6.6). Structure factors of this possible superstructure were not calculated as accurately as for the filled Cu_3Au-type structure. It was assumed, for simplicity, that the Mg atoms lie in the middle of the non-regular tetrahedral holes formed by two Si atoms and two Sn atoms (see Eq. 6.6).

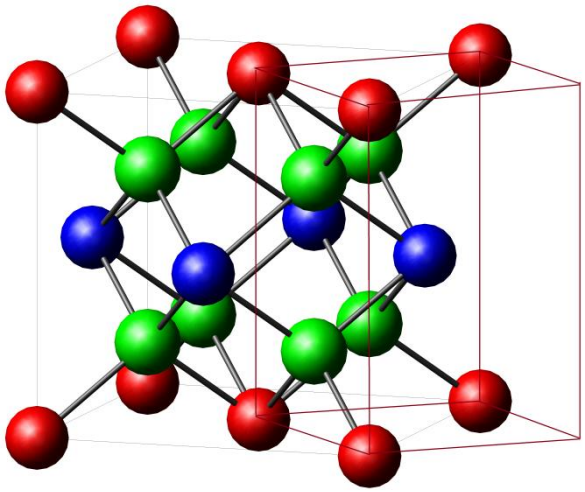

Figure 6.6: A model of a possible CuAu I-type superstructure of $Mg_2Si_{0.50}Sn_{0.50}$. The ordering is in such a way that planes of Si atoms (red) and Sn atoms (blue) alternate in the [001]-direction. The Mg atoms (green) are still in the tetrahedral holes. Brown lines indicate a conventional primitive cubic Bravais lattice for this structure.

Using the C-centred lattice as a model for ordered $Mg_2Si_{0.50}Sn_{0.50}$ rather than the conventional primitive tetragonal lattice, as it is easier to compare with disordered $Mg_2Si_{1-x}Sn_x$ unit cells, the structure factor is then calculated as follows:

$$F_{hkl} = f_{Sn}\left(1 + e^{\pi i(h+k)}\right) + f_{Si}\left(e^{\pi i(h+l)} + e^{\pi i(k+l)}\right) + 2f_{Mg}\cos\left(\frac{\pi}{2}(h+k+l)\right)\cdot\left(1 + e^{\pi i(h+k)} + e^{\pi i(h+l)} + e^{\pi i(k+l)}\right) \quad (6.6)$$

The reflection conditions for a C-centred tetragonal lattice are $h + k = 2n$.

The relation between lattice constants *c* and *a* is as follows:

$$c = 2 \cdot \left(\sqrt{l_{Mg-Si}^2 - \frac{1}{8}a^2} + \sqrt{l_{Mg-Sn}^2 - \frac{1}{8}a^2} \right) \tag{6.7}$$

where $l_{Mg\text{-}Si}$ and $l_{Mg\text{-}Sn}$ are the Mg – Si and Mg – Sn bond lengths, respectively. For the special case when $c = a$, then $a \sim 6.55$ Å, which is approximately the theoretical value of *a* for a disordered single phase of $Mg_2Si_{0.50}Sn_{0.50}$, based on Vegard's law.

Figure 6.7 shows a [112] and a [100] diffraction pattern obtained from the same particle. Both patterns have weak extra reflections and are indexed as C-centred tetragonal lattices. They are consistent with the predicted model of CuAu I-type superstructures of $Mg_2Si_{1-x}Sn_x$. If that is the case, the extra reflections in the [100] diffraction pattern are due to two different domains that are oriented at 90 ° relative to each other in the image plane (see Fig. 6.8). The reflections that are stretched horizontally stem from one set of equally oriented domains, and the reflections stretching vertically come from another. The weak reflections are spikes, because the domains are thin. Judging by the length of the spikes, the domains are approximately 20 Å thick.

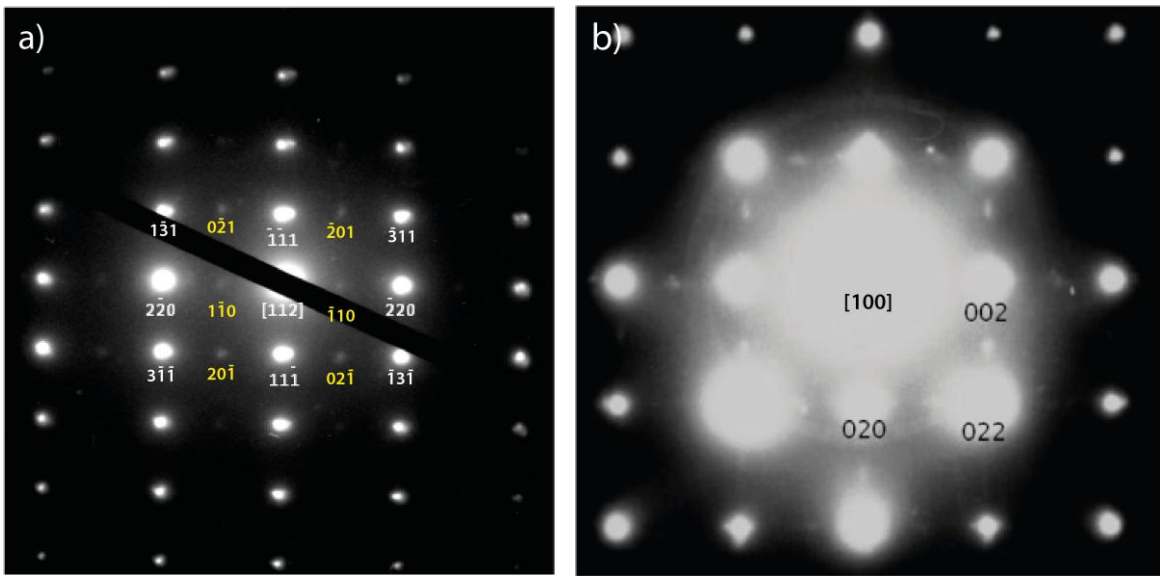

Figure 6.7: A [112] (left) and a [100] diffraction pattern (right) indexed as a C-centred tetragonal lattice. The weak reflections in the latter come from at least two thin, mutually orthogonal domains.

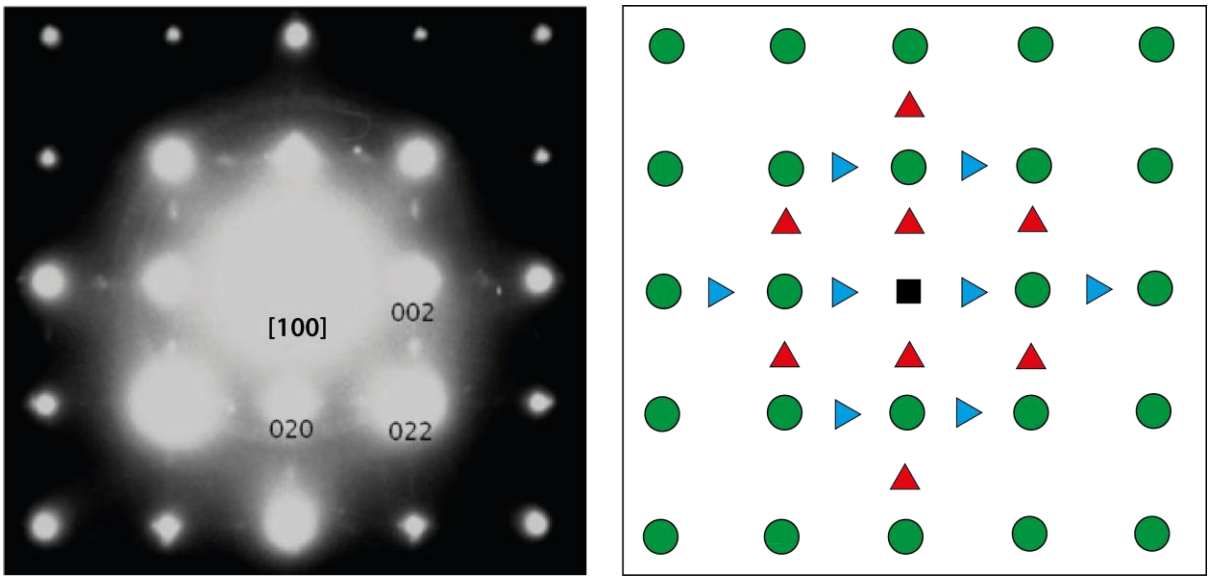

Figure 6.8: A [100] diffraction pattern (left) and a schematic showing how two thin, mutually orthogonal domains may combine to form a diffraction pattern (right). Green circles represent the main reflections. Red triangles represent weak reflections due to one domain and blue triangles represent weak reflections caused by another domain.

After performing tilt series of diffraction patterns, it was concluded that the particles did not have CuAu I-type of ordering of the Si- and Sn atoms, because the extra reflections that were present when viewed along [112] and [100] zone axes were absent in [114] and [111] diffraction patterns (see tilt series in Fig. 5.23, Section 5.3). Also, it would be strange if there were only mutually orthogonal domains with *c* parallel to the diffraction plane, and none with *c* perpendicular to it.

Higher order Laue zones:

Another possible reason for why extra reflections were only observed in [112] and [001] diffraction patterns was that the first order Laue zone (FOLZ) was projected onto the zero order Laue zone (ZOLZ) of a crystal with an anti-fluorite structure. The number of reflections in a reciprocal plane is inversely proportional to the distance between the reciprocal planes. In other words, the area enclosed by four spots in the obtained diffraction patterns (e.g. 000, 11-1, 13-1 and -220 in a [112] diffraction pattern) is relatively small, so that the height between the ZOLZ and FOLZ in the perpendicular direction (pointing out of the plane of this paper) is relatively large. Hence, based on a qualitative description of reciprocal lattice cells, it is improbable that the weak reflections are due to the FOLZ. As already mentioned in section 5.3, 111-type reflections were projected from the FOLZ onto a [113] diffraction

pattern (see Fig. 5.26, see Section 5.3). This is possible because the distances between the reflections in [113] diffraction patterns are large, so the distance to the FOLZ is much shorter, and because the 111-type reflections were spikes. The spikes were neither parallel nor perpendicular to the Ewald sphere, but diagonally oriented.

Multiple scattering

It was first assumed that the particles giving SAD patterns with extra reflections in only some projections did not have any ordering, but that the weak reflections were due to multiple scattering in a crystal having the anti-fluorite structure. However, although there may have been (and most likely were) double diffraction events occurring inside the crystals, multiple scattering cannot be the only reason for the weak reflections appearing. The *g*-vector of a forbidden reflection has to be the sum of at least two *g*-vectors of allowed reflections, which is certainly not the case for g_{100} in an *fcc* lattice. Thus, at least one of the weak reflections cannot be due to double diffraction.

If one takes a closer look at [112] diffraction patterns, it seems that the intensity of the 210-type reflections are greater than that of 110-type reflections (see Fig. 6.7). It could be that 210 and equivalent reflections are due to ordering of the crystal structure of $Mg_2Si_{1-x}Sn_x$, and that the 110 and equivalent reflections are caused by multiple scattering events. The 110 reflections disappeared by tilting away from the projection. That explains the presence of the 210-type and 100-type of reflections and the absence of the 110-type of reflections in the [001] diffraction patterns. Therefore, there may be another kind of superstructure of $Mg_2Si_{1-x}Sn_x$.

CuAu II-type superstructures:

There is another ordered structure of Cu and Au known as CuAu II. The superstructure consists of CuAu I-type domains separated by anti-phase boundaries (APBs) (See Fig. 6.9 [39]). If the periodicity is in the y-direction, the translation vector between adjacent boundaries is ½ [**a** + **c**].

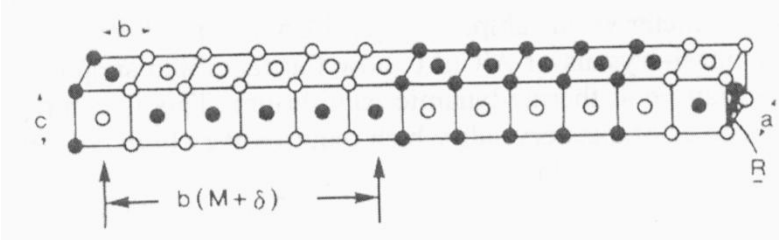

Figure 6.9: CuAu II-type superstructures with a periodicity of two domains, each consisting of five unit cells of CuAu I structures, in the y-direction [39]. The translation vector at the APBs is **R** = ½ [**a** + **c**].

There may be CuAu II-type of ordering of the Si – Sn sub-lattice of $Mg_2Si_{1-x}Sn_x$. Structure factors were not calculated accurately for this possible superstructure, because the number of unit cells in each period may vary. In the diffraction patterns with extra reflections presented earlier, *h*00 reflections where *h* is odd are observed because of double diffraction. They are predicted to appear for CuAu I-type structures. In a CuAu II-type of superlattice, an APB between two adjacent domains is a glide plane. For $k = 0$, the reflection condition is that *h* is even (see two-dimensional space group number 4 in [56]). The lengths of the domains may vary in a crystal, so that the (002) planes are randomized with respect to occupancy of Si and Sn atoms. As a result, h00 reflections where h is even disappear. The diffraction patterns in Fig. 6.10 are consistent with this model. They could be [100] and [112] diffraction patterns of $Mg_2Si_{1-x}Sn_x$ with a Mg-filled CuAu II-type superstructure.

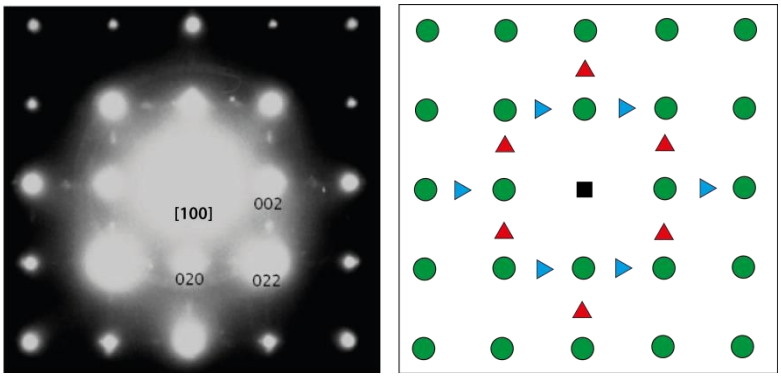

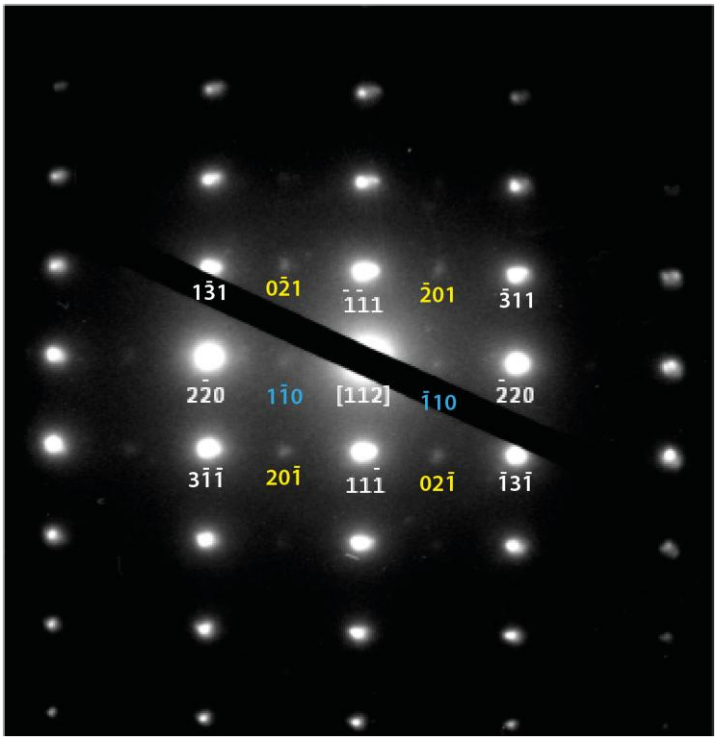

Figure 6.10: Diffraction patterns indexed as a crystal with CuAu II-type ordering of Si and Sn. a) A [100] diffraction pattern with contributions from two domains of ordered structures oriented at 90° relative to each other. b) A model of the [100] diffraction pattern, where red triangles represent reflections caused by one domain and blue triangles represent reflections due to another. c) A [112] diffraction pattern, showing the main reflections (white), superstructure reflections (yellow) and reflections caused by double diffraction (blue).

6.2.7.2 Satellites in diffraction patterns of $Mg_2Si_{1-x}Sn_x$

Fig. 6.11 shows three different diffraction patterns where some of the reflections are split into or surrounded by weak satellites. In the first, which is projected along the [001] zone axis, the reflections for which ½ (h + k) = 2n +1 are surrounded by four satellites (see Fig. 6.11a), in the second, which is projected along [110], all reflections are surrounded by two satellites (see Fig. 6.11b), and in the third, which is also projected along [110], all reflections are surrounded by four satellites.

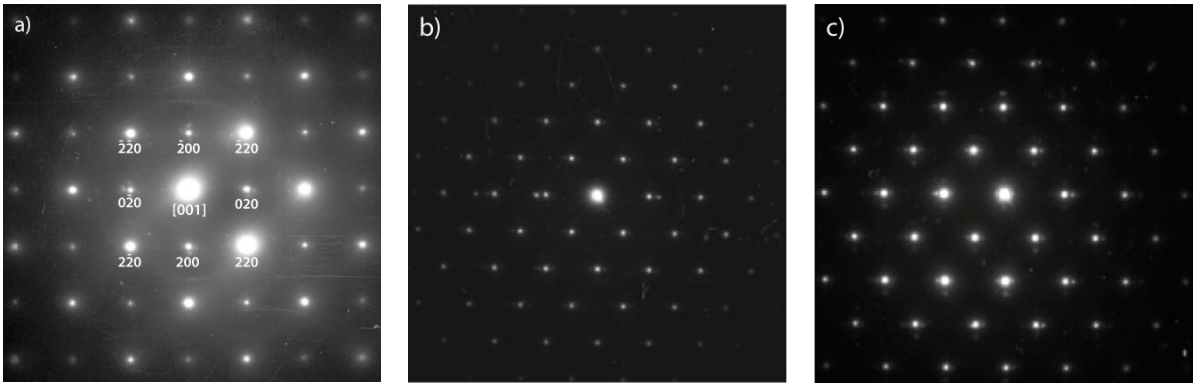

Figure 6.11: a) An [001] diffraction pattern with satellites around the main reflections with indices ½ (h + k) = 2n +1. b) A [110] diffraction pattern where all of the main reflections are surrounded by two satellites. c) A [110] diffraction pattern with four satellites around all of the main reflections.

Anti-phase boundaries:

According to optical simulation experiments carried out by van Dyck et al., anti-phase boundaries (APBs) with a displacement vector along [110] in primitive cubic lattices should cause reflections with $h + k = 2n +1$ to split into two reflections [55]. The splitting increases with decreasing domain size and is in the direction perpendicular to the displacement vector. The same kind of splitting occurs for an *fcc* lattice, but it is the *hkl*-reflections with ½ h + ½ k = 2n + 1 that are split, and the translation vector is [¼ ¼ z]. The component of the displacement vector perpendicular to the diffraction plane cannot be determined from a diffraction pattern, but a hypothesis is that the grains are displaced by [¼ ¼ ¼] relative to each other. In this situation, Mg atoms occupy the positions of $Si_{1-x}Sn_x$ atoms and vice versa at the boundary.

The satellites in the diffraction pattern in Fig. 6.11a may indicate the presence of such APBs. If that is the case, there are at least two sets of mutually orthogonal APBs in the particle. One set causes splitting of the main reflections in the horizontal direction and the other in the vertical direction. APBs parallel to an electron beam in an electron microscope are invisible. All of the main reflections are still present, because a large part of the particle contributing to the SAD pattern does not contain any boundaries.

The satellites around the 111-type reflections in Figs. 6.11b and 6.11c may be caused by multiple scattering from those around the 200-type of reflections.

One would have to do a tilt series along the 200 series to determine if the satellites are due to APBs. This was not done in this project, partly because the weak reflections could not be observed in the TEM and because the main focus on the instrument was to tilt along the 220 series and look for Cu_3Au and CuAu I-type superstructures. However, the four satellites around the reflections have an asymmetrical intensity distribution. The strongest of them must be caused by inclusions of other phases in the particles, and the weaker ones due to double diffraction.

Epitaxially grown tin inclusions:

As mentioned above, the satellites surrounding strong reflections in Fig. 6.11 have an asymmetrical intensity distribution. The satellites further away from the direct beam than the 200-type of reflections are the strongest ones. Another noteworthy observation is that the 400-type of reflections each have a satellite twice as far away from the direct beam as the strong satellites of 200-type of reflections are. Based on lattice parameters obtained by measuring the diffraction patterns, it is very probable that there are phases of (Sn) that have grown epitaxially inside the matrix of $Mg_2Si_{1-x}Sn_x$ particles. The series of 200 reflections of Sn in Figs. 6.11a, 6.11b and 6.11c are on the same row as the 200 series of the $Mg_2Si_{1-x}Sn_x$ particles. Therefore, the (200) plane of Sn is parallel to the (200) plane of the rest of the particle. In Fig. 6.11c, the (220) plane of Sn is parallel to the (220) plane of the $Mg_2Si_{1-x}Sn_x$ particle (see Fig. 6.12). Two sets of satellites correspond to two mutually orthogonal phases in Fig. 6.12a, while Figs. 6.12b and 6.12c indicates the presence of one such phase. The weaker satellites are caused by multiple scattering.

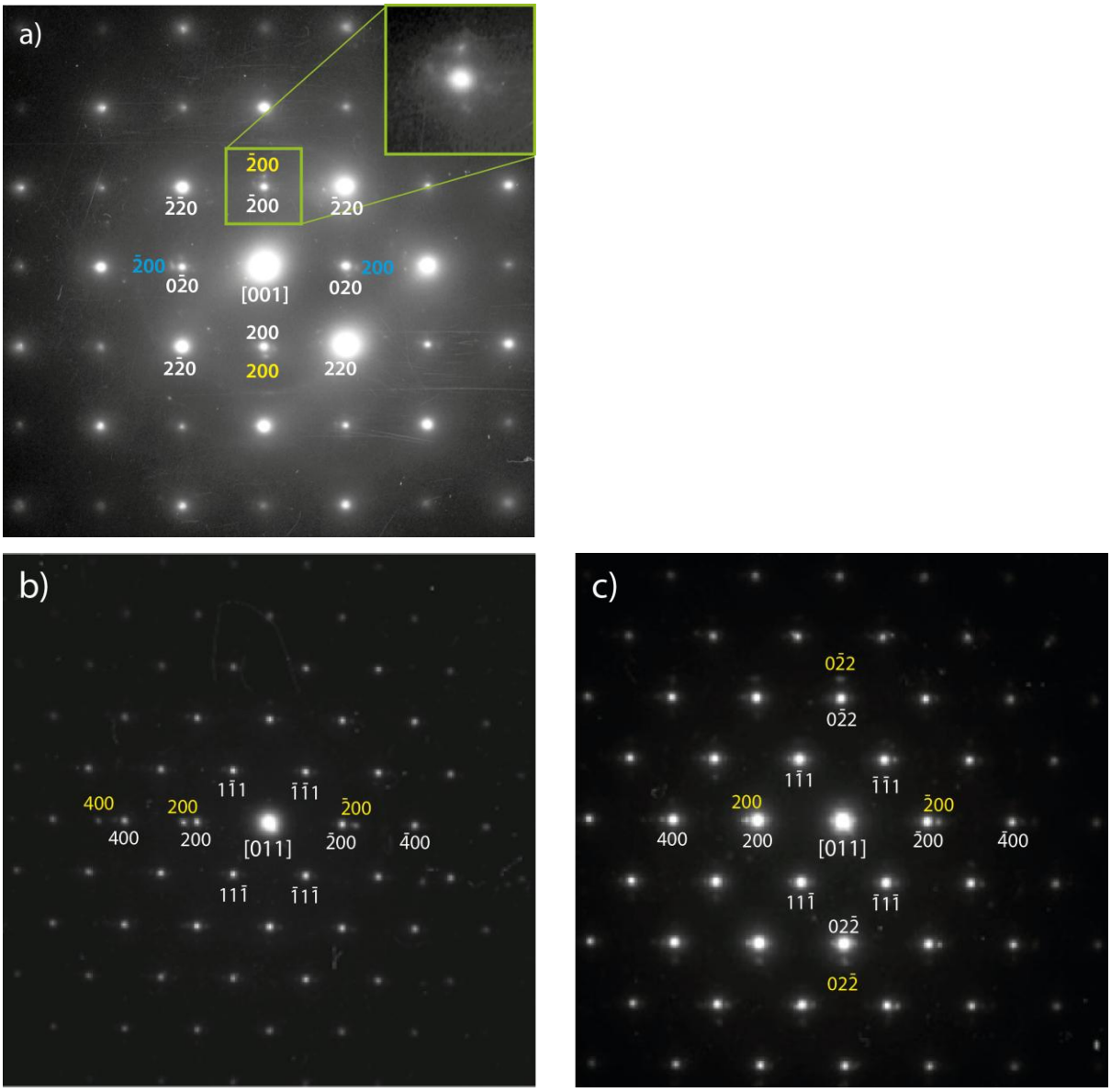

Figure 6.12: Diffraction patterns with weak satellites indicating the presence of Sn inclusions. a) An [001] diffraction pattern of $Mg_2Si_{1-x}Sn_x$ with two sets of satellites (yellow and blue), corresponding to two mutually orthogonal domains of Sn with their (200) planes parallel to the (200) plane of the $Mg_2Si_{1-x}Sn_x$ crystal. b) A [011] diffraction pattern. There is a Sn inclusion with (200) planes parallel to the (200) planes of the rest of the particle. c) An [011] diffraction pattern with Sn inclusions. The Sn inclusion is also projected along the [011] zone axis.

6.2.7.3 Summary of diffraction effects

The superstructure reflections in the [112] and [001] diffraction patterns is a result of local ordering of the Si and Sn atoms, possibly as in CuAu II-type or similar structures, but the proposed superstructures based on ordered Cu_3Au and CuAu I-type were not characterized.

Satellites surrounding reflections in [001] and [110] diffraction patterns are due to double scattering in the presence of (Sn) embedded in the matrix.

7. Conclusion

Samples of $Mg_2Si_{1-x}Sn_x$ with nominal compositions of x = 0.00, 0.25, 0.50, 0.75 and 1.00 (with Mg in excess) were synthesized by different techniques. The synthesis methods include solid state reactions, solidification of melts and a so-called boron oxide flux method.

Equilibrium was not obtained. Optical microscopy and SEM revealed that the products made by melting the reactants consisted of Si-rich $Mg_2(Si,Sn)$ dendritic crystals, surrounded by Sn-rich $Mg_2(Si,Sn)$ crystals, which were in turn surrounded by eutectic mixtures of Sn and Mg_2Si. Si crystals were dispersed throughout the samples.

According to powder XRD experiments performed on all of the samples, $Mg_2Si_{1-x}Sn_x$ has an antifluorite structure, as reported in the literature. However, structural investigations with TEM reveal that there may be ordering of the Si – Sn sub-lattice at certain compositions. Only certain projections within tilt series show signs of local ordering consistent with the two proposed superstructures, namely Cu_3Au for x = 0.25 and 0.75 and CuAu I-type for x = 0.50. Judging by tilt series of diffraction patterns, the ordered structures are not consistent with the proposed superstructures, but the ordering may be due to CuAu II-type or similar ordered structures.

200 and equivalent reflections were surrounded by satellites in certain diffraction patterns. These satellites were interpreted to be caused by double diffraction due to the presence of elemental Sn. The (200) planes of Sn are parallel to the 200 planes in $Mg_2Si_{1-x}Sn_x$.

8. Future work

Anyone who works with $Mg_2Si_{1-x}Sn_x$ should be aware of the difficulty of synthesizing good samples. Much better samples are needed for microstructural studies of this material than those that were made in this project. A closed system is strongly recommended, so that the products can be quenched in water without reacting with other phases, and subsequently post-annealed. A closed system also limits the evaporation of Mg.

With better samples and hence better TEM specimens, it would be much easier to find particles that may have locally ordered domains. Selected area diffraction techniques should be used for looking for possible superstructures, while convergent beam electron diffraction is a better option for determining the symmetry, as the determinations can be performed independently of the camera length of the TEM.

When it comes to determining the width of the immiscibility gap in the system Mg_2Si – Mg_2Sn, samples should be hot-pressed at different pressures to see how the width of the gap varies with the parameters of the hot-pressing. The Structure Physics Group at the University of Oslo is getting hold of hot-pressing equipment ideal for $Mg_2Si_{1-x}Sn_x$ samples in the near future.

9. References

[1] H J Goldsmid, R Hull, R M Osgood, Jr, J Parisi and H Warlimont (2010), *Introduction to thermoelectricity.* Springer-Verlag Berlin Heidelberg.

[2] D M Rowe (ed.) (2006), *Thermoelectrics handbook: Macro to nano.* CRC Taylor and Francis Group, Boca Raton.

[3] V K Zaitsev, M I Fedorov, E A Gurieva, I S Eremin, P P Konstantinov, A Yu Samunin and M V Vedernikov (2006) *Highly effective $Mg_2Si_{1-x}Sn_x$ thermoelectrics.* Physical Review B **74,** 045207.

[4] Q Zhang, J He, T J Zhu, S N Zhang, X B Zhao and T M Tritt (2008), *High figures of merit and natural nanostructures in $Mg_2Si_{0.4}Sn_{0.6}$ based thermoelectric materials.* Applied Physics Letters **93,** 102109.

[5] Sh Muntyanu, E B Sokolov and E S Makarov (1966) *Study of the Mg_2Sn – Mg_2Si system.* Journal of Inorganic Materials **2,** 870-5.

[6] E N Nikitin, É N Tkalenko, V K Zaitsev, A I Zaslavskii and A K Kuznetsov (1968) *A study of the phase diagram for the Mg_2Si – Mg_2Sn system and the properties of certain of its solid solutions.* Journal of Inorganic Materials **4,** 1656-9.

[7] I-H Jung, D-H Kang, W-J Park, N J Kim and SH Ahn (2007) *Thermodynamic modelling of the Mg-Si-Sn system.* Computer Coupling of Phase Diagrams and Thermochemistry **31,** 192-200.

[8] ID no. 206780, ASM Alloy Phase Diagrams Center, P. Villars, editor-in-chief; H. Okamoto and K. Cenzual, section editors; http://www.asminternational.org/AsmEnterprise/APD, ASM International, Materials Park, OH, USA, 2006-2012.

[9] Q Zhang, T J Zhu, A J Zhou, H Yin and X B Zhao (2007) *Preparation and thermoelectric properties of $Mg_2Si_{1-x}Sn_x$.* Physica Scripta **T129,** 123-126.

[10] A Kozlov, J Gröbner and R Schmid-Fetzer (2011) *Phase formation in Mg-Sn-Si and Mg-Sn-Si-Ca alloys.* Journal of Alloys and Compounds **509,** 3326-3337.

[11] S Zhou, C Bai and C Fu (2011) *A fast synthesis and sintering of $Mg_2Si_{1-x}Sn_x$ ($0 \leq x \leq 1.0$) solid solutions by microwave irradiation.* Advanced Materials Research Vols. 197-198, pp 417-420.

[12] M Riffel and J Schilz (1996), *Mechanically alloyed $Mg_2Si_{1-x}Sn_x$ solid solutions as thermoelectric materials.* Proceedings ICT '96 – Fifteenth International Conference on Thermoelectrics, 133-136.

[13] R B Song, T Aizawa and J Q Sun (2006) *Synthesis of $Mg_2Si_{1-x}Sn_x$ solid solutions as thermoelectric materials by bulk mechanical alloying and hot pressing.* Materials Science and Engineering B 136, 111-117.

[14] T Aizawa and K Kondoh (2001) *Nanostructured materials via bulk mechanical alloying.* Scripta Materialia **44,** 1751–1755.

[15] D Boudemagh, D Fruchart, R Haettel, E K Hlil, A Lacoste, L Ortega, N Skryabina, J Tobola and P Wolfers (2011) *Crystal structure analysis of the $Mg_2Si_{1-x}Sn_x$ system having potential thermoelectric properties at high temperature.* Solid State Phenomena Vol. 170, pp 253-258.

[16] Personal communication from Dr. Daniel Fruchart, e-mail: fruchart@grenoble.cnrs.fr

[17] Y Isoda, N Shioda, H Fujiu, Y Imai and Y Shinohara (2004) *Thermoelectric properties of sintered $Mg_2Si_{(1-x)}Sn_x$.* Proc. 23rd International conference on Thermoelectrics, Adelaide, Australia, July (2004) #124.pdf.

[18] Y Isoda, T Nagai, H Fujiu, Y Imai and Y Shinohara (2006) *Thermoelectric properties of Sb-doped $Mg_2Si_{0.5}Sn_{0.5}$.* 2006 International Conference on Thermoelectrics.

[19] H Gao, T Zhu, X Liu, L Chen and X Zhao (2011) *Flux synthesis and thermoelectric properties of eco-friendly Sb doped $Mg_2Si_{0.5}Sn_{0.5}$ solid solutions for energy harvesting.* Journal of Materials Chemistry **21,** 5933-5937.

[20] L Chen, G Jiang, Y Chen, Z Du, X Zhao and T Zhu (2011) *Miscibility gap and thermoelectric properties of ecofriendly $Mg_2Si_{1-x}Sn_x$ $(0.1 \leq x \leq 0.8)$ solid solutions by flux method.* Journal of Materials Research, Vol. 26, No. 24.

[21] W Luo, M Yang, F Chen, Q Shen, H Jiang and L Zhang (2009) *Fabrication and thermoelectric properties of $Mg_2Si_{1-x}Sn_x$ $(0 \leq x \leq 1.0)$ solid solutions by solid state reaction and spark plasma sintering.* Materials Science and Engineering B 157, 96-100.

[22] X Zhang, Q-M L, L Wang, F-P Zhang and J-X Zhang (2010) *Preparation of $Mg_2Si_{1-x}Sn_x$ by induction melting and spark plasma sintering, and thermoelectric properties.* Journal of Electronic Materials **39,** 1413-1417.

[23] S K Hanssen (2012) *Casting thermoelectric $Mg_2Si_{1-x}Sn_x$.* Bachelor's thesis.

[24] H Le-Quoc, A Lacoste, S Béchu, A Bès, D Bourgault and D Fruchart (2012) *Deposition of thin films of $Mg_2Si_{1-x}Sn_x$ solid solution by plasma-assisted co-sputtering.* Journal of Alloys and Compounds **538,** 73-78.

[25] R B Song, T Aizawa, A Yamamoto and T Obara (2005) *Solid-state synthesis of $Mg_2Si_{1-x}Y_x$(Y=Ge and Sn) thermoelectric materials via bulk mechanical alloying.* Journal of Metastable and Nanocrystalline Materials **24-25,** p. 347-350.

[26] T Aizawa, R Song and A Yamamoto (2006) *Solid state synthesis of ternary thermoelectric magnesium alloy, $Mg_2Si_{1-x}Sn_x$.* Materials Transactions **47(4),** p. 1058-1065.

[27] H L Gao, X X Liu, T J Zhu, S H Yang and X B ZHAO (2011) *Effect of Sb doping on the thermoelectric properties of $Mg_2Si_{0.7}Sn_{0.3}$ solid solutions.* Journal of Electronic Materials **40(5),** p. 830-834.

[28] W Luo, M Yang, F Chen, Q Shen, H Jiang and L Zhang (2010) *Preparation and thermoelectric properties of Bi-doped $Mg_2Si_{0.8}Sn_{0.2}$ compound.* Materials Transactions **51(2),** p. 288-291.

[29] ID no. 100218, ASM Alloy Phase Diagrams Center, P. Villars, editor-in-chief; H. Okamoto and K. Cenzual, section editors; http://www.asminternational.org/AsmEnterprise/APD, ASM International, Materials Park, OH, USA, 2006-2012.

[29] 35-0821, PDF-2, JCPDS – International Centre for Diffraction Data, 12 Campus Boulevard, Newtown Square, PA, USA.

[30] A Kozlov, M Ohno, R Arroyave, Z K Liu and R Schmid-Fetzer (2008) *Phase equilibria, thermodynamics and solidification microstructures of Mg-Sn-Ca alloys, Part 1: Experimental investigation and thermodynamic modeling of the ternary Mg-Sn-Ca system.* Intermetallics **16(2),** p. 299-315.

[30] 27-1402, PDF-2, JCPDS – International Centre for Diffraction Data, 12 Campus Boulevard, Newtown Square, PA, USA.

[31] 04-0673, PDF-2, JCPDS – International Centre for Diffraction Data, 12 Campus Boulevard, Newtown Square, PA, USA.

[31] K Valset, E Flage-Larsen, P Stadelmann and J Taftø (2011) *Electronic structure of Mg_2Si by combining electron diffraction and first-principle calculations.* Acta Materialia **6,** 972-976.

[32] 35-0773, PDF-2, JCPDS – International Centre for Diffraction Data, 12 Campus Boulevard, Newtown Square, PA, USA.

[32] C Kittel (2005) *Introduction to solid state physics (8th ed.).* John Wiley & Sons, Inc., Hoboken.

[33] 07-0274, PDF-2, JCPDS – International Centre for Diffraction Data, 12 Campus Boulevard, Newtown Square, PA, USA.

[33] D B Williams and C B Carter (2009) *Transmission electron microscopy: a textbook for materials science (2nd ed.).* Springer, New York.

[34] P A Doyle and P S Turner (1968) *Relativistic Hartree-Fock X-ray and electron scattering factors.* Acta Cryst. **A24,** p. 390-396.

[35] U Schubert and N Hüsing (2005) *Synthesis of inorganic materials (2nd ed.).* WILEY-VCH Verlag GmbH & Co. KgaA, Weinheim.

[36] A R West (1985) *Solid state chemistry and its applications.* John Wiley & Sons, Ltd., Chichester.

[38] D Brandon and W D Kaplan (2008) *Microstructural characterization of materials (2nd ed.).* John Wiley & Sons, Ltd., Chichester.

[39] A Olsen (2008) *The theory and practice of transmission electron microscopy in materials science*. Department of Physics, University of Oslo, Oslo.

[40] R Erni (2010) *Aberration-corrected imaging in transmission electron microscopy: an introduction.* Imperial College Press, London.

[41] Kemetyl Norge AS, Delitoppen 3, N-1540 Vestby.

[42] VWR International, 100 Matsonford Road, Radnor, Pennsylvania.

[43] Fluka Chemie AG, Industriestrasse 25, 9471 Buchs.

[44] AGAR Scientific, Elektron Technology UK Ltd, Stansted, Essex.

[45] Demotec, Brentanostrasse 22, Nidderau.

[46] Struers, 24766 Detroit Road, Cleveland, Ohio.

[47] Gatan, 5794 West Las Positas Boulevard, Pleasanton, California.

[48] Goodfellow, 125 Hookstown Grade Road, Coraopolis, Pennsylvania.

[50] Eva Version 13.0.0.3, Diffrac Plus Evaluation.

[51] UnitCell Version 0.95, BeN Systems 1997, 1999; Special version for H. W. Brinks, University of Oslo.

[49] JENOPTIK ProgRes C5.

[52] Gatan DigitalMicrograph

[53] P M Kelly, C J Wauchope and X Zhang (1994) *Calculation of overall tilt angle for a double tilt holder in TEM.* Microscopy research and technique **28,** p. 448-451.

[55] D van Dyck, G van Tendeloo and S Amelinckx (1984) *Diffraction effects due to a single translation interface in a small crystal.* Ultramicroscopy **15,** p. 357-370.

[54] F T Greene and J L Margrave (1965) *The vapor pressure of boron oxide over the range 1946-2419 K.* The Journal of Physical Chemistry, p. 2112-2115.

[55] G S Nolas, D Wang and M Beekman (2007) *Transport properties of polycrystalline $Mg_2Si_{1-y}Sb_y$ $(0 \leq y < 0.4)$.* Physical Review B **76,** 235204-1 – 6.

[56] International Tables of Crystallography, Vol. A, Space-group symmetry (2006)

[58] Personal communication with Prof. Vidar Hansen, e-mail: vidar.hansen@uis.no

10. Appendix

Fig. A.1 shows a high resolution transmission electron microscope (HRTEM) image and a selected area diffraction (SAD) pattern of a nitride phase. EDS analyses indicate a composition of Mg_4Si_4N, but the nitrogen content has not been quantified correctly. Space group determination is not possible, because this is the only diffraction pattern obtained from this area. It shows threefold symmetry, so it could be a [111] diffraction pattern of a cubic lattice or an [001] diffraction pattern of a trigonal or a hexagonal lattice.

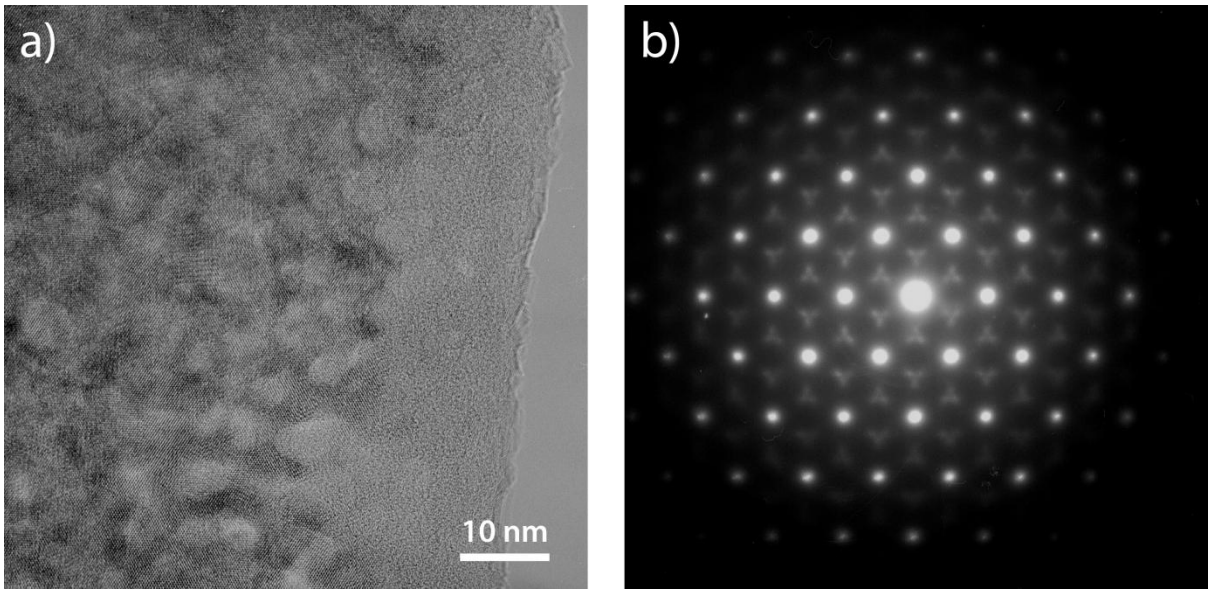

Figure A.1: A HRTEM image of the nitrogen-containing area (left) and a SAD pattern from a relatively large part of the area (right).

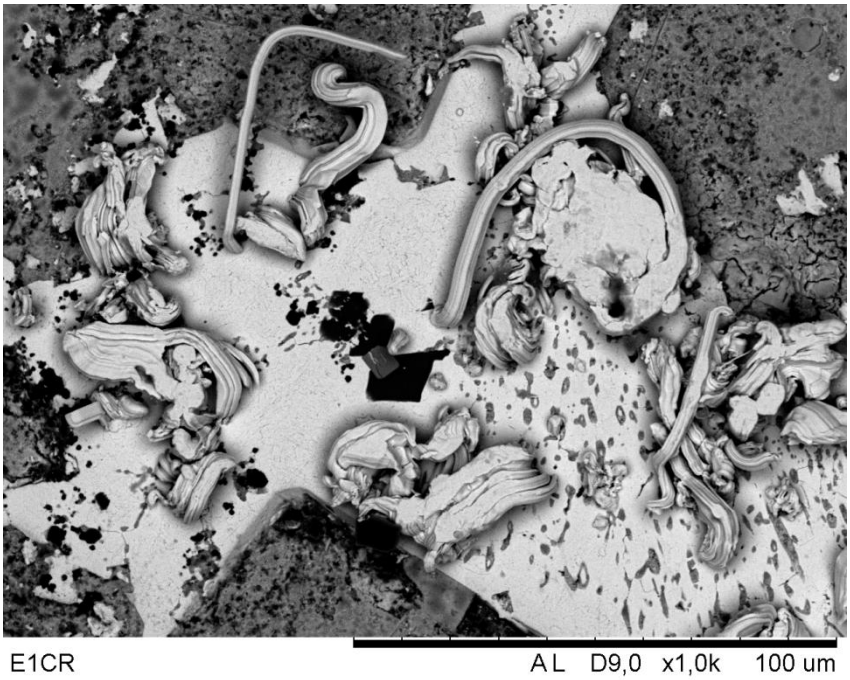

Figure A.2: Sn fibres sticking out from an area of the surface of sample $Mg_2Si_{0.25}Sn_{0.75}$-1150, which had been unprotected for five months.